Quantitative imaging of lung function using hyperpolarised gas MRI

Thesis submitted for the degree of Doctor of Philosophy

Felix Clemens Horn

Academic Unit of Radiology
Department of Cardiovascular Science
School of Medicine
The University of Sheffield

Supervisors: Jim Wild, Juan Parra-Robles
Examiners: Jan Wolber, Peter Thelwall

e-thesis submission (edited version)
January 2015

Acknowledgements

First and foremost I owe greatest gratitude to my supervisor Jim Wild, who has supported me and given me patient guidance throughout this thesis whilst allowing me the room to work my own way and develop. I thank him for all the effort he put into training me and for sending me to numerous conferences. With Jim's scientific thinking, his dedication to the topic and his social attitude towards us as a group he's a person I look up to.

Equally I'd like to express my gratitude towards my second supervisor Juan Parra-Robles. It's been an amazing pleasure to learn from Juan. I thank him for his thoughtful advice and his eagerness to explain and discuss with me.

I'm thankful to have done this work together with great colleagues/friends from my group in Sheffield. I'm thankful to Helen, who's been incredibly helpful, without whom I could not have accomplished all this. Graham, who's supported me during the first months after arriving in Sheffield. Equally I'd like to thank Guilhem, General, Neil and Madhwesha, who have had contribution towards accomplishing this work. Finally I'd also like to acknowledge Martin Deppe for introducing me into my project during his last weeks in Sheffield and who's laid the foundations of the work that I've been doing here in Sheffield. Last but not least thanks to Peggy Xu, the best person to share a desk with (when you like chocolate).

I am grateful to Alex Horsley and Laurie Smith who have taught me on pulmonary function testing, taught me acquiring pulmonary function data on my own and both have contributed to this work.

I would like to thank Leanne Armstrong, Yvonne Steel and the whole Academic Unit of Radiology for all their help and amazing company in the coffee room. I'd like to thank in particular the radiographers of our unit for their great help with scanning patients.

I would also like to express my appreciation to the organiser of the pulmonary imaging network (PI-net) Jesus Ruiz-Cabello and all contributors. It's been an honour to be part of this European training network and meeting people from all over Europe for focused scientific exchanges and friendship.

I'd like to express my gratitude towards my former supervisor from Technischer Hochschule Nürnberg, Prof. Florian Steinmeyer, an admirable scientist, who's introduced me to MRI and awakened the fascination thereof. Equally I'd like to thank my former supervisors from Siemens Healthcare, Dr. Dieter Ritter and Matthias Gebhardt.

But all this would have been impossible without the support from family and friends. A special thanks to my oldest and best friend here, Jenny for the countless evenings discussing all matters of life. Thanks to Helen, Kevin, General and Carolyn for the great time together climbing inside,

outside as well as the after climbing social sessions. Thanks to my friends Nico and Simon for amazing times together at the Matrix. And thanks to my flatmate Dani, the one who had to bear me most of all. Thanks also to my German friends, who came here so many times to explore Britain together with me, to Christoph and Stephan. Cheers also to my old colleague Martin for all the advice he's given me over the years.

Finally thanks to my dear family. Thanks to my parents Beatrice and Ulrich, without whom I would not be where I'm today. I'd also like to thank my beloved sisters Ina, Susanne, Elisabeth, Maria, and Cornelia for all their support, love and their countless visits.

And last but not least a great thanks to my girlfriend Fabiola, for her continuous support, encouragement and for coping with me during writing up. Thanks for the countless times you were coming to Sheffield when I was not able to come visit you.

This thesis was funded by European framework 7 – PI-net.

Abstract

This thesis describes methods for Magnetic Resonance Imaging (MRI) of hyperpolarised noble ^{3}He and ^{129}Xe gas to quantitatively measure lung ventilation and changes thereof in humans. Three different methods are proposed and tested:

1. Percentage ventilated lung volume derived from functional (hyperpolarised gas imaging) and anatomical (proton imaging) imaging acquired in a single breath-hold is compared to images from two separate breath-holds. The single breath technique is shown to be significantly more reliable and can help to reduce statistical noise.
2. Treatment response mapping is developed as a quantitative measure of lung ventilation response to intervention. The measured signal difference between ventilation images acquired before and after treatment (provocation) is used to calculate changes in gas regional distribution. The technique is validated in an asthma cohort and preliminary findings indicate the method is thought to be more sensitive to changes than existing hyperpolarised gas techniques as existing pulmonary function tests.
3. With multiple breath washout imaging a method is developed and investigated to derive quantitative functional information from images by monitoring regional signal decay during tracer gas washout. The technique is extended to produce regional quantitative information of ventilation in 3D. Reproducibility of the technique is tested and its errors are systematically investigated. Furthermore, image acquisition is optimised using bSSFP imaging. The method is applied to a CF and an asthma cohort.

   Finally, preliminary results are presented comparing multiple breath washout measured at the mouth in the pulmonary function lab to a predicted global washout as modelled from regional functional information derived from the imaging technique.

Contents

List of abbreviations

%TR	Percentage treatment response
%VV	Percentage ventilated volume
bSSFP	Steady state free precession imaging sequence
BW	Bandwidth
DSC	Dice similarity coefficients
FEV1	Forced expiratory volume in 1 second
FRC	Function residual capacity
FVC	Forced ventilator capacity
LCI	Lung clearance index
LV	Inspiratory lung volume
MBW	Multiple breath washout
MRI	Magnetic resonance imaging
RF	Radio-frequency
r	Fractional ventilation
SD	Standard deviation of fractional ventilation
SPGR	Spoiled gradient echo imaging sequence
TE	Echo time
TLV	Total lung volume of the lung cavity
TR	Repetition time
TV	Tidal volume
VH	Ventilation heterogeneity

Chapter 1 Introduction

1.1. Motivation

2014 year it has been 20 years since the first images from hyperpolarised ^{129}Xe were acquired in animals [1]. Only one year later hyperpolarised ^{3}He was successfully used to acquire images in human lungs [2]. In the past decades major efforts were undertaken to improve sensitivity of this imaging technique with advances in hardware [3], sequence design [4-6] as well higher polarisation levels of hyperpolarised gases e.g. using stronger lasers [7].
In an editorial in early 2014, Prisk and Sá emphasise the achievements of imaging hyperpolarised gases and point out the need for quantitative numbers for better physiological interpretation of data [8]. Those quantitative metrics and imaging markers are crucial for successful classification of disease and early detection of change in regional lung function. The motivation of this thesis is the development of more quantitative metrics for measuring lung ventilation with hyperpolarised gases in human lungs.

1.2. Thesis outline

Chapter 2 serves as a very brief introduction to the background of MRI physics and pulmonary physiology and function testing. This has deliberately been kept short.

Chapter 3 investigates the increase in reliability of percentage ventilated volume (%VV) gained through the use of a single breath-hold imaging method: Instead of acquiring functional (^{3}He) and anatomical (^{1}H) images in separate breath-holds, both images are acquired in a single breath-hold. This is shown to significantly decrease the variability of the %VV in repeated experiments when compared to a technique acquiring both images in separate breath-holds.

Chapter 4 introduces treatment response mapping as a method to derive quantitative information of ventilation changes from images acquired before and after intervention. Differences of regional changes of static ventilation weighted image signal intensity are used derive percent treatment response (%TR). The technique is tested on an asthma cohort and compared to %VV and spirometry.

Chapter 5 explains the methodology of multiple breath washout imaging. Images are acquired in subjects after each breathing cycle (expiration-inspiration) over multiple breaths. Regional gas washout is used to derive quantitative maps of fractional ventilation in 2D and 3D. The washout imaging protocol and post-processing steps to derive fractional ventilation from images are

described. The method is compared to independently measured lung volume turn over and repeatability is tested in 7 volunteers.

Chapter 6 is an error analysis of multiple breath washout imaging. Sources of error are addressed and resulting errors are estimated using values from the literature and obtained in measurements.

Chapter 7 demonstrates further advances in multiple breath washout imaging. Balanced steady state imaging (bSSFP) is demonstrated to use only half the dose of hyperpolarised ^{3}He when compared to the initial protocol (from Chapter 5) using an SPGR sequence. Quantitative fractional ventilation maps derived from images acquired with a bSSFP sequence are compared to the SPGR sequence as used in Chapter 5. Quantitative maps from both sequences show very good agreement. Using the bSSFP sequence the feasibility of MBW-imaging in 3D with hyperpolarised ^{129}Xe is also demonstrated.

Chapter 8 tests multiple breath washout imaging in two clinical studies: (1) comparing healthy children to age matched cystic fibrosis (CF) patients with early lung disease and (2) an cohort of moderate-severe asthmatics. An increased sensitivity of multiple breath washout derived ventilation heterogeneity parameter SD is demonstrated compared to methods from the pulmonary function lab such as LCI and spirometry in healthy children when compared to CF patients. Good correlation between SD and spirometry as well as SD and LCI could be found over the whole cohort of 47 subjects and controls.

Chapter 9 briefly introduces the theory to predictively model multiple breath washout as measured globally at the mouth using the regional functional information from imaging. A direct comparison in a preliminary study on 3 subjects shows the difficulties of the proposed method and highlights the scope for future work.

Chapter 2 Background

2.1. Principles of nuclear magnetic resonance

Nuclear magnetic resonance (NMR) was first discovered by Bloch and Purcell, which they were given a joint Nobel Price for in 1952 [9, 10]. Their seminal work quantifies the effect of a spin precessing in the presence of a magnetic field setting the stage for all further developments. To regionally differentiate soft tissues Lauterbur and Mansfield utilised imaging gradients in 1973 [11, 12]. This chapter provides a very brief overview of the basic concepts of NMR relevant to this thesis.

2.1.1. Spin angular momentum and magnetisation

NMR is fundamentally based on the interaction of nuclear spin with external magnetic fields. Spin (like mass) is an intrinsic property of elementary particles and atomic nuclei. The nuclear spin ($\vec{I}$) possesses an magnetic moment ($\vec{\mu}$) that is directly related to its spin angular moment ($\vec{S}$) [13]:

$$\vec{\mu} = \gamma \vec{S} = \gamma \hbar \vec{I} \qquad \text{Eq. [2.1]}$$

Where $\hbar$ is the reduced Planck constant $h/2\pi$, $\vec{I}\hbar$ is the spin angular momentum and γ is the gyromagnetic ratio. Nuclear spin $\left|\vec{I}\right|$ takes integer or half-integer values and is non-zero for many atomic nuclei -a requirement of NMR. The gyromagnetic ratio is the ratio of the nuclear magnetic dipole moment to the nuclear angular momentum and is determined by a nucleus's distribution of charge and mass.

Nucleus	γ gyromagnetic ratio (Mhz/T)	Spin(I)	Magnetic moment	Natural abundance (%)
^{1}H	42.58	½	+2.793	99.98
^{3}He	32.43	½	-2.127	$1.37 \cdot 10^{-4}$
^{129}Xe	11.78	½	-0.773	26.4

Table 2.1: Summary of the magnetic properties and isotopic abundance in nature of the principal nuclei relevant to this work [14-16].

For a system of nuclei, the sum of microscopic magnetic moments $\vec{\mu}$ can be visualised as a macroscopic magnetisation in the volume occupied by the system:

$$\vec{M} = \frac{1}{V}\sum_{V}\vec{\mu}_i \qquad \text{Eq. [2.2]}$$

The spin quantum number *I* (and hence the total spin angular momentum) is a fixed quantity for a nucleus in the ground state (see Table 2.1 for values of nuclei relevant to this work). I_z is the quantum number along an arbitrary axis of quantisation (*z*) and can take (*2I+1*) different values ranging from *–I* to *+I*. In the absence of a magnetic field the states (*–I* and *+I*) are energetically equivalent (degenerate).

In the presence of an external magnetic field ($\vec{B}_0$) the ground energy state is split. ^{1}H for example has a spin *I*=+1/2 and occupies 2 different states (corresponding to the nuclear magnetic moment aligning parallel and anti-parallel to $\vec{B}_0$). The energy of interaction of the individual magnetic moments with the external magnetic field is related to the strength of $\vec{B}_0$:

$$E = -\vec{\mu}\ \vec{B}_0 \qquad \text{Eq. [2.3]}$$

The effect is called Zeeman-splitting. The two states are populated according to the Boltzmann distribution at thermal equilibrium, as discussed in Section 2.1.2. The energy difference between the two states is (for a spin ½ nucleus):

$$\Delta E = \gamma\ \hbar\ \left|B_0\right| = \hbar\ \omega_0 \qquad \text{Eq. [2.4]}$$

where $\gamma\ |B_0|$ is the Larmor angular frequency ω_0.

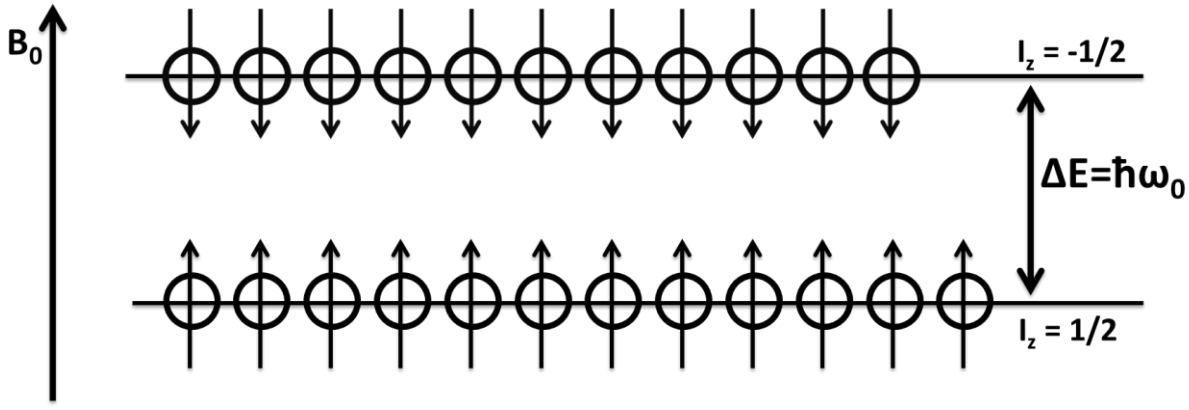

Figure 2.1: The Zeeman effect in the presence of field B_0 for the case of a spin=1/2 nucleus.

2.1.2. Thermal polarisation

Polarisation *P* is defined as the ratio of the difference on number of nuclei on the lower (parallel to $\vec{B}_0$) and higher (anti-parallel) energy states of a spin-½ system in the presence of magnetic field:

$$P = \frac{\left|N_{\uparrow} - N_{\downarrow}\right|}{N_{\uparrow} + N_{\downarrow}} \qquad \text{Eq. [2.5]}$$

Where *P* is a value between 0 and 1 and is usually expressed in percent. $N_{\uparrow}, N_{\downarrow}$ are the quantity of spins in the lower and higher energy states calculated by the Boltzmann distribution. At body temperature the thermal energy of the nuclei is much larger than the energy difference between parallel and anti-parallel states (Eq. [2.4]). Hence, polarisation of a spin system at thermal equilibrium is very small and can be approximated as:

$$P \cong \frac{\hbar\omega_0}{2k_B T} \qquad \text{Eq. [2.6]}$$

where k_B is Boltzmann's constant and *T* is the absolute temperature in Kelvin. The resulting magnetisation $\vec{M}_0$ along a magnetic field $\vec{B}_0$ is typically denoted as M_z (assuming $\vec{B}_0 \equiv B_0\ \hat{z}$) and is proportional to polarisation *P* and spin density ρ:

$$M_z = \rho\ P\ \mu_z \qquad \text{Eq. [2.7]}$$

From Eq. [2.6], the polarisation at body temperature, with B_0= 1.5T is approximately 10^{-5}. In most tissues the low polarisation is compensated for by a high density of protons (spin density in tissue ~$6.7\text{x}10^{22}/\text{cm}^3$ [16]) resulting in sufficient magnetisation for MR-imaging. However, the considerably lower spin density in the lung, in combination with additional compounding effects (e.g. field inhomogeneity due to numerous tissue-air interfaces) make proton imaging in the lung inherently challenging. Noble gases with a ½-spin (^{3}He and ^{129}Xe) can also be used for MR imaging of the lung upon inhalation, but at thermal equilibrium the lower spin density of the gases (~ $0.002\text{x}10^{22}/\text{cm}^3$ at 1-bar and room temperature) and lower gyromagnetic ratios (Table 2.1) result in a considerably smaller magnetisation. Nevertheless, through hyperpolarisation, the polarisation levels of these noble gases can be significantly enhanced compensating for the low spin density and enabling lung MRI with hyperpolarised ^{3}He and ^{129}Xe. Details of the hyperpolarisation methods will be discussed in Section 2.4.

2.1.3. Excitation

Nuclear spin is an intrinsic property of a nucleus which can be described by the laws of quantum physics. In addition, the microscopic magnetic moment $\vec{\mu}$ can be treated according to classical electrodynamics and this formalism is often beneficial to visualise spin dynamics. As discussed above, in the presence of a static magnetic field $\vec{B}_0$ a magnetisation $\vec{M}_0$ is created as the result of the sum of all microscopic magnetic moments. Generally, we consider the B_0-field to act along *z* and hence on thermal equilibrium we can think of the magnetisation vector $\vec{M}_0$ aligning with the, z-axis ($\vec{M}_0 \equiv M_0\ \hat{z}$). When applying a radiofrequency pulse (RF) of frequency f_0, a rotating small magnetic field $\vec{B}_1$ is generated perpendicular to the static field $\vec{B}_0$ and the magnetisation vector tilts into the transverse (*x*,*y*) plane as a result of the applied torque $\vec{M} \times \vec{B}_1$. Depending on the amplitude of the field (B_1, e.g. along the *x*-axis) and duration (*T*) of the RF pulse, the magnetisation vector will be rotated away from its alignment with $\vec{B}_0$ at a 'flip angle' α:

$$\alpha = \int_0^T \gamma \cdot B_1(t) \cdot dt \qquad \text{Eq. [2.8]}$$

This will result in a certain magnetisation component perpendicular to the *z*-axis commonly referred to as transverse magnetisation M_{xy} ($M_{xy}=M_0 \sin\alpha$). It is this transverse magnetisation that is detected as the signal on an NMR experiment as discussed below. Figure 2.2 shows a diagrammatical representation of the excitation process, showing in (A) the initial state of the spin-system at equilibrium and in (B) the same spin-system after application of a RF pulse with a Larmor frequency f_0, resulting in a flip angle α.

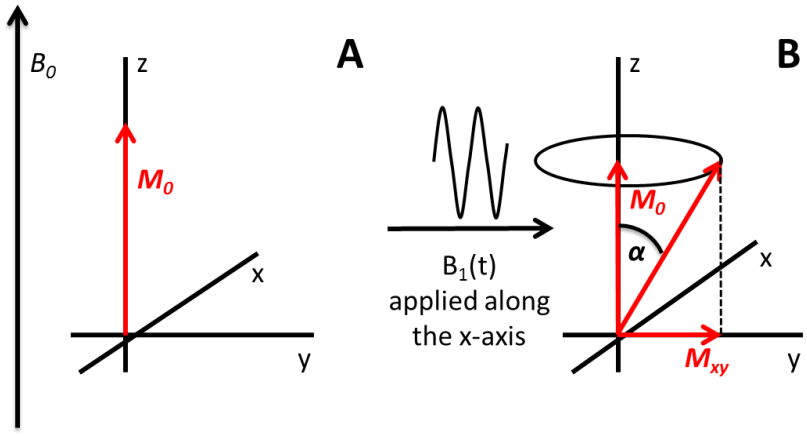

Figure 2.2: (A) Magnetisation M_o in the presence of a static magnetic field B_0. (B) After applying a RF pulse $B_1(t)$ (with frequency ω_0 along the x-axis for a duration T) magnetisation has tilted at flip angle α and has two components: M_{xy} and M_z

2.1.4. Relaxation and signal detection

Immediately after the RF pulse is switched off (Figure 2.2B) the tilted magnetisation vector transverse component (M_{xy}) precesses around $\vec{B}_0$ and recovers its alignment along *z* over time returning to their equilibrium state (*t*=0, Figure 2.2A). During this process the spin system re-emits the energy that was absorbed from the RF pulse. During precession a time-varying magnetic flux is produced in the *xy*-plane inducing an electromotive force (*emf*) in a receiver coil tuned to the Larmor frequency f_0 (the frequency of precession):

$$emf = -\oint \frac{d}{dt}(\vec{M}(\vec{r},t)\cdot\vec{B}_{RF}(\vec{r}))d^3r \qquad \text{Eq. [2.9]}$$

where $\vec{B}_{RF}$ is the magnetic field per unit current produced at location $\vec{r}$ .The voltage measured by the coil as a result of the time-varying flux is called the free induction decay (FID). This decay can be described by two intrinsic processes which lead to relaxation of the magnetisation vector, as related by the Bloch equation [9]:

$$\frac{d\vec{M}}{dt} = \gamma\cdot\vec{M}\times\vec{B}_{ext} + \frac{1}{T_1}(\vec{M}_0 - \vec{M}_z) - \frac{1}{T_2}\vec{M}_{xy} \qquad \text{Eq. [2.10]}$$

Where $\vec{B}_{ext}$ is the $\vec{B}_0$ field pointing in *z*-direction, M_0 is the equilibrium magnetisation, $\vec{M}_z$ and $\vec{M}_{xy}$ denote the component of the magnetisation in the longitudinal direction and transversal planes respectively. T_1 and T_2 are relaxation time constants discussed below. The Bloch equation (Eq. [2.10]) fundamentally describes how the magnetisation in the longitudinal ($\vec{M}_z$) and transverse ($\vec{M}_{xy}$) plane evolves with time. The longitudinal and transversal components can be separated and solved in the following manner:

$$\frac{dM_z}{dt} = \frac{1}{T_1}(\vec{M}_0 - \vec{M}_z) \qquad \text{Eq. [2.11]}$$

Eq. 2.11 describes the interaction of the spin system with its surrounding lattice and can be solved as follows

$$\vec{M}_z(t) = \vec{M}_0\left(1 - e^{-t/T_1}\right) + \vec{M}_z(0)\cdot e^{-t/T_1} \qquad \text{Eq. [2.12]}$$

where $|M_z| = |M_0|$ for $t >> T_1$. This equation shows that there is an exponential regrowth of longitudinal magnetisation $\vec{M}_z$, after excitation. T_1 is the so-called 'spin-lattice' relaxation time. The magnetisation $\vec{M}_{xy}$ in the transverse plane rotates with the Larmor frequency around the *z*-axis (due to $\vec{B}_{ext}$) and relaxes towards zero with a time constant T_2. As a result of the rotation, it is

best to solve the Bloch equation describing magnetisation in the transverse plane in the 'rotating frame' rather than the 'laboratory frame'. In the rotating frame, the term describing the magnetisation precession around the *z*-axis goes to zero. The solution can be expressed as:

$$\vec{M}_{xy}(t) = \vec{M}_{xy}(0) \cdot e^{-t/T_2} \qquad \text{Eq. [2.13]}$$

where T_2 is the 'spin-spin' relaxation resulting in a decreasing $|M_{xy}|$ over time, while T_1 decay is also acting to recover M_z. As the name suggest, spin-spin relaxation concerns spins interacting with each other, rather than the lattice. Spins exchanging energy induce a dephasing of the spin-system coherence in the transverse direction and therefore a decay of the net-magnetisation $|M_{xy}|$.

In addition, in most real applications regional field inhomogeneities also lead to dephasing and effectively a shortening of the time constant of transverse magnetisation decay ($T_2^* < T_2$):

$$\frac{1}{T_2^*} = \frac{1}{T_2} + \frac{1}{T_2'} \qquad \text{Eq. [2.14]}$$

Where T_2' derives from inhomogeneity in the external field $\vec{B}_0$ and within the sample itself (especially in the lungs where many air-tissue interfaces are present[1]). Nevertheless, dephasing induced by field inhomogeneity can be reversed using a 180° RF pulse which results in a re-phasing of the spins and recovery of magnetisation. Sequences using this mechanism are referred to as spin-echo sequences.

2.2. Imaging using magnetic resonance

In the previous section the excitation and relaxation of a spin system was discussed in the context of the Bloch equations. In this section the principles of spatial encoding of the spin system to measure regional information is introduced.

2.2.1. Encoding k-space with magnetic field gradients

To encode the 3D spatial position of the spins, gradients G in all directions (*x*,*y*,*z*) are used. Gradients are magnetic fields that vary linearly with position *x*, *y* or *z*. Superposition of a gradient with the principal magnetic field $|B_0|$ results in a modulation of the Larmor resonant frequency as a function of position, according to:

[1] Two adjacent areas with different magnetic susceptibility (e.g. water-air) cause small magnetic field gradients. In the presence of susceptibility gradients spins dephase faster leading to signal attenuation via T_2^*.

$$\omega(r) = \gamma\ B(\vec{r}) = \gamma\ (B_0 + G(t)\ \vec{r}) \qquad \text{Eq. [2.15]}$$

Where $\vec{r}$ is the position ($|\vec{r}|=(x^2+y^2+z^2)^{½}$) and G($t$) is a gradient field resulting in a regionally varying magnetic field *B(r)*. Note that on 3D G(t) is the resultant gradient of 3 linearly varying gradients on *x*,*y* and *z*. Expressed in the rotating frame, the angular frequency reduces to:

$$\omega(\vec{r},t) = \gamma\ G(t)\ \vec{r} \qquad \text{Eq. [2.16]}$$

In the temporal domain, a gradient switched on for a time interval *T* causes a position-dependent accumulation of phase by the spins:

$$\phi(\vec{r},T) = \int_0^T \omega(\vec{r},t)dt = \gamma \cdot r \cdot \int_0^T G(t)\ dt = 2\pi\ \vec{k}\ \vec{r} \qquad \text{Eq. [2.17]}$$

where $\vec{k} = \frac{\gamma}{2\pi} \cdot \int_0^T G(t) \cdot dt$ is the spatial frequency. With this, the time-dependent MRI signal can be expressed as:

$$s(t) = \int_{object} \rho(r) \cdot e^{-i \cdot \phi(\vec{r},t)} dr \qquad \text{Eq. [2.18]}$$

Eq. [2.18] describes the relationship of the position-dependent spin density $\rho(r)$ to the signal s(t) in the temporal domain. This can be re-written in terms of the spatial frequency *k*:

$$s(k) = \int_{object} \rho(r) \cdot e^{-i \cdot 2\pi \cdot \vec{k} \cdot \vec{r}} dr \qquad \text{Eq. [2.19]}$$

This equation is central to MRI and relates the signal *s*(*k*) to the function of spatial frequency (*k*). Eq. [2.19] is expressed in the rotating frame after demodulation of the Larmor frequency. The spin density $\rho(r)$ is deducted from the detected signal by applying the inverse Fourier transform to *s*(*k*):

$$\rho(r) = FT^{-1}[s(k)] = \int_{k-space} s(k) \cdot e^{i \cdot \vec{k} \cdot \vec{r}} dk \qquad \text{Eq. [2.20]}$$

It is useful to introduce the concept of *k-space* here as the domain of spatial frequencies (Eq. [2.17]). *k* varies as a function of time according to the temporal course of the magnetic field gradient (Eq. [2.17]). Gradients are therefore used to sample *k-space* in 3 spatial dimensions and *k-space* is the Fourier inverse (Fourier space) of the image domain. An example k-space and the corresponding image are shown in Figure 2.3.

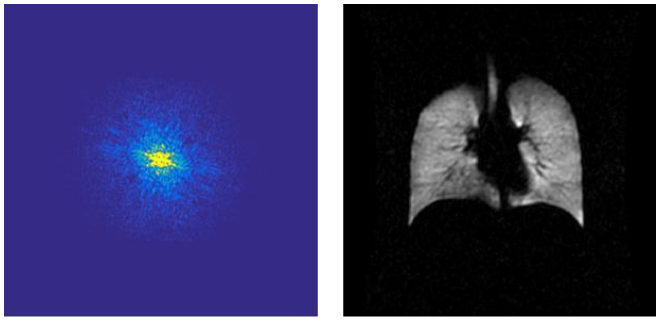

Figure 2.3: Acquisition using hyperpolarised gas MRI, showing a single 2D slice from a healthy subject. Left: k-space; right: image space. Images acquired by the hyperpolarised gas imaging group in Sheffield.

The three axes in an image are commonly labelled as shown in Figure 2.4 (an example lung image acquired using hyperpolarised ^{3}He MRI). For better visualisation, the lung of this healthy smoker has been coloured turquoise and the major airways red. Here the *z*-axis corresponds to the anterior-posterior direction.

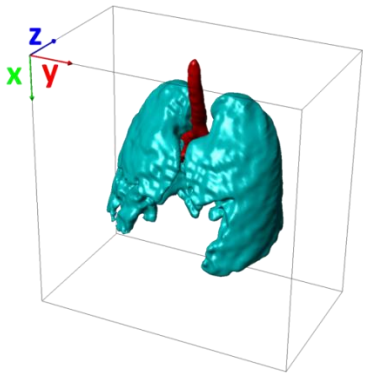

Figure 2.4: Example of a 3D MR lung image acquired using hyperpolarised ^{3}He (lungs in turquoise and major airways in red).

Frequency encoding (x encoding)

A linear gradient applied to the spin-system acts to assign different spatial frequencies to spins as a function of position along the direction in which the gradient is applied. This type of gradient is commonly referred to as a readout gradient (G_r) because it is applied during the sampling (also known as readout) of data. Figure 2.5 shows the action of the readout gradient for the case of a gradient echo sequence.

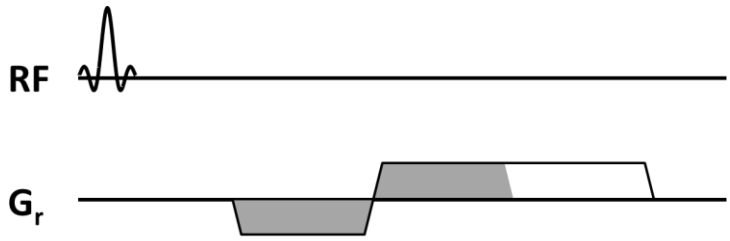

Figure 2.5: After excitation a negative gradient is applied to dephase the spins. Immediately afterwards in the opposite direction is applied rephasing the spins as an echo. The area of the two regions shaded grey is equal.

Phase encoding (y encoding)

A gradient is applied such that spins accrue a phase which differs depending on their position. The gradient is applied immediately after the RF pulse. In 2D MRI, phase encoding is applied in one dimension (usually *y*). However, in 3D sequences two sets of phase encoding gradients are applied to encode spin position in the *y* and *z* dimensions. The effect of a phase encode gradient on an ensemble of spins is schematically shown in Figure 2.6.

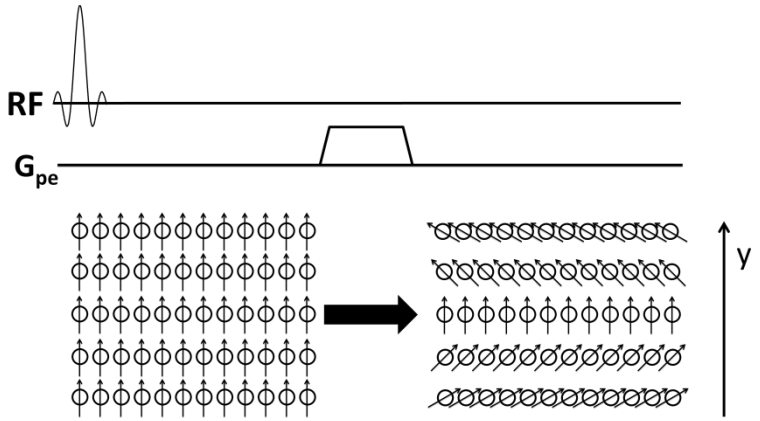

Figure 2.6: Following the RF pulse all spins are aligned (neglecting B_0 inhomogeneity). Spins start to dephase according to their y position after application of the phase encoding gradient (G_{pe}) in the *y*-direction.

Slice selection (z encoding) for 2D MRI

In 2D MRI, *x* and *y* read and phase encoding is typically used to acquire a 2D image from particular segments (slices) of an object. To selectively excite only the spins within a certain slice, a slice-selection gradient (G_{ss}) is switched on in parallel with the application of a tailored RF pulse at centre frequency ω_0 with a bandwidth $\Delta\omega$ determined by its duration τ (see Figure 2.7). The slice select gradient causes a spatial change in resonant frequency meaning that the RF pulse selectively excites only a certain slice of space. Only spins with an angular frequency of $\omega_0 \pm \Delta\omega/2$

are excited by the RF pulse. To reverse the dephasing of spins caused by the slice-selection gradient a rephasing gradient is applied immediately afterwards.

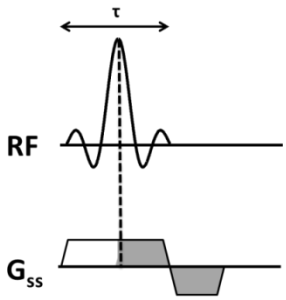

Figure 2.7: Slice selection gradient (G_{ss}) applied simultaneously with as the RF pulse. The two regions shaded in grey have the same integral for a symmetric RF pulse.

3D sequences

As previously mentioned, 3D sequences exploit phase encoding in two dimensions. Slice selection gradient are either not present or are used to select the whole imaging volume (slab). The phase encoding gradient is typically added on top of the rewinding gradient of the slice selection gradient to minimise the length of the sequence. Schematic outline of the 3D sequences used throughout this work are shown in Figure 2.9 and Figure 2.10.

2.2.2. Discrete sampling

Up to this point the representation of an object in frequency space (k) and in the image resulting from the Fourier transform have been treated as continuous functions. However, in real world MRI applications, the signal is acquired at discrete time points with an analogue /digital-converter (ADC). This means that the continuous signal emitted by the spin system will be multiplied with a sequence of Dirac-delta functions representing the sampling pattern of the ADC of the MRI system. A multiplication of the two functions in the frequency domain results in a convolution of the two Fourier transforms in the spatial domain and hence the reconstructed image is periodic, with a period $1/\Delta k$ (Figure 2.8). Δk is the spacing between any two Dirac-deltas sampling *k-space*. The Nyquist sampling theorem states that if Δk becomes larger than $1/A$ (with A being the object size) then aliasing artefacts will be seen in the image since the period (FOV) is smaller than the object itself (Figure 2.8 bottom row).

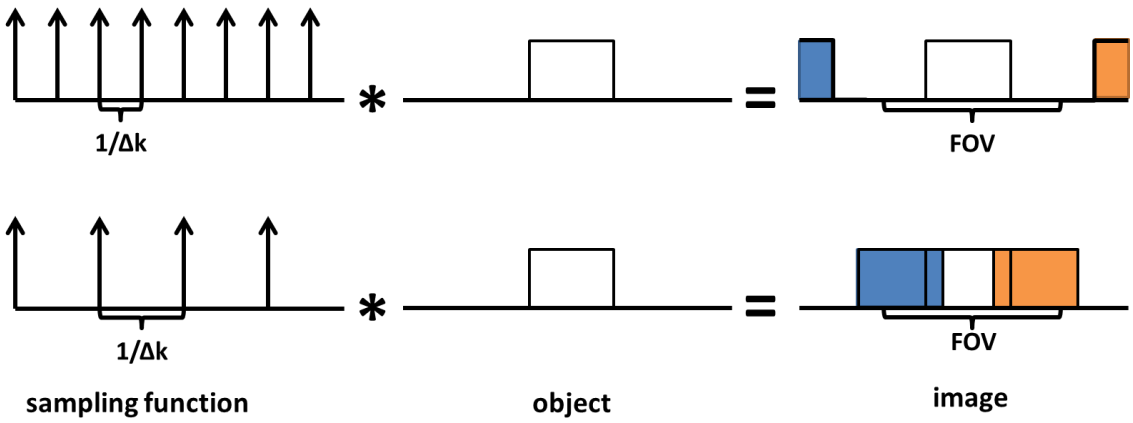

Figure 2.8: Schematic representation of sampling in 1D image space. Discrete sampling results in a convolution (*) *of the object* (*in this case a boxcar function*) *with the sampling pattern* (*a series of Dirac delta functions*). *This can cause aliasing if the sampling frequency is less than the Nyquist frequency* (*bottom row*).

2.2.3. The SPGR pulse sequence

Spoiled gradient echo sequences (SPGR) are commonly used for imaging with hyperpolarised gases. This type of sequence is also known as fast low-angle shot (FLASH) [17] and Figure 2.9 shows a schematic of the sequence diagram. The sequence employs all the above described gradients to sample k-space: slice-selection gradient (*z*), a read-out gradient (*x*) and a phase encoding gradient (*y*). The sequence diagram illustrates the gradients required for acquisition of a single line in k-space. This sequence is repeated for different phase encode steps. The time between two repetitions (measured from the middle of the RF pulse the middle of the next) is called the repetition time (TR). The time from the middle of the RF pulse to the middle of the data acquisition is the echo time (TE). The additional gradients at the end of the sequence in all spatial directions are used to spoil (dephase) any residual magnetisation before the next repetition.

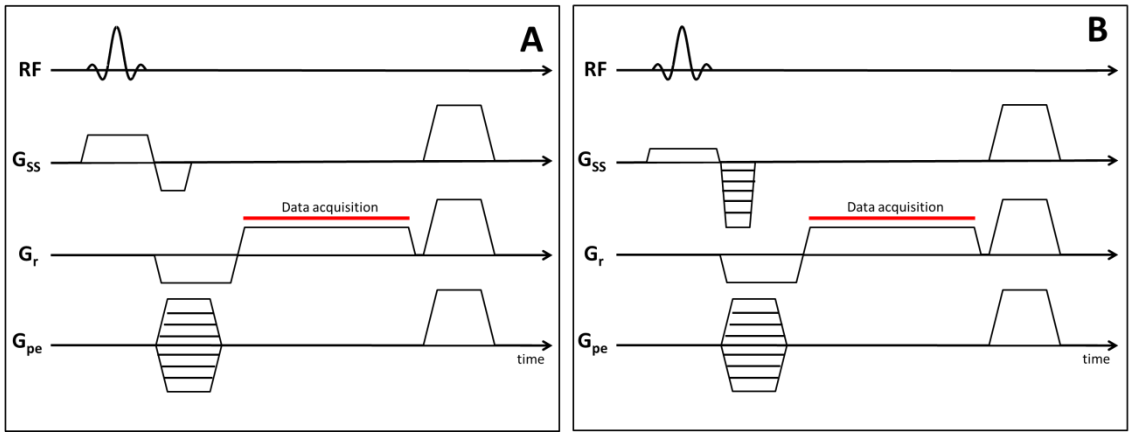

Figure 2.9: Schematic sequence diagrams: (A) of a 2D-SPGR imaging sequence and (B) of a 3D-SPGR sequence using an additional phase encoding direction.

2.2.4. The bSSFP sequence

Similar to the SPGR sequence is the balanced steady state free precession (bSSFP) sequence [18, 19]. In this sequence all gradients along each axis are balanced such that the integral of the gradients along all axes is zero (see Figure 2.10). This allows a partial rephasing of spins at the end of the repetition and therefore magnetisation is recycled and can be reused in the next acquisition. This additional magnetisation leads to higher signals and a more efficient use of available polarisation when compared to SPGR. In particular, when imaging hyperpolarised gases this can significantly increase signal to noise ratio (SNR) (see Section 2.4).

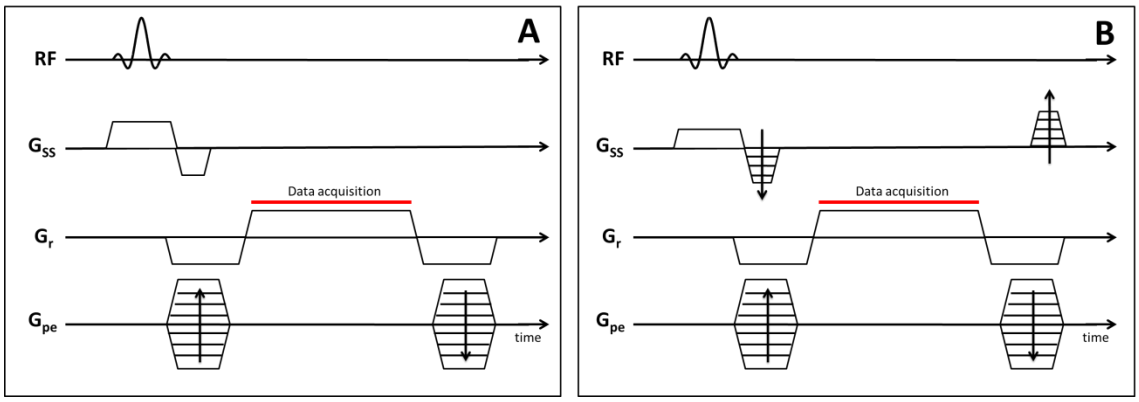

Figure 2.10: Schematic sequence diagrams: (A) of a 2D-bSSFP imaging sequence and (B) of its 3D version using an additional phase encoding direction.

2.3. Lung imaging using proton MRI

With a density of 0.1g/cm^3 the ^{1}H MR signal deriving from lung tissue is about 10 times weaker than from the surrounding tissue [20]. In addition the numerous tissue– air interfaces in the lung lead to magnetic susceptibility differences, which give rise to local field gradients. These microscopic field gradients lead to short T_2* relaxation times for ^{1}H of <2ms at B_0 = 1.5T. This makes proton imaging of the lung intrinsically challenging.

Spoiled gradient echo imaging (SPGR)

SPGR imaging is fast enough to acquire whole lung coverage MR scans within a breath-hold. As T_2* in the lungs is very short partial Fourier reconstruction [21] in the frequency encoding direction and high bandwidths (>60kHz) are typically used to ensure short TEs (~1ms) can be achieved [20]. A specific example of SPGR is presented in Chapter 3 as a method to measure the volume of the lung cavity. An example ^{1}H MR image slice from a healthy volunteer using a SPGR imaging sequence is shown in Figure 2.11A.

Balanced steady state free precession imaging (bSSFP)

bSSFP allows rephasing of magnetisation dephased by imaging gradients, however, in the presence of field inhomogeneities so called banding artefacts can be observed [20]. bSSFP is also associated with complex contrast behaviour (e.g. for short TRs the contrast is proportional to the ratio T_2/T_1 [22]). Nevertheless, bSSFP sequences provide improved SNR over SPGR sequences and have been shown to be useful to detect interstitial lung disease and morphologic abnormalities in the lung [23]. An example slice acquired from a healthy volunteer using a bSSFP sequence is shown in Figure 2.11B.

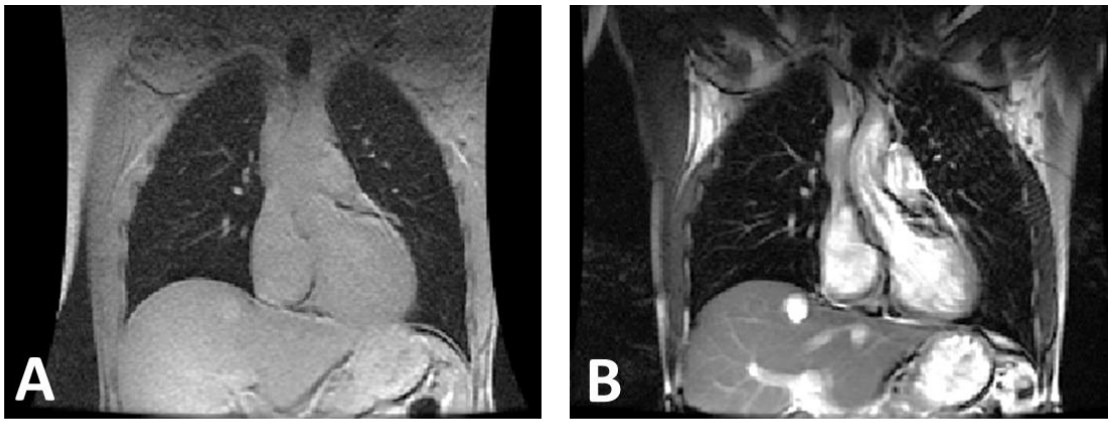

Figure 2.11: ^{1}H Lung images from a healthy volunteer: (A) ^{1}H lung image acquired with a SPGR sequence. (B) Same resolution ^{1}H lung image acquired using a bSSFP sequence. Images acquired by the hyperpolarised gas imaging group in Sheffield.

Oxygen enhanced (OE) imaging

OE imaging exploits the paramagnetic properties of oxygen, which act to shorten the T_1 of blood and tissue in the lung. When breathing pure oxygen compared against breathing air, the T_1-shortening enhances the ^{1}H MR signal [24]. Parametric maps of perfusion weighted lung ventilation can be calculated from the difference between OE and air images. Hence T_1 weighted sequences have been facilitated to measure changes in MR signal intensity when breathing pure oxygen, which can be used to map oxygen distribution by quantifying the T_1 of lung parenchyma [20]. Oxygen enhanced imaging has also been used to quantitatively measure lung ventilation using signal intensity changes from images acquired during washin and washout of oxygen [25]. Despite promising results it is still not clear to what extend those images are weighted by perfusion [20].

Fourier decomposition (FD) ^{1}H MRI

In the FD method bSSFP images of a single slice are acquired in quick succession while subjects are breathing freely. A Fourier frequency decomposition of the signal over time allows separation of perfusion weighted signal (at a frequency of typically 1Hz) from ventilation weighted signal (around 0.2Hz) caused by respiratory motion [26]. This technique has been applied to study abnormalities in expansion of lung parenchyma in patients with cancer [27] and to deduce ventilation weighted and perfusion weighted images in patients with pulmonary embolism and COPD [28]. The drawback of the method is, it is currently a single slice technique.

2.4. Imaging hyperpolarised gases in the lung

2.4.1. Introduction

As briefly discussed above, proton MRI of the lungs has challenges related to available signal. However, introducing gaseous imaging agents in the lung allows measurement of gas density and diffusion directly in the alveolar airspaces. Hyperpolarisation of spin-½ noble gases permits compensation of the low density of a gaseous spin system at body temperature and ambient pressure, allowing MR imaging with high spatial and temporal resolution. This enables the derivation of both high quality functional and structural information from images.

Most of the work presented in this thesis is based on imaging hyperpolarised ^{3}He. This stable isotope is chemically inert, non-toxic, and highly diffusive and has a low solubility in tissues. However, the finite supply of ^{3}He has caused prices to reach > $500 per litre recently [29, 30]. ^{129}Xe ($30 per litre at natural abundance) is a much cheaper alternative, although MRI with ^{129}Xe is more difficult since its gyromagnetic ratio is about 2.75 times lower than that of ^{3}He (Table

2.1). Thus images acquired with ^{129}Xe result in lower SNR with gas polarised to same levels as ^{3}He, even when using ^{129}Xe enriched xenon (^{129}Xe isotope has a natural abundance of 26.4%).

Fluorinated gases such as sulphurhexafluoride (SF_6), tetrafluorometane (CF_4), and hexafluoroethane (C_2F_6) can also be used for MR imaging due to the inherent ^{19}F nuclear spin of ½. As less expensive contrast agents they can be used in a thermally polarised state. However, imaging is therefore challenging due to the low spin-density [31]. To increase quality of images additional averages can be acquired however, this increases scan time (and hence breath-hold).

Although most of the work presented here was done using ^{3}He the same methods are directly transferable to other nuclei. In fact MBW-imaging (presented in Chapter 5) is also demonstrated using ^{129}Xe.

2.4.2. Optical pumping

^{3}He and ^{129}Xe gases are hyperpolarised by optical pumping methods through the transfer of angular momentum from circularly polarised laser light to the noble gas nucleus. There are two commonly used methods of optical pumping to achieve high nuclear spin polarisations of ^{3}He and ^{129}Xe. Metastability exchange optical pumping (MEOP) is a technique of direct optical pumping used to polarise ^{3}He, and is capable of producing high quantities of hyperpolarised gas in a short amount of time. Polarisation is transferred through metastability exchange collisions at low gas pressures [32]. Spin-exchange optical pumping (SEOP) is the second method of optical pumping and is the technique used in Sheffield for polarising both ^{3}He and ^{129}Xe [33]. SEOP is an indirect method of optical pumping by which the transfer of angular momentum occurs in two steps, using an alkali metal (usually rubidium) as an intermediate to transfer polarisation to the noble gas. The SEOP process takes place in a glass cell heated to approximately 100°C to vaporise the rubidium (Rb). Circularly polarised laser light at a wavelength of $\lambda = 795nm$ induces a transition from the 5S1/2 ground state to the 5P1/2 state. Due to the circular polarisation of the laser light, the electrons preferentially build up on the 5S+1/2 ground state, causing polarisation '↑'. The Rb electrons can then transfer their polarisation to the noble gas nuclear spin through collisional spin exchange [33]. The result is a net transfer of angular momentum from the circularly polarised light to the nuclear spin system. This process is schematically shown in Figure 2.12 [14].

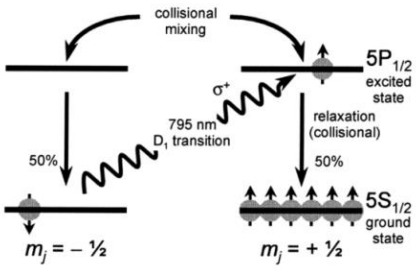

Figure 2.12: Representation of the optical pumping process. Left circularly polarised light (σ+) at a wavelength λ=795nm, resonant with the D_1 transition in Rb, excites the valence electron spins from the m_j = -1/2 ground state of the $5S_{1/2}$ state into the m_j = +1/2 $5P_{1/2}$ excited state. Through collisions the excited electrons relax to repopulate both ground levels. Because there is no removal of electrons from the m_j=+1/2 state a polarisation build up is formed. Figure taken from Moeller et. al. with permission [14] © by John Wiley and Sons.

In Sheffield, commercial polarisers (MITI, Durham, NC, USA and GE Healthcare, Amersham, UK) are used to hyperpolarise ^{3}He (and were used for this project). Approximate ^{3}He polarisation levels of 25% are obtainable using this system. A schematic showing the key components of a ^{3}He polariser is shown in Figure 2.13. In Sheffield, ^{129}Xe is polarised using a home-built SEOP polariser [34]. In the current implementation ^{129}Xe polarisations of up to 40% can be routinely achieved. After hyperpolarisation the gases are collected in Tedlar bags (Jensen Inert Products, Coral Springs, FL, USA) and mixed with nitrogen as a buffer gas prior to application in subjects.

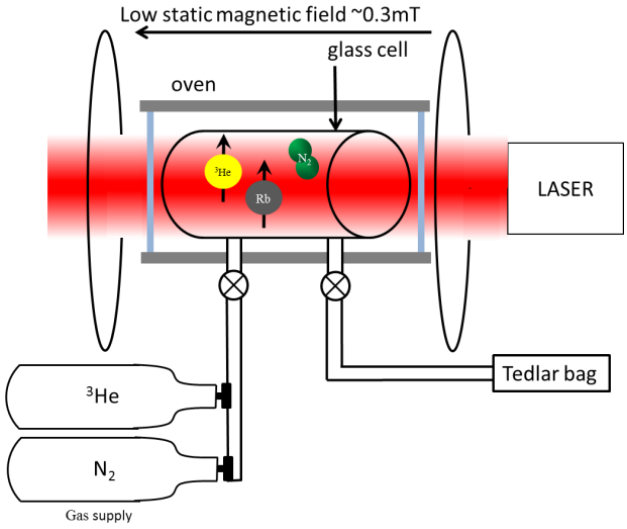

Figure 2.13: Schematic of a Helium-3 polariser. Static magnetic field is required to cause Zeeman splitting; The oven heats the glass cell to vaporise the rubidium; the laser provides circularly polarised light through optics. The glass cell has a gas inlet (for ^{3}He and N_2), the outlet can be connected to a Tedlar bag to deliver gas for MRI scanning.

2.4.3. Imaging hardware

In hyperpolarised gas MRI, because the polarisation is produced using optical pumping, it is independent of the field strength B_0 (unlike ^{1}H imaging, where SNR increases with B_0). The effects of B_0 on SNR and spatial resolution are more complex in the case of hyperpolarised gas MRI compared with ^{1}H MRI [35, 36]. In fact, lower field strengths have been demonstrated to be effective for imaging hyperpolarised gases due to longer transverse relaxation times versus higher field strengths [37]. Nevertheless, in clinical application, systems with higher field strength (1.5T and 3T) are most common due to the higher ^{1}H SNR. In this thesis all imaging studies were performed on a 1.5T GE Signa HDx system (GE, Milwaukee, WI, USA).

In this work three different transmit/receive RF coils were used for imaging of hyperpolarised gases. Two quadrature vest coils tuned to the ^{3}He Larmor frequency at 1.5T (48.62MHz) in two different sizes; an 'adult' coil: Clinical MR Solutions, Milwaukee, WI, USA, see Figure 2.14A; and a 'small' coil: Picker, Cleveland, OH, USA. To image ^{129}Xe a dual-tuned quadrature coil, tuned to the frequency of both ^{3}He and ^{129}Xe (17.65MHz at 1.5T) was used [38]. This coil is shaped like a bib (see Figure 2.14B).

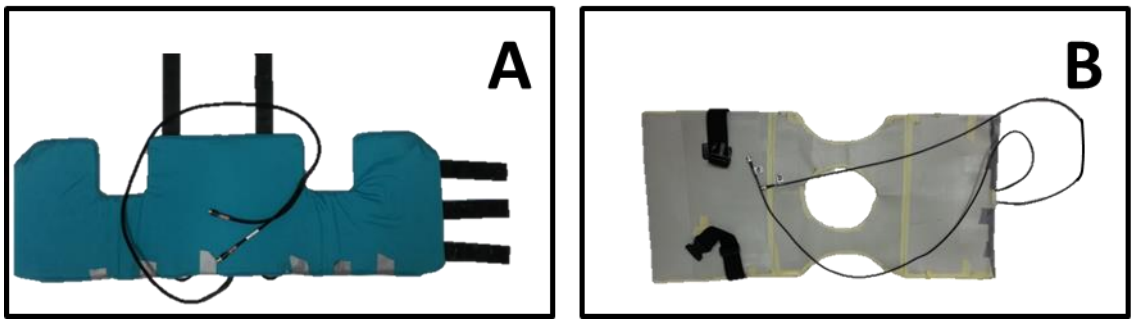

Figure 2.14: (A) Adult sized coil used for imaging studies with hyperpolarised ^{3}He (frequency 48.62MHz). (B) Home-built dual-tuned (48.62MHz (^{3}He) and 17.65MHz (^{129}Xe)) flexible transmit-receive coil [38].

2.4.4. Sequence considerations

MR imaging of hyperpolarised gases is challenging since the polarisation (unlike in ^{1}H imaging) is always in a non-equilibrium state and decays in a non-recoverable manner over time and with each RF pulse. In addition, the image acquisition is further restricted by the duration of a breath-hold. Thus, image acquisition time is the most crucial parameter to consider when designing MR imaging strategies for imaging the lungs with hyperpolarised gases.

The longitudinal magnetisation of a hyperpolarised gas relaxes towards the thermal equilibrium value with a time constant T_1. In the absence of paramagnetic oxygen or other paramagnetic impurities the T_1 of ^{3}He and ^{129}Xe can be many hours [39]. However, in the presence of oxygen the T_1 shortens dramatically and upon inhalation in the lung T_1 is ~20-30s. The inverse of T_1 is linearly related to partial oxygen pressure:

$$pO_2 = \frac{\xi}{T_1} \qquad \text{Eq. [2.21]}$$

At room temperature the proportionality constant ξ has been empirically determined to be 2.61bar·s for ^{3}He [40]. This low T_1 value places restrictions on acquisition time. In addition, the high self-diffusion of noble gases ($D_{0\text{-}3He}$ = 1.85cm^2·s^{-1} and $D_{0\text{-}129Xe}$=0.058cm^2·s^{-1} [41]) compared water protons contributes to an increased signal attenuation due to Brownian motion of the gas atoms in the presence of magnetic field gradients.

SPGR sequences (see Section 2.2.3) are most commonly used to image hyperpolarised gases [42]. The use of low flip angles preserves non-recoverable magnetisation throughout acquisition of *k-space*. Strong spoiler gradients after each data acquisition act to dephase residual transverse magnetisation, preparing the spin-system for another data acquisition and allowing minimal TR. This spoiling is necessary for hyperpolarised gases to avoid interference of residual magnetisation with the subsequent acquisition (since T_2^* relaxation can be relatively long with ~30ms for ^{3}He and ^{129}Xe at 1.5T [36, 43]). The transverse magnetisation used for imaging hyperpolarised gas can be described as a function of acquisitions number (or RF pulse) n as follows:

$$M_{xy}(n) = M_0 \cdot \cos(\alpha)^{n-1} \cdot \sin(\alpha) \cdot e^{-\frac{(n-1)\cdot TR}{T_1}} \qquad \text{Eq. [2.22]}$$

For sequential Cartesian sampling of k-space, the optimal flip angle therefore be derived by maximising the signal at the centre of k-space is [42]:

$$\alpha_{opt} = \arctan((N/2-1)^{-1/2}) \qquad \text{Eq.[2.23]}$$

for N total phase encoding steps. Nevertheless, using constant flip angle will continually deplete the transversal magnetisation available for imaging with each data acquisition, leading to blurred images, since the edges of *k-space* along phase encoding direction are acquired last [42].To maximise the use of available magnetisation a variable flip angle (VFA) scheme can be applied [44]. This reduces the effects of *k-space* filtering by maintaining a constant transverse magnetisation for each phase encoding step. VFA requires a careful calibration of the flip angle,

such that the magnetisation is not completely used up before the whole of *k-space* has been acquired.

As introduced in Section 2.2.4, bSSFP sequences offer increased SNR (using balanced gradients) at the expense of banding artefacts for high B_0 inhomogeneity or incorrect centre frequency calibration. In Chapters 3 and 8, bSSFP imaging is used to reduce the delivered gas dose, maximise SNR and/or increase the spatial resolution of hyperpolarised gas images.

For advanced application fast non-Cartesian sequences [45, 46] and also image acceleration techniques such as parallel imaging with 32-channel coils for ^{129}Xe and ^{3}He [3, 47] and compressed sensing have been developed in the past years [6]. Fast imaging has been shown useful to increase the temporal resolution of imaging [48] or to obtain different functional information in the lung in a single acquisition [49].

2.4.5. Flip angle calibration

When imaging hyperpolarised gases it is crucial to calibrate the flip angle accurately for the particular coil and loading used. In the case of the bSSFP sequence (presented Chapter 4) and the SPGR sequence (Chapter 5) used for ventilation imaging, flip angles must be optimised for the given resolution of the images and any deviation from the optimum would result in a penalty on image SNR [42].

To calibrate the flip angle a number of FIDs (~50-200) are acquired after inhalation of a very small dose of hyperpolarised gas (<50ml, topped up with N_2 to fill a Tedlar bag). The decay in hyperpolarised gas signal over *n* acquisitions can be used to solve for the flip angle (assuming T_1 decay is negligible, sequence TR<<T_1):

$$e^{\frac{\ln(S(n))-\ln(S(0))}{n-1}} = \cos(\alpha) \qquad \text{Eq. [2.24]}$$

2.4.6. Ventilation imaging

The expression ventilation imaging is used routinely in this work for MR imaging performed during breath-hold after an inhalation of a single dose of hyperpolarised gas. Ventilation images are typically acquired using SPGR or bSSFP sequences in 2D or 3D (example slices from a healthy volunteer are shown in Figure 2.15). While 3D sequences have been shown to result in improved SNR, patient motion can lead to artefacts that would affect all slices [50]. Signal intensity in ventilation images directly reflects the gas volume in each voxel (spin density contrast), but is additionally weighted by effects of T_1, T_2^* decay and coil sensitivity profile.

Ventilation imaging has been demonstrated in many different lung diseases in the past, such as CF [51, 52], COPD [53, 54], asthma [55, 56] as well as in smokers [57]. Particularly, ventilation imaging is sensitive to obstructive lung disease, where in regions of the lung with poor ventilation have low ^{3}He or ^{129}Xe gas signal. Figure 2.16 shows example slices from patients with those lung diseases alongside with the lung of a healthy smoker (all pulmonary function tests in the smoker were in the normal range). Specific details of the diseases themselves will be discussed later (Section 2.5.4). Furthermore, quantitative metrics of lung function can be derived from ventilation images as described in Chapter 3 and 4.

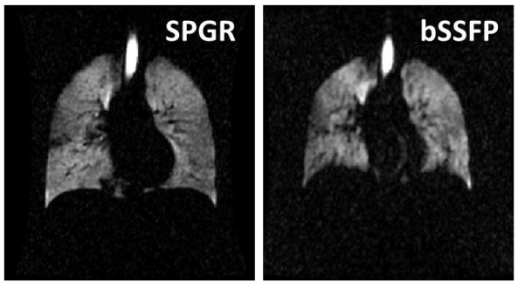

Figure 2.15: Ventilation images of the same subject (and same slice) using 2D-SPGR (left) and 3D-bSSFP (right) hyperpolarised ^{3}He MRI. NB: For SPGR images 300ml of ^{3}He was used, compared to 100ml for bSSFP imaging. Minor artefacts from cardiac motion can be seen in the centre of the 3D-bSSFP image. Images acquired by the hyperpolarised gas imaging group in Sheffield.

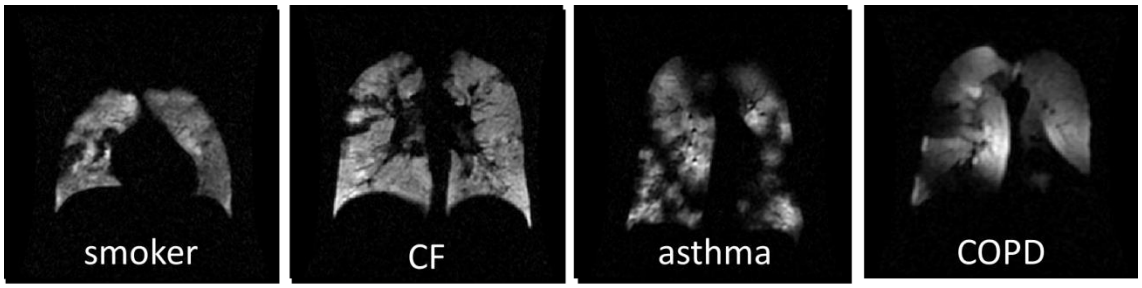

Figure 2.16: Example slices from a smoker, a patient with CF, asthma and COPD acquired with 2D SPGR ventilation hyperpolarised ^{3}He MRI. Images acquired by the hyperpolarised gas imaging group in Sheffield.

2.4.7. Diffusion weighted imaging

Hyperpolarised gas imaging can be used to probe lung microstructure via the application of diffusion weighted gradients. The diffusion of the inert tracer gas (usually ^{3}He) in the complex structure of the lung is confined by the walls of the alveoli. To estimate the apparent diffusion

coefficient (ADC) of ^{3}He, two sets of ventilation images are required with the exact same timing: one with diffusion weighting gradients, and one without. From the difference in measured signal intensity between the two sets of images and knowledge of the gradient waveform and duration (b-value), ADC values can be calculated. Hence ADC maps of the lungs can be generated; this has enabled quantification of tissue destruction in emphysema for example, on regions where the ADC is large [58]. In the literature mathematical models have been proposed to draw conclusions about lung microstructure from measurements of different diffusion length scales. The so-called cylinder model treats the alveolar ducts as infinitely long cylinders isotropically oriented in space [59]. Application of this model to ^{3}He ADC data permits estimation of lung microstructural parameters e.g. alveolar duct diameter. However, it has been shown that acinar branching and the finite length of the airways have a significant influence upon the ^{3}He diffusivity [37] and recently a method based solely on fractal exponential analysis (independent of modelling) has been developed [60].

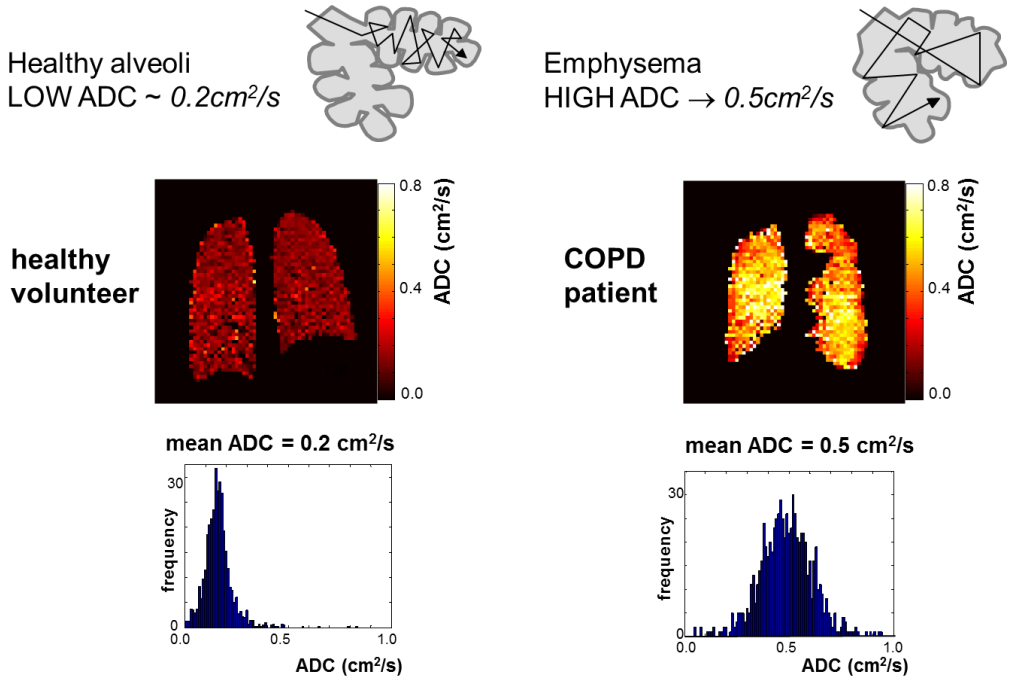

Figure 2.17: ADC maps of a healthy volunteer (left) and a COPD patient (right). High ADC values indicate structural damage to the lung tissue/alveolar walls in the COPD patient as shown in the schematic on top. Images acquired by the hyperpolarised gas imaging group in Sheffield.

2.4.8. Imaging of partial oxygen pressure

As presented in Section 2.4.4, Saam. et. al. discovered an inverse linear dependence of T_1 with partial oxygen pressure pO_2 (see Eq. [2.21]) as mentioned before [20]. Therefore measurement of the T_1 of hyperpolarised ^{3}He allows determination of alveolar pO_2. In order to properly calculate the pO_2, RF depolarisation of the hyperpolarised gas signal must be separated from the oxygen

induced signal decay. A minimum of three subsequent imaging acquisitions is therefore necessary. The time evolution of alveolar pO_2 can be followed over multiple time points using a method of acquiring two series of images as first demonstrated by Deninger et al.[61]. More recent methods use only one single breath-hold to obtain regional maps of pO_2 [62, 63]. These methods require the assumption that pO_2 decay in the lung is linear with time. This might be true for short breath-holds, but recent work has suggested an exponential fitting of the ^{3}He signal decay might be more accurate for longer breath-holds [64].

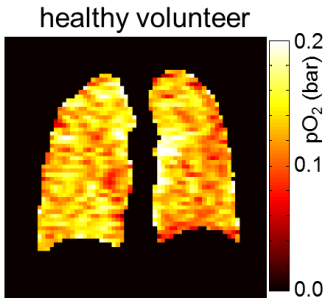

Figure 2.18: Map of regional pO_2 measured in the lungs of a healthy volunteer obtained with hyperpolarised ^{3}He MRI. Average pO_2 is 150mbar, in agreement with literature values [65]. Images acquired by the hyperpolarised gas imaging group in Sheffield.

2.4.9. Conclusion

Over the past 20 years hyperpolarised gas MRI has become established as a comprehensive tool with a multitude of methods to probe different functional and structural aspects of the lung. Despite major improvements in sequence design and of polarisation technology expectations of bringing this technique into the clinical routine have yet to be fulfilled. In parts this might be attributed to the cost of ^{3}He, but future research must also focus on the definition of new quantitative measurement methods and metrics that underline the additional value that the increased sensitivity and regional insight into disease processes offered by hyperpolarised gas imaging can add to standard pulmonary function tests.

Finally, a wide variety of methods and derived metrics have been developed over the past few years. Methods such as phase contrast velocimetry to measure flow [66] or chemical shift saturation recovery of ^{129}Xe to measure alveolar wall thickness [67] are just two examples of the broad spectrum of promising applications using hyperpolarised gas MRI, and there are many more that cannot be covered in this thesis.

2.5. Pulmonary Function Testing

2.5.1. Pulmonary structure

The lungs fill most of the thorax and are of a complex design. They are divided into a right and a left lung each situated in its own pleural cavity. Each lung is sub-divided into lobes, the left lung into 3 (upper, middle and lower lobe) and the right lung, being smaller, into 2 lobes (upper and lower). The biggest airway, the trachea, splits into the left and right primary bronchi, which then divide in the same dichotomic pattern. In total a network of about 23 generations of dichotomic bifurcations is found in the lungs. A schematic of the lung is shown in Figure 2.19A.

Figure 2.19: (A) shows schematically an overview of the lung. (B) is a schematic of a network of alveoli. Copyright by Churchill Livingstone Elsevier [68].

This network of airways is divided into:

(a) **conducting airways**, which do not participate in gas exchange, but lead the gas to the respiratory zone. Together they constitute the total anatomic dead space with a volume of about 150 ml.

(b) **transitional and respiratory zone**, consisting of acini with respiratory bronchioles bifurcating 6 generations into alveolar sacs at the end. In the respiratory zone gas exchange is taking place between alveoli filled with gas and capillaries filled with blood (Figure 2.19B).

A schematic model of the generations of the lung derives from the pathological analysis of Haefli-Bleuer and Weibel and is schematically shown in Figure 2.20 [69]. In addition to these two functional zones, small airways are often referred to as peripheral airways and represent generation 8-23 with an airway diameter of less than 2mm in healthy adults [70].

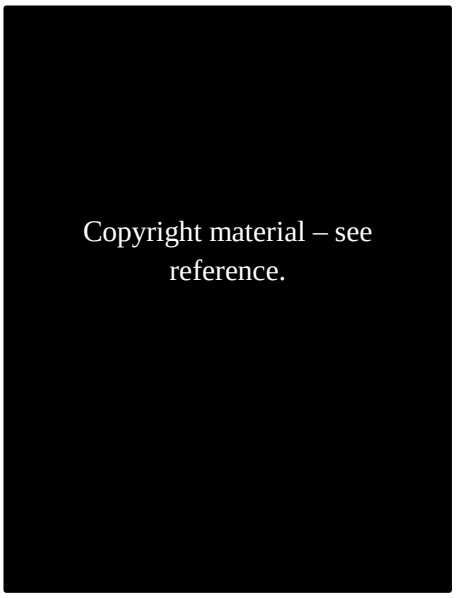

Figure 2.20: *Schematic structure of the human airways from Weibel. Z generations of dichotomic bifurcations are divided in conducting zone (Z=1-16) and transitional and respiratory zone (Z= 17-23). Reproduced with permission from [65]. Small airways are defined as airways with diameter <2mm (in adults Z=8-23). Reproduced with permission of Wolters Kluwer Lippincott Williams & Wilkins.*

2.5.2. Pulmonary volumes

Figure 2.21 shows a lung volume-time spirogram with the most important lung volumes schematically indicated: the functional residual capacity (FRC) is the end-expiration volume during relaxed breathing and represents a physiological equilibrium between the outward pull of the chest wall and the inward elastic recoil of the lungs. The residual volume (RV) is the volume of air left in the lungs after a complete expiration. The total lung capacity (TLC) is the volume of maximum inflation level that can be pushed into the lung after a complete inhalation. During normal breathing the tidal volume (TV) is measured as volume of air displaced at no extra effort.

Lung inflation during imaging with hyperpolarised gas MRI is related to the above mentioned pulmonary volumes. For imaging, a reproducible lung volume is crucial for comparison of ventilated volumes in longitudinal studies. FRC as the relaxed end-exhalation volume of the lung is thought to be reproducible and serves as the initial state before inhaling a fixed volume of a gas mix containing the hyperpolarised tracer for imaging. Therefore most images are typically acquired at FRC+1 (functional residual capacity plus 1 litre). The 1 litre derives from the size of the filled Tedlar bags routinely used to transport the hyperpolarised gases from the production site to the scanner. In addition, throughout this work LV is used for the end-inspiratory lung volume (~FRC+TV).

Figure 2.21: *Volume-time curve of tidal breathing (FRC=functional residual capacity) followed by a complete exhalation to residual volume (RV) and inhalation to total lung capacity (TLC). Expiratory reserve volume (ERV), inspiratory capacity (IC) as well as inspiratory vital capacity (IVC) are derived from this curve. Adapted version reproduced with permission of the European Respiratory Society © Eur Respir J March 2013 [71].*

2.5.3. Lung function

Before explaining the primary function of the lung, which is gas exchange with the blood, the mechanism of how gas gets to the alveoli needs to be addressed. Ventilation is the process of gas turnover via inhalation and exhalation in order to transport oxygenated air into the lung and remove deoxygenated air. Gas turnover is the movement of air along pressure gradients generated by volume changes of the respiratory system. Those pressure gradients are created by volume changes of the expandable lung tissue. Volume changes are the response to the summation of forces applied to lung and chest wall from respiratory musculature that combine to drive the air into and out of the lung. The continuous turnover of gas in the lungs supplies the lung with oxygen and transports air with increased carbon dioxide away. The difference of gas concentration in the blood and alveoli creates pressure gradients leading gas to diffuse through lung tissue of approximately 0.3µm thickness: Oxygen diffuses into the blood and CO_2 into the alveoli. Under normal conditions (tidal breathing of air) gas exchange depends on three major factors: (a) the thickness of the alveolar-capillary wall (b) the mixture and concentration of the gases present in the lung and (c) the volume of blood available for gas exchange. Different lung diseases can affect these pathways individually, by different pathophysiological mechanisms resulting in a less efficient gas exchange [65, 72].

2.5.4. Lung disease

A number of diseases influence gas exchange directly or indirectly. Thickening of the alveolar-capillary walls leads to a prolonged gas exchange due to increased septal diffusion times (i.e.

from fibrogen deposition in idiopathic pulmonary fibrotic disease). Indirect effects on gas exchange include ventilatory dysfunction and diseases involving the pulmonary vasculature, where capillary uptake is altered by impaired cardiopulmonary circulation. The focus of this work is on heterogeneous ventilation related to airflow obstruction.

In obstructive lung disease airflow and ventilation are regionally impaired. This causes an inhomogeneous distribution and mixing of gas in the lung commonly referred to as ventilation heterogeneity (VH). Ventilation is known to be heterogeneous in healthy volunteers and increase with age [73]. VH increases considerably in obstructed lungs with airway narrowing or blockage and resulting in an insufficient supply with fresh gas. As a result of a reduced turnover of gas, the lack of oxygen and increased CO_2 levels influence gas exchange efficiency. Therefore patients with severe obstructive airway disease cannot supply alveoli with enough oxygen and suffer from breathlessness. Obstructive lung diseases are the target of studies presented here and the quantitative imaging methods discussed throughout this work are sensitive to changes in ventilation. Techniques presented in Chapter 3, 4 and 5 are tested on an asthma and a cystic fibrosis cohort.

Asthma

Asthma is a chronic inflammatory pulmonary disease characterised by reversible obstruction of airways as a result of bronchial hyper-responsiveness [74]. Obstruction leading to restricted airflow derives from reversible bronchoconstriction, inflammation of the airway walls and chronic mucus plugging [75]. Starting in the peripheral airways, the inflammatory process can result in remodelling of the airways, if not detected early [76, 77]. The hyper-responsiveness of airways to different direct (histamine, methacholine) and indirect stimuli (exercise, cold or dry air) results in bronchoconstriction as a response to inflammatory mediators [78].

Cystic fibrosis

Cystic fibrosis (CF) is a genetic disorder that affects function of liver, pancreas, intestine and the lungs. About 1 in 2500 children is diagnosed with this life-shortening disorder in Causcasian people [79]. CF patients do not possess a working copy of the gene for the protein cystic fibrosis transmembrane conductance regulator that is needed to regulate components of mucus, sweat and digestive fluids. This mutation results in build up of mucus in the lung, leading to airway blockage and inflammation. Despite early detection through new-born screening and advances over the past decades, life expectancy of CF patients is with a median of 36.6 years (in the UK in 2013) much lower than healthy subjects [80]. An early detection of increased ventilation heterogeneity is crucial to decide on treatment pathways.

COPD

Chronic obstructive pulmonary disease is characterised by irreversible airflow obstruction. Its prevalence is increasing majorly caused by effects of smoking [81]. COPD is used as an umbrella term to describe a disease encompassing chronic bronchitis and emphysema and most patients have elements of both conditions [82]. Chronic bronchitis can derive long term exposure with cigarette smoke or other inhaled irritants and is associated with structural narrowing of the small airways because of chronic inflammation. Emphysema is characterised by destruction of airway walls in the distal airways of the respiratory zone, loss of elastic recoil and rapid airway closure on expiration [74, 83]. As late diagnosis and under-treatment are seen as one of the major causes for high mortality from COPD an early detection and treatment is important to improve the long-term prognosis to prevent irreversible losses of lung function [82].

2.5.5. Measuring respiratory function

Respiratory function can be directly measured using a variety of breathing tests performed at rest and during exercise. These tests can be used to assess: (1) airflow through the respiratory tract [71, 84]; (2) gas distribution throughout the airways [73, 85, 86]; (3) the efficiency of gas exchange [65]; just to name the most important ones. Some measures, such as spirometry, are well established and are commonly used in clinical practice and clinical trials. Others are less established but have great potential to be useful in the future, such as the multiple breath washout test (MBW), which measures behaviour of tracer gases in the lung. In the following a brief overview is given of lung function tests used in this thesis as comparison to functional imaging metrics.

2.5.5.1. Flow derived metrics - spirometry

Spirometry is the measurement of flow and lung volumes. Modern spirometry uses a pneumotachograph deriving flow and volume from pressure differences measured with sensors at the mouth. The following parameters are usually reported from spirometry [84]: FEV1, the forced expired volume in one second, and FVC, the forced vital capacity. In addition, maximum flow-volume loops (MFVL) are acquired for visual recognition of typical disease patterns. Two flow-volume loops acquired during spirometry are shown in Figure 2.22. Example A of that figure is a healthy volunteer with a predicted FEV1 of 109% [71]. Example B displays the MFVL of a subject of similar height and weight with a significantly reduced FEV1 (25%), indicating severe airflow limitation as found in obstructive pulmonary diseases. In addition this patient has a severely decreased FVC (compare flow-volume loops of A and B) with a flat flow in the second

half of the expiration suggesting slow emptying due to airway obstruction. Those curves demonstrate the information content of this test. In addition spirometry is cheap and due to portable design of machines it can be brought to the patient. On the other hand spirometry is highly effort dependent with respect to the patient's ability to perform forced exhalations.

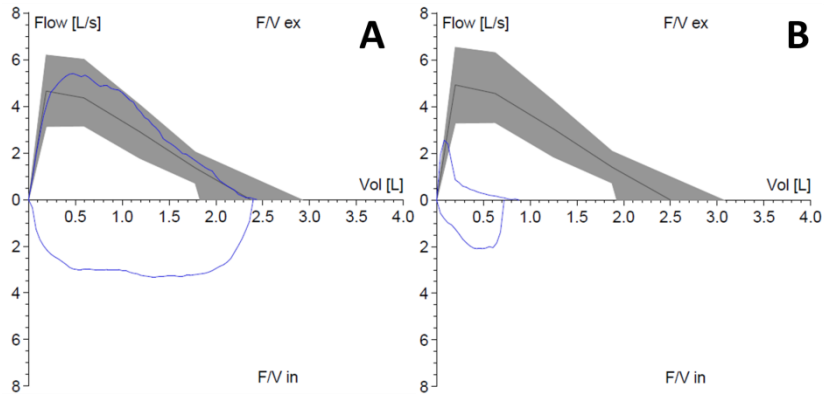

Figure 2.22: (A,B) Maximum flow-volume loop (MFVL) of a normal subject. Negative flow (bottom part) represents a full inhalation to TLC and positive flow represents a complete forced exhalation to RV. In a normal subject, flow reaches its maximum relatively instantaneously (during a forced manoeuvre) and then continues to decline in a relatively linear fashion during exhalation to RV. In grey are 95% confidence intervals of a healthy population, the blue line shows the course of each individual. (A) shows flow-volume loop from a healthy volunteer (10years,145cm,38kg) while (B) is from a CF patient (16 years,148cm,45kg). Reproduced with courtesy of Laurie Smith from Sheffield Children's Hospital.

2.5.5.2. Lung function testing using tracer gases – inert gas washout

Tracer gas dilution tests to derive lung volumes have been used for 200 years [87]. More recently dilution techniques have been used to derive metrics of lung function. Those lung function tests are used to derive metrics of gas transfer [65] and ventilation heterogeneity (VH) [73, 88-90]. The focus of this work is on obstructive lung diseases and therefore measures of VH are discussed in the following.

Airways smaller than approximately 2mm luminal diameter are referred to as the 'silent lung zone' [91]. These peripheral airways are to approximately the last 5-6 generations of airways. The accumulated cross-sectional area of this zone is several orders of magnitude larger than in the major airways and hence the flow velocity is much lower than in the conducting airways. Its contribution to the total resistance was estimated at only 10% [70, 92]. Forced expiratory flow in one second (FEV1) reflects airway resistance and therefore largely represents the function of the larger airways. Small airways with a low overall resistance are not represented, making

spirometry a less sensitive test for detecting changes in the small airways. This has systematically been proven in animal experiments [93]. In cystic fibrosis (CF) it has been shown that the early lung changes occur peripherally in small airways [94]. FEV1 is broadly used in CF to assess lung function, but other methods have been suggested as more sensitive measures of early changes [92, 95]. By the time a change in FEV1 is detected the disease has already caused major damage [96-99]. Similar peripheral airway restructuring has also been verified in asthma and chronic obstructive lung disease (COPD) [100]. Also early emphysema related to smoking damage of the alveoli can go undetected by spirometry. Therefore alternative lung function testing has been suggested for early detection of those diseases [95].

Inert gas washout (IGW) as a measure of gas mixing efficiency is used to assess VH. IGW was described as a pulmonary function test in the first half of the last century [101]. Instead of using flow or volumes as a surrogate of ventilation efficiency, the gas composition is measured using inert gas washout upon single or multiple exhalations. While Darling et al. [101] were interested in the process of 100% oxygen replacing the present alveolar nitrogen their colleagues Mundt et al. looked into the feasibility to measure the composition of alveolar gas in a single breath [102]. With those two publications, the basis of the two principal IGW tests was laid: single breath washout (SBW) and multiple breath washout (MBW). Both lung function tests sample the composition of exhaled gases - one over a single breath (SBW) the other over multiple breaths (MBW). Therefore they both rely on accurate measurement of gas composition with a high temporal resolution. The introduction of mass spectrometers into respiratory research made precise measurement of gas concentrations feasible for clinical practice [103]. Due to the capability to directly measure partial mass of more than one gas with a good temporal resolution, the mass spectrometer still remains the gold standard [104, 105]. Today's development of reliable IGW systems with enhanced optical and acoustic sensors has increased the interest in this lung function test. The user friendly compact systems have been validated against mass-spectrometry using SF_6 [95] and N_2 [106, 107] as tracer gases. In the following SBW and MBW are described in further detail.

Single breath washout (SBW)

Single breath washout measures concentration change of a tracer gas during a single expiration. Most commonly nitrogen concentration is sampled over a full expiration to RV after a single inspiration of 100% oxygen [89]. Figure 2.23 shows the result of a SBW from a healthy volunteer. The N_2 concentration is plotted against accumulated exhaled total gas volume. The curve is divided into 4 phases: phase I, where the inhaled oxygen has completely washed out all N_2 and therefore no concentration of N_2 is measured; phase II (the bronchial phase) with a fast rising N_2

concentration leading to phase III the alveolar phase and finally phase IV of the washout referred to as closing volume with a fast rising slope. From each phase different parameters have been derived: phase I & II is used to calculate Fowler-dead space [108], phase III, a slope (phase III slope) as a measure of VH [109], phase IV measuring the closing volume (CV) [110].

Figure 2.23: SBW after single inhalation of 100% oxygen. Dead space is derived from phase I, phase II is the bronchial phase with a rising N_2 concentration until phase III with a constant slope (alveolar phase, 25-75% of exhaled volume) used to derive ventilation heterogeneity (S_{III} as the dotted line) and phase IV as the fast rising end of expiration used to derive the closing volume (CV). Reproduced with permission of the European Respiratory Society © Eur Respir J 2013 [105].

Multiple breath washout (MBW)

Multiple breath washout (MBW) was established more than 70 years ago [111] and has gained popularity in recent years. It has been successfully tested for sensitivity to changes in disease in different patient populations such as cystic fibrosis [95, 97, 98, 112, 113], asthma [114] as well as chronic obstructive pulmonary disease (COPD) [115] and asymptomatic smokers [116].

Methods

MBW measures the concentration decay during gas washout over multiple breaths. The observed tracer gas can either be naturally present in the air (e.g. N_2) or an exogenous tracer gas washed in to the lungs before MBW (e.g. SF_6). Due to the easy access to oxygen, N_2 washout using wash-in of 100% oxygen is broadly used in the clinic. Nevertheless, up to this point it is still not clear to which extent nitrogen dissolved in tissue and blood influences the outcome of a MBW

measurement. In recent work it has been shown to significantly alter the outcome of metrics derived from MBW [117]. Therefore, in this thesis all MBW tests were performed using SF_6 washout. MBW was performed in compliance with the ERS-ATS guidelines [105]. For the purposes of this work MBW was performed using a modified photoacoustic analyser (Innocor, Innovision, Glamsbjerg, Denmark) and SF_6 as the tracer gas mixed with air as (0.2% SF_6 in the gas mix) [95]. The experimental setup is shown in Figure 2.24A. A gas cylinder provides air mixed with the tracer gas (red), the analyser records flow and tracer gas concentration (blue). A fan prevents rebreathing of tracer gas during the washout (green). Figure 2.24B shows the setup at the patient's mouth in greater detail. During an initial phase of the MBW, the SF_6/air mix is washed into the lungs until equilibrium is reached between the concentrations of inhaled and exhaled gas. The difference between inspirational concentration and exspirational concentration should be less than approximately 0.1‰. Afterwards the flowpast[2] (marked with a red square, Figure 2.24B) is removed to allow the subject to breathe air. This enables the washout of SF_6 from the lungs. The washout of SF_6 continues until the SF_6 concentration has fallen below $1/40^{th}$ of the concentration at the end of the tracer gas washin phase. The resulting recordings of flow and tracer gas concentration during a MBW are shown in Figure 2.25.

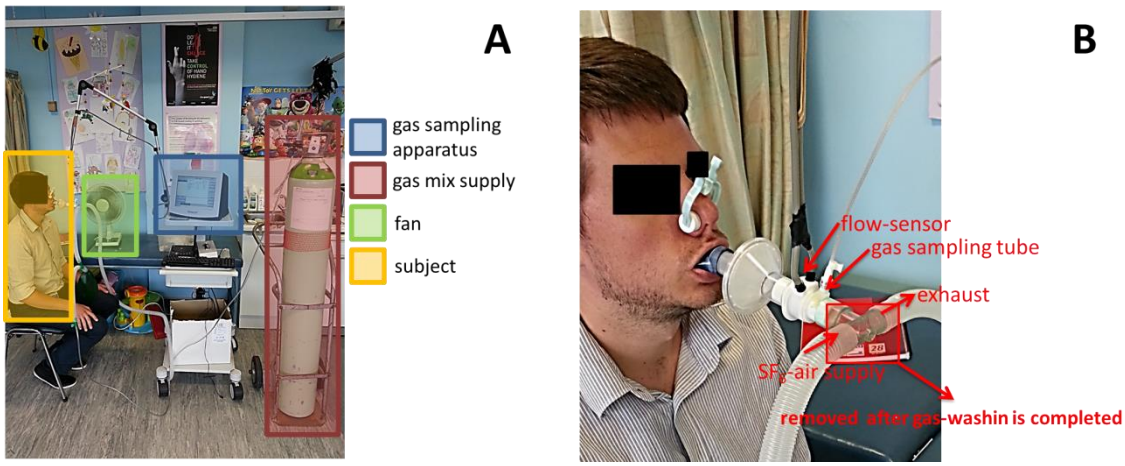

Figure 2.24: *(A) Setup of a MBW experiment. (B) Detailed view of system setup.*

[2] A flowpast is a t-piece with a tube supplying constant gas flow attached at one side, an exhaust on the opposite side and the subject breathing from the third side (Figure 2.24B). A constant flow higher than the maximum inspiratory flow assures that the gas mix supplied at the inlet is inhaled by subjects.

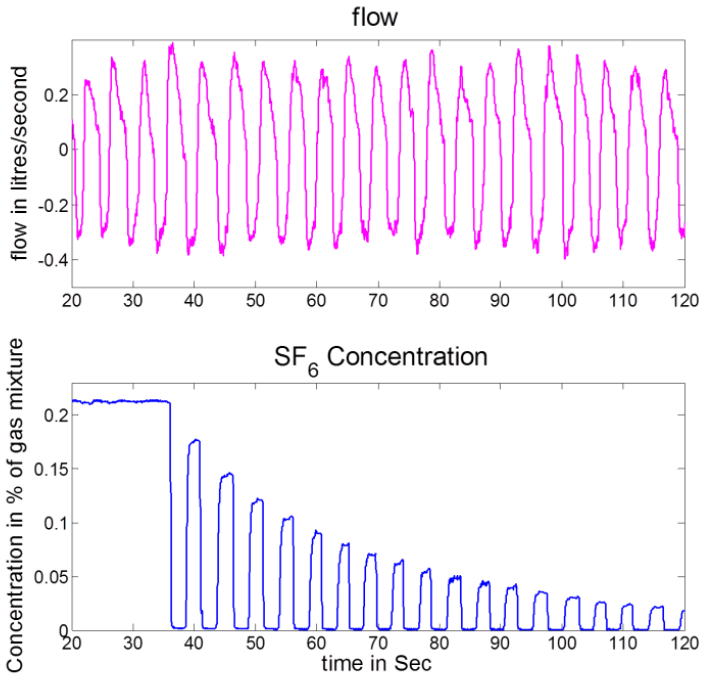

Figure 2.25: *Recording from an SF_6 MBW in a healthy volunteer. Top figure: flow-time curve acquired during experiment to calculate accumulated exhaled volume. Bottom figure: tracer gas concentration over time. After wash-in to equilibrium concentration, the tracer gas supply is disconnected and the washout begins (approximately at t=33s).*

The lung clearance index (LCI)

A variety of metrics have been derived from MBW to probe ventilation heterogeneity [73, 118-120]. The most widely used is the lung clearance index (LCI). LCI is calculated as the amount of lung turn-overs (ratio of accumulated expiratory volume to FRC) needed to reduce end tidal tracer gas concentration (Cet[3]) to 1/40th of its initial values [121]:

$$LCI = \int_{t=0}^{t_{end}} \frac{V_{exhale}(t)}{FRC}\,dt \approx \frac{\sum_{i=1}^{n} TV(i)}{FRC} \qquad \text{Eq. [2.25]}$$

[3] Cet = end tidal concentration. End tidal concentration is referred to as the gas concentration at the end of an exhalation.

V_{exhale} is a function of the exhaled volume over time, $t=0$ is the start of the washout as the first expiration and the disconnection from the tracer gas (in the case of nitrogen washout, switching to inhalation of pure oxygen) and t_{end} is the last expiration (with a Cet_{end} = 1/40 of Cet_{ini} e.g. typically 0.2% for SF_6 washout and 78% for nitrogen washout). This can be approximated by the sum of tidal volumes (TV) during washout divided by the FRC. FRC is calculated from the same test as the dilution of the tracer gas over the same number of breaths:

$$FRC = \frac{\int_{t=0}^{t_{end}} C_{tracer}(t) \cdot Q(t) \cdot dt}{\Delta C(t_{end}, t=0)} = \frac{\sum_{t=0}^{t_{end}} C_{tracer}(t) \cdot Q(t) \cdot T}{Cet_{ini} - Cet_{end}} \qquad \text{Eq. [2.26]}$$

where C_{tracer} is the recorded tracer gas concentration, $Q(t)$ the flow, and T is the sampling rate of the device for the tracer gas and the flow (typically <50ms).

LCI in healthy volunteers ranges from 5.5 to 7.5 and is only weakly age dependent with slightly increasing LCI in older healthy volunteers [95]. Its sensitivity to early changes in disease has been proven in cystic fibrosis (CF) [95, 97, 98]. Another major advantage is that LCI is easy to understand and to calculate. LCI will be reported as a measure of VH for the clinical trials in Chapter 8.

2.6. Multiple breath washout models - modelling gas mixing

Since its establishment, it has always been of great interest to draw conclusion and models of regional changes in VH from MBW. The underlying model in common to all approaches to recover regional information is presented in the following section and is based on the work of Gomez [122].

Ventilation is a time dependent process that can be measured globally in gas volume turned over per breath or second e.g. using spirometry. Ventilation is a continuous process that allows wash-in of fresh air and washout of CO_2-enriched air. When recording MBW the gas composition of the lung during each exhalation is probed while a tracer gas is being washed out. MBW is sensitive to VH, meaning that changes in regional ventilation affecting parts of the lung are reflected in the course of the washout curve. As discussed before this manifests in metrics like the LCI [121], but it is desirable to quantify the information about changes of single lung regions that are coalesced in this global measurement. The underlying model to derive this information divides the lung into n compartments with different regional ventilation [85, 122]. This model assumes that all compartments are connected in parallel and that each compartment is separate and does not interact with neighbouring compartments. Gas leaving a compartment is washed out from the

lung. In addition it is assumed that each compartment is uniformly ventilated and no sub-compartmental ventilation differences are present. The compartmental model treats ventilation as a repetitive (same from breath-to-breath) and non-continuous periodical process that is probed at discrete (same) time points [85, 123]. To quantify compartmental properties, fractional ventilation is used throughout this work. Fractional ventilation r is defined as the ratio of fresh gas (V_f) entering a volume unit, to the total end-inspiratory size of the unit:

$$r = \frac{V_f}{V_f + V_r} \qquad \text{Eq. [2.27]}$$

with V_r being the residual or end-expiratory volume of the compartment. Figure 2.26 schematically shows the concept of fractional ventilation in two compartments with different ventilation. Fractional ventilation has no unit and is dimensionless [122]. Values of fractional ventilation range from 0 (=no fresh gas entering a unit) to 1 (=100% fresh gas in each breath) and can be used to describe the concept of ventilation heterogeneity (VH) in a quantitative manner (using the compartmental model by deriving e.g. standard deviation of whole-lung fractional ventilation histogram, see Chapter 8).

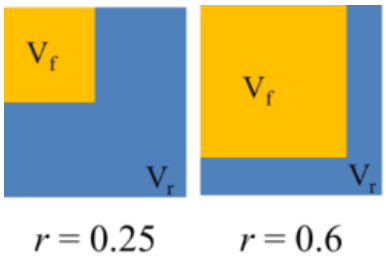

Figure 2.26: Schematic of fractional ventilation of two compartments with different lung ventilation.

Fractional ventilation can be directly converted into the specific ventilation parameter (SV). SV is defined as the ratio between the fresh gas entering the lung with each breath (V_f) over the expiratory volume of a voxel (V_r) and is also used in the literature [25, 122, 124-126]:

$$SV = \frac{V_f}{V_r} = \frac{r}{1-r} \qquad \text{Eq. [2.28]}$$

Tracer gas concentration measured during each exhalation of a MBW measurement at the mouth is the result of all compartments emptying at different rates from different positions of the lung. By measuring the exhaled volume over multiple breaths the properties of virtual compartments can possibly be recovered. With the compartmental model and this underlying idea, MBW recordings have been used to predict lung compartments (size and regional ventilation) reaching

from $n = 2$ compartments to a continuous spectrum of regional ventilation distribution [120, 125, 127, 128]. It should be noted that attributing these compartments to regional location in the lung is not possible as there is no unique solution. In the case of MBW-imaging developed in Chapter 5, the compartmental information of concentration decay is measured as the image intensity decay with each breath in every voxel, thus giving truly regional information of each compartment. In addition, quantitative values can be derived from signal changes gas does not need to be washed in to equilibrium before starting a wash-out – a prerequisite when sampling tracer gases during MBW at the mouth.

Chapter 3 Lung ventilation volumetry with same breath acquisition of hyperpolarised gas and proton MRI[4]

3.1. Introduction

Hyperpolarised gas (^{3}He and ^{129}Xe) single breath-hold lung ventilation weighted MRI has been shown to be sensitive to disease severity in chronic obstructive pulmonary disease [129-131], cystic fibrosis [51, 132, 133], asthma [134-137] and other obstructive lung diseases [138, 139] (see Figure 2.16). The technique can resolve regional impairment in lung ventilation caused by airway obstruction before changes are seen in spirometry [129, 140] and before structural alterations of lung disease are manifested on CT [141].

With ^{3}He lung ventilation weighted MRI, high spatial resolution gas spin density images, (referred to as ventilation images) can be produced covering the whole of the lungs at a single breath-hold. Initially defect size and count were used to derive a semi-quantitative parameter from functional images acquired using this technique [55, 142]. Nevertheless, this can result in intra observer differences and a defect count and classification according to size (e.g. small, medium, big) represents only a semi-quantitative method. When combined with spatially registered proton (^{1}H) images of the lungs, a commonly used quantitative metric can be derived, such as the percentage of lung ventilated or obstructed. This is calculated from the ratio of the ventilated lung volume from ^{3}He ventilation MRI to the total lung volume from the segmented ^{1}H lung MRI [129]. Percentage of lung volume ventilated (%VV) and its derivative, the volume of defects in percent(VDP) are quantitative measures of lung function, which have been shown to be sensitive to early obstructive changes in the lungs of smokers with normal spirometry [129] and in the assessment of lung ventilation changes in response to bronchodilator therapy [143].

[4] This chapter is based on an article published in NRM in Biomedicine: Lung ventilation volumetry with same breath acquisition of hyperpolarized gas and proton MRI. [1]FC Horn, [1,2]BA Tahir, [1]NJ Stewart, [1]GJ Collier, [1]G Norquay, [1]G Leung, [2]RH Ireland, [1]J Parra-Robles, [1]H Marshall and [1]JM Wild; NMR in Biomedicine; Volume 27, Issue 12, pages 1461–1467, December 2014;

1. Academic Radiology, Department of Cardiovascular Sciences, University of Sheffield, UK

2. Academic Unit of Clinical Oncology, University of Sheffield, UK

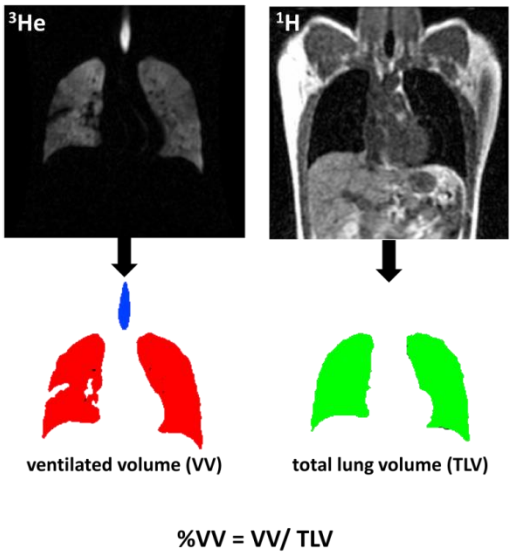

Figure 3.1: Calculation of percentage ventilated volume (%VV) is ratio of ventilated volume to total lung volume from masks of a ventilation scan and a proton scan. Example ^{3}He ventilation slice (left) and ^{1}H slice (right) from a healthy smoker.

The spatial signal variation in these ventilation-weighted images can also be analysed with other quantitative approaches such as cluster analysis or treatment response mapping (Chapter 4) [143, 144], which help quantify ventilation heterogeneity. Moreover, multi breath washout imaging [145] provides a more quantitative measure of ventilation without losses of the regional information (Chapter 5).

To date, all studies that have evaluated %VV and VDP with ^{3}He ventilation MRI, and indeed more recently with ^{129}Xe ventilation MRI [146], have acquired anatomical ^{1}H MRI images during a separate breath-hold from the hyperpolarised gas ventilation MRI images [129]. To match lung inflation levels between the separate ^{3}He and ^{1}H breath-holds, the same breathing manoeuvre can be used for both scans. However, any difference in lung inflation level between the separate breath-holds leads to an inherent error in the calculated %VV. Other studies have used interpolation algorithms to estimate the lung boundaries from the ^{3}He ventilation images alone [136, 147], which may not be robust in the presence of large peripheral ventilation defects, where the lung borders are difficult to delineate, and may therefore under or over estimate the total lung volume. The same day and short-term reproducibility of separate breath-hold and interpolation techniques for %VV calculation [53, 132] have been reported. However, no method currently uses ^{1}H MR images that are spatially and temporally registered to the hyperpolarised gas ventilation images for more accurate calculation of the total lung volume.

Methods to synchronously acquire hyperpolarised gas and ^{1}H images of the lungs have recently been demonstrated in our group [148, 149] allowing images of gas ventilation and lung anatomy to be acquired within the same breath-hold, thus, eliminating spatio-temporal mis-registration between scans. The benefits of the methods are yet to be tested quantitatively for %VV calculation. In this chapter a same breath hyperpolarised ^{3}He and ^{1}H 3D image acquisition protocol is used to demonstrate increased accuracy of %VV calculations when compared to the separate breath method. The method used is tested in a cohort of subjects scanned twice to assess reproducibility of %VV. In the same session proton images from a separate breath are acquired to assess reproducibility of separate breath methods and separate breath method facilitating image registration.

3.2. Materials and methods

3.2.1. Participant selection

13 volunteers were recruited for this study; no exclusion criteria based on either pulmonary function test results or smoking history were applied. The volunteers ranged in age from 24 to 70. Four volunteers were former smokers, one volunteer was a current smoker and eight volunteers were never smokers. No specific inclusion criteria were applied. The study was performed with National Research Ethics Committee and MHRA regulatory approval with informed consent from all volunteers.

3.2.2. Imaging protocol

Volunteers were positioned in a ^{3}He transmit-receive quadrature vest coil (Clinical MR Solutions, Brookfield, WI, USA). The ^{3}He coil was fitted with passive trap circuits to isolate the coil from the proton body coil and to block induced currents during its transmission at 63.6 MHz. For imaging a 1.5T MRI scanner (GE HDx, Milwaukee, WI, USA) was used. Figure 3.2 shows the timings of the imaging protocols used. In order to best replicate the lung inflation state during imaging [129], in breath 1, proton images were acquired after inhalation of 1L air from functional residual capacity (FRC). In breath 2, a 1L mix of hyperpolarised ^{3}He and N_2 was inhaled from FRC and ^{3}He images were acquired followed immediately by ^{1}H images in the same breath-hold. Breath 3 was a repeat of breath 2, with a maximum time interval of 10 minutes between the two ^{3}He breaths. Before breathing hyperpolarised ^{3}He, volunteers were trained in the breathing

manoeuvres using a test bag filled with air. They were instructed to exhale relaxed to functional residual capacity (FRC) before inhaling 1L of air. A test run was performed twice, outside the scanner to visually check the execution of instructions as well as the maneuver and once inside the scanner before the imaging protocol was carried out.

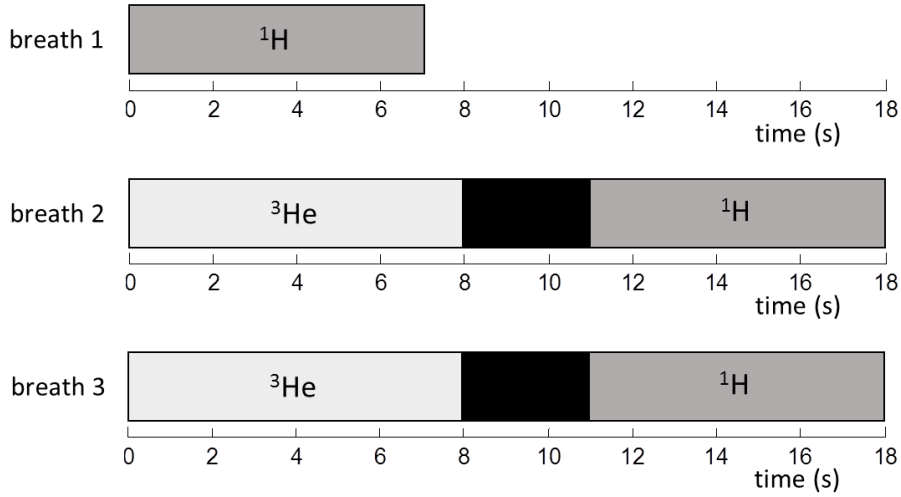

Figure 3.2: *Imaging protocol; ^{3}He image acquisition is shown in light grey, ^{1}H image acquisition is shown in dark grey and black indicates the delay time taken to switch the scanner from ^{3}He to ^{1}H acquisition.*

^{3}He ventilation MRI

Helium was polarised on site to approximately 25% using a rubidium spin exchange polariser (Section 2.4.2). Patients inhaled 150 ml ^{3}He mixed with 850 ml N_2 from a Tedlar bag (Jensen Inert Products, Coral Springs, Florida, USA) from functional residual capacity (FRC). An optimised 3D balanced steady state free precession sequence (bSSFP) [4] was used to acquire the static ventilation weighted images (parameters shown in Table 3.1) as discussed in Section 2.2.4.

Scan	*Echo time (ms)*	*Repetition time (ms)*	*Flip angle (°)*	*Bandwidth (kHz)*	*Field of view (cm) frequency x phase*	*Matrix size frequency x phase*	*Pixel size (mm) frequency x phase*	*Slice thickness (mm)*	Number of Slices
^{3}He ventilation (3D bSSFP)	0.6	1.9	10	167	40 x 32	100 x 80	4 x 4	5	42-54
^{1}H anatomical (3D SPGR)	0.6	1.4	5	167	40 x 40	100 x 100	4 x 4	5	42-54

Table 3.1: Scan parameters for the helium and proton acquisitions. The number of slices was adjusted for full lung coverage according to volunteer size but kept consistent for all scans of an individual volunteer. The size of voxels is kept constant for all volunteers and all scans.

^{1}H anatomical MRI

^{1}H images were acquired at the same voxel size and from the same volume as the ^{3}He ventilation images using the scanner quadrature transmit-receive body coil with a 3D spoiled gradient echo sequence (SPGR, parameters shown in Table 3.1). ^{1}H images were acquired in the same breath directly after both ^{3}He image acquisitions (breath 2 and breath 3, Figure 3.2) and also in a separate breath (breath 1, Figure 3.2). The SPGR sequence was used here instead of a 3D bSSFP to avoid banding-artefacts at the lung edges in the ^{1}H anatomical images.

3.2.3. Image analysis

All images were analysed using ScanIP (Simpleware Ltd, Exeter, UK). To calculate %VV for each volunteer the total lung volume was determined by segmenting the ^{1}H anatomical scans as well as ^{3}He functional images (Figure 3.3). Proton images were segmented in a semi-automated way by applying a 3D region growing algorithm based on thresholds. The thresholds were manually tuned and had to be changed individually for each dataset. Following this step, holes in the mask were filled automatically. Resulting masks were visually inspected and manual correction was applied wherever necessary. As a final step major airways were excluded from the mask up to the second generation. In a similar fashion ^{3}He ventilation images were segmented using the same threshold-based region growing method (Figure 3.3) and by setting thresholds manually and patient specific. Artifacts from cardiac motion, found in 3D SSFP images, and the signal from the major airways were manually excluded. To exclude any ^{3}He signal which fell outside of the lung volume as defined by the proton images and to prevent an unrealistic %VV > 100%, the masks from the ventilation images were multiplied by the proton masks produced in the previous step. This situation may arise for example if the lung inflation level in the ^{3}He images is greater than that in the ^{1}H images when acquiring images in separate breath-holds. Despite the use of same breath-hold imaging, partial volume effects may occur in voxels containing both ^{3}He signal and high ^{1}H signal e.g. close to the major blood vessels.

Ventilated volume was then divided by the total lung volume in order to calculate $\%VV_{single}$ and $\%VV_{separate}$ for each set of scans. The appropriate proton mask was applied to the ^{3}He masks in each case.

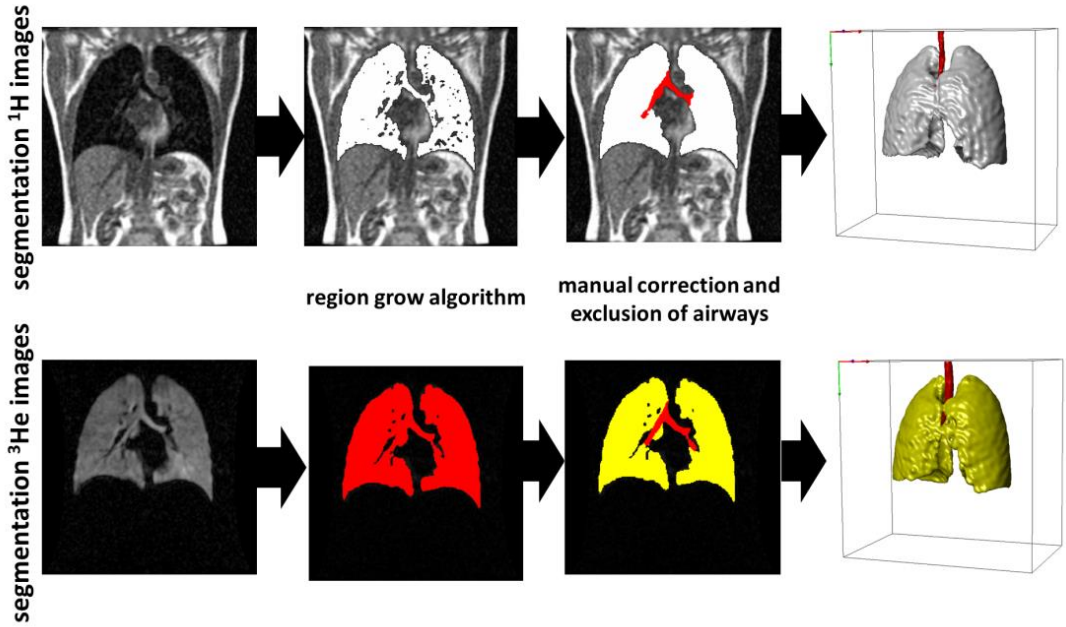

Figure 3.3: Image segmentation workflow for ^{1}H images and ^{3}He images.

Image registration

To assess the effect of image registration upon the efficacy of the separate breath method the proton images from breath 1 were registered to the ^{3}He images from breaths 2 and 3. In contrast to the rest of this thesis, where the Sheffield Image Registration Toolbox (SHIRT) was used, here image registration was performed using the ANTsRegistration tool incorporated as part of the Advanced Normalisation Tools [150]. SHIRT cannot be used with images deriving from different imaging modalities.

Registration was designed and conducted in collaboration with Bilal Tahir who has optimised ANTs for this purpose as part of his PhD project. The separate breath ^{1}H images (breath 1) were registered to the ^{3}He ventilation images (breaths 2 and 3). The mutual information similarity metric was used. A coarse pre-alignment rigid transform was applied to align the centres of the image datasets. The resulting transform was then input to a rigid transform stage allowing for rotations and translations only. An additional diffeomorphic transformation was also applied to the resulting transform of the rigid transform pipeline. The registered proton masks were used to calculate $\%VV_{sep\text{-}registered}$.

Dice overlap analysis

As an additional metric to compare single breath ^{3}He and ^{1}H acquisition, separate breath acquisition and registered separate breath acquisition, Dice similarity coefficients (DSC) were

calculated [151] to quantify the overlap between the segmented ^{3}He and ^{1}H masks for the three techniques at each time-point. DSC is a measure of spatial overlap which gives a value between 0 (no overlap) and 1 (complete overlap). The DSC of ^{3}He and ^{1}H segmentations was defined as follows:

$$DSC = \frac{\sum A \cap B}{\sum A \cup B} \qquad \text{Eq. [3.1]}$$

where, A was the ^{3}He mask and B was the ^{1}H mask. Dice coefficient is calculated as the ratio of the sum of all voxels mask A and B have in common to the sum of all voxels from mask A or B. Dice is commonly used to test how well image registration aligned two masks derived from registered images.

Statistical analysis

The calculated %VV values for each subject were represented on Bland-Altman plots for single and separate breath measurements. As a metric of reproducibility of %VV measurements, magnitude differences in %VV (time-point 1 minus time-point 2) were calculated for the single and separate breath methods. The magnitude differences in %VV returned by the single and separate breath methods were tested for significant difference using a Wilcoxon matched-pairs signed rank test.

To assess reliability and consistency between measurements of %VV1 and %VV2 for the different techniques, the following measures were calculated; 2-way random single measures intra-class correlation (ICC), coefficient of variation (CoV), standard error of measurement (SEM) and smallest detectable difference (SDD) [152]. In addition the Pearson's r and its corresponding P-value were calculated as a measure of correlation between repeated measures. In case of non-normally distributed data the Spearman's correlation was calculated instead.

To compare Dice overlap results, the mean DSC of time-points 1 and 2 was calculated for each technique for each volunteer. A Wilcoxon matched-pairs signed rank test was used to test for difference between the mean single breath acquisition DSC and the mean separate breath acquisition DSC, and difference between the mean single breath acquisition DSC and the mean registered separate breath acquisition DSC.

3.3. Results

Table 3.2 and Figure 3.4 show percentage ventilation values from the single breath technique, the separate breath technique and the registered separate breath technique. When measured with the single breath acquisition, 12 volunteers had %VV between 89% and 100% and 1 volunteer had a lower %VV (mean %VV single = 70%, ^{3}He image shown in Figure 3.5b). Using the separate-breath technique measured %VV values were spread over a larger range between 73% and 98% (Figure 3.4).

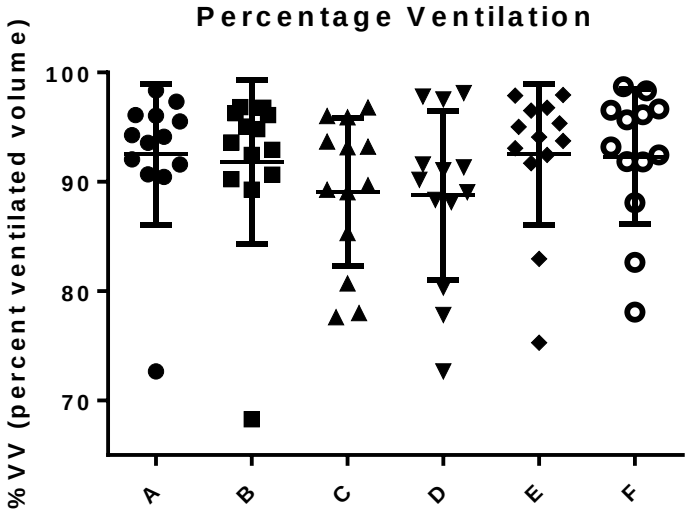

Figure 3.4: *Percentage ventilated volume values measured using:*

single breath technique	● (***A***) *%VV1 single breath from breath2*	■ (***B***) *%VV2 single breath from breath 3*
separate breath technique	▲ (*C*) *%VV1 separate breaths from breaths 1 and 2*	▼ (***D***) *%VV2 separate breaths from breaths 1 and 3*
registered separate breath technique	♦ (***E***) *%VV1 registered separate breaths from breaths 1 and 2*	○ (***F***) *%VV2 registered separate breaths from breaths 1 and 3*

Examples of the ^{3}He ventilation images acquired are shown in Figure 3.5. Figure 3.6 demonstrates how the use of separate breaths for the ^{3}He and ^{1}H images can introduce errors in the %VV calculation due to the different inhalation volumes. In this example the separate breath ^{1}H image (b) was acquired at a higher lung inflation level than the ^{3}He image (a) resulting in underestimation of %VV (c), whereas the ^{3}He and ^{1}H images acquired in the same breath (a, d) have the same lung inflation level allowing accurate calculation of %VV (e).

Figure 3.7 shows Bland-Altman plots of %VV measurements obtained by the three different techniques. The reproducibility of %VV measured with single breath acquisition (a) is greater than that measured with the conventional separate breath acquisition either without (b) or with registration (c).

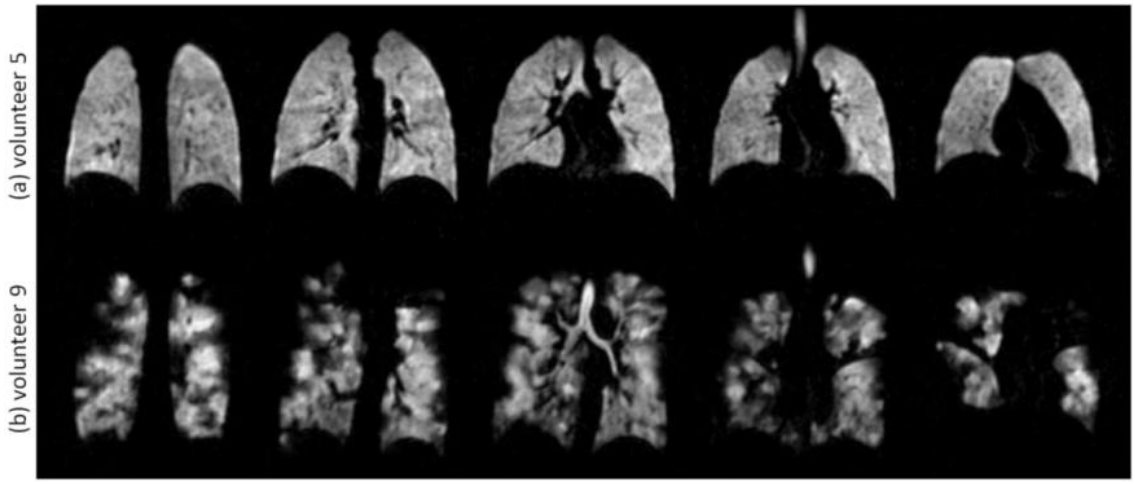

Figure 3.5: ^{3}He ventilation images of the volunteers with (a) the highest single breath %VV (mean %VV single = 97.59%) and (b) the lowest single breath %VV (mean %VV single = 70.47%).

Volunteer	%VV1 single (%) breath 2	%VV2 single (%) breath 3	%VV1 separate (%) breaths 1 & 2	%VV2 separate (%) breaths 1 & 3	%VV1 registered separate (%) breaths 1 & 2	%VV2 registered separate (%) breaths 1 & 3
1	94.12	92.93	77.98	91.59	95.29	82.62
2	93.56	92.47	89.05	77.81	92.46	88.09
3	91.59	94.83	85.32	91.06	91.69	95.67
4	96.06	96.11	95.89	97.79	97.88	98.70
5	98.34	96.83	96.01	97.53	96.76	96.53
6	96.10	93.61	93.68	89.04	95.02	92.46
7	94.26	95.04	80.70	80.33	93.75	91.86
8	90.67	90.23	93.16	91.33	94.08	93.18
9	72.65	68.29	77.62	72.66	82.95	78.08
10	97.34	96.78	89.29	90.19	96.51	96.65
11	95.52	96.28	96.81	98.13	97.94	98.32
12	90.46	90.64	93.23	88.16	95.36	96.14
13	92.06	89.29	89.68	88.34	93.08	91.83

Table 3.2: Percentage ventilated volume (%VV) measurements.

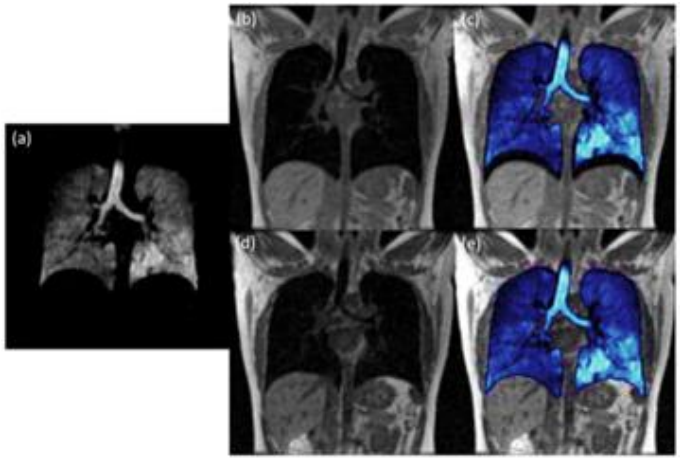

Figure 3.6: Example of lung inflation level differences between separate breaths, volunteer 1. (a) ^{3}He ventilation image, breath 2, (b) separate breath ^{1}H image, breath 1 and (c) shows (a) superimposed on (b). (d) Single breath ^{1}H image, breath 2 and (e) shows (a) superimposed on (d).

Single breath compared to separate breath

The mean of magnitude %VV differences between the two sets of measurements (± standard deviation) for the single breath technique was 1.49 ± 1.32% whilst the mean of magnitude %VV differences between the two sets of measurements for the separate breath technique was 4.19 ± 4.10%. A Wilcoxon matched-pairs signed rank test showed significant difference between the reproducibility of the same-breath and separate-breath acquisition strategies (P=0.01).

Single breath compared to registered separate breath

The mean of magnitude %VV differences between the two sets of measurements for the registered separate breath technique was 2.27 ± 2.23%. A Wilcoxon matched-pairs signed rank test found no significant difference between the reproducibility of the same breath and registered separate breath techniques (P=0.19). There was significant difference between the reproducibility calculated from separate breaths without registration and separate breaths with registration (P<0.01, Wilcoxon matched-pairs signed rank test). Registration improved the reproducibility of separate breath %VV measurement but the registered separate breath %VV still remained less reproducible than single breath %VV (Figure 3.7).

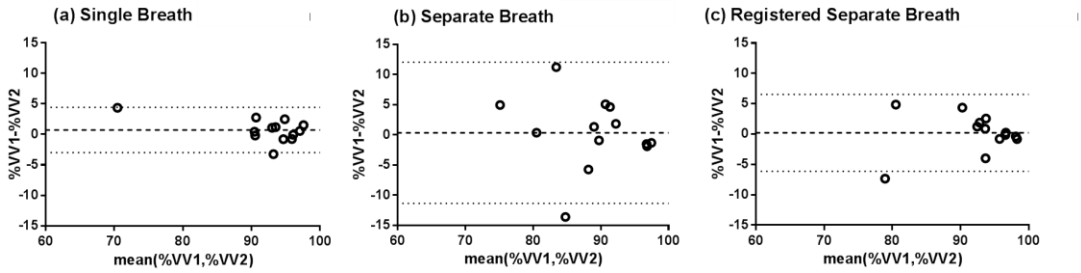

Figure 3.7: Bland-Altman plots of %VV measurement reproducibility for the three techniques; (a) single breath (mean difference = 0.7%, standard deviation = 1.9%), (b) separate breaths (mean difference = 0.3%, standard deviation = 6.0%) and (c) registered separate breaths (mean difference = 0.2%, standard deviation = 3.2%). The lines show mean difference and 95% confidence intervals.

%VV calculated from single breath image acquisition was found to be more reliable than %VV calculated from separate breath images, with or without registration, for all consistency measures. Measurement error quantified by SEM and SDD was smallest for single breath %VV and consistency between measures quantified by ICC, Pearson's r and CoV was greatest for single breath %VV. Dice overlap was greatest for the registered separate breath acquisition and smallest for the separate breath acquisition without registration (Table 3.4**Error! Reference source not found.**). There was significant difference in DSC between the same breath acquisition and separate breath acquisition ($P < 0.01$), and between the same breath acquisition and registered separate breath acquisition ($P < 0.01$).

Measure	Single Breath	Separate Breath	Registered Separate Breath
ICC (2,1)	0.961	0.679	0.877
r (P-Value)	0.857*	0.621	0.896*
CoV (%)	1.21	3.44	1.84
SEM (%)	1.34	4.23	2.29
SDD (%)	3.72	11.72	6.35

*Table 3.3:Intra-class correlation (ICC(2,1)), Spearman's r (with corresponding P-value), coefficient of variation (CoV), standard error of measurement (SEM) and smallest detectable difference (SDD) for the three techniques.*Spearman's r*

	Single Breath	Separate Breath	Registered Separate Breath
mean Dice overlap	0.9076	0.8690	0.9152
std Dice overlap	0.0325	0.0488	0.0433

Table 3.4: Mean and standard deviation (std) Dice overlap after taking the mean of time-point 1 and time-point 2 for each technique.

3.4. Discussion

Repeated measurements of lung function within a short time period would be expected to be similar. The differences between repeated separate breath %VV measurements are thought to be primarily due to different lung inflation levels in the ^{3}He and ^{1}H images acquired in separate breaths as clearly visualised in Figure 3.6. Acquisition of the ^{3}He and ^{1}H images during the same breath provides inherent spatial and temporal registration, allowing accurate calculation of %VV. The remaining difference between repeated single breath %VV measurements could be primarily attributed to genuine variability in ^{3}He distribution between the two breaths due to physiological factors such as lung ventilation heterogeneity from any underlying airways obstruction. Another source of variability when comparing repeated same-breath %VV values, particularly in a patient population, could be on account of different lung volumes at the two time-points due to partially obstructed airways opening at higher lung volumes. Nevertheless, this effect is minimised when both image-sets were acquired after the same breathing manoeuvre at FRC+1L.

The reproducibility of %VV measurement was found to be significantly greater using same breath acquisition than with separate breath acquisition. Registration of the separate breath proton images to the helium images significantly improved the reproducibility of the separate breath technique, and there was no significant difference between registered separate breath and single breath reproducibility. Image registration in the lungs is challenging, particularly when using MR images like these, which lack distinct internal landmarks. Whilst the lung edges can be warped to one another, the accuracy of registration across the whole lungs remains questionable. There are some marked discrepancies in mean %VV when measured with single breath and registered separate breath acquisition (Figure 3.7). For example, mean %VV single breath = 94% and mean %VV registered separate breath = 89% for volunteer 1, and mean %VV single breath = 70% and mean %VV registered separate breath = 81% for volunteer 9. Considering the nature of the two techniques it is likely that registration is introducing error into the %VV measurement in these cases, although it is difficult to accurately establish this given that there is no ‘gold standard’ %VV value to compare with. It also can be expected that errors resulting from registration will increase with decreasing %VV values as found in patients with obstructive lung diseases as peripheral ventilation defects make the bounds of the lung less well defined. Same breath acquisition provided increased reproducibility (as tested with Bland-Altman analysis), increased consistency (ICC and CoV) and reduced measurement error (SEM and SDD) when compared to separate breath acquisition either with or without registration. Similar comparisons using the

separate breath technique are reported in two publications. Investigating 24 COPD patients Mathew et al. [53] claimed to find an ICC of 0.97 calculating the ventilation defect volume (VDV=TLV-VV), when comparing images acquired within about 10min intervals. This shows a very high reproducibility of VDV. Kirby et al. performed a similar analysis on a CF population [132]. The gap between the two imaging sessions was 7 days, which was considerably longer than in the presented study. A Bland-Altman analysis was done on ventilated defect percentage (VDP=100%-%VV) from this population and a mean difference of -3% with a standard deviation of 4% was found. They also reported a high correlation between repeated scans with a Spearman's r = 0.94. The high correlation is not a surprise, since the standard deviation found from the Bland-Altman analysis was relatively small and the pulmonary function tests of this patient cohort were spread out over a wide range. The high mean difference of -3% might be explained with ventilation changes between scans. The standard deviation of the Bland-Altman analysis is comparable to what we found (SD = 3.2%, separate breath registered, Figure 3.7 (c)) and the much lower mean difference (MD = 0.3%) can be explained with the smaller gap between scans (5 min versus 7 days). The slightly lower correlation (r = 0.90) in this study compared to Kirby et al. can be explained by a much smaller range of values of %VV.

Dice overlap between the segmented ^{3}He and ^{1}H masks was significantly greater for single breath acquisition than for un-registered separate breath acquisition as would be expected. The Dice overlap of the registered separate breath technique was significantly greater than that of single breath acquisition. This is likely to be due to the fact that the diffeomorphic registration used is driven by a cost-function, which sought to maximise a metric similar to DSC. The different contrasts of the source and target images, the lack of internal structures visible in the lungs in the SPGR ^{1}H images and partial-volume effects make registration of ^{1}H to ^{3}He images complicated. Therefore it is realistic to assume that registration will introduce some level of error into %VV calculation, even in this healthy population.

Image segmentation of the ^{3}He ventilation images in this healthy volunteer population with an average SNR of 33 was checked visually and masks were adjusted manually to optimise segmentation. Automated segmentation eliminates inter- and intra-observer variability, nevertheless, in patient data, semi-automated segmentation was shown to be highly reproducible and more reliable than manual methods [153]. To date no reliable use of an automated algorithm for segmenting ventilation images has been found in the literature. Simple methods using noise level [52] are highly SNR dependent, more sophisticated segmentation using a region growing algorithm has been demonstrated [136]. A detailed comparison of those methods with manual segmentation is still a gap in the literature.

Overall there are still limitations of single breath %VV measurement. Although single breath acquisition removes breath to breath inhalation volume discrepancy, factors such as cardiac motion and any gradual or sudden diaphragm movement during the breath-hold are not mitigated. In a few cases a small movement of the diaphragm occurred between the ^{3}He and ^{1}H images in the same breath-hold. In a patient population it is more likely that some patients would not be able to complete the 18s breath-hold. Further reduction of the single breath-hold duration will help to mitigate this problem. Further work is aimed at reducing the scanner-reset time between sequences on the system used (3s), which would then reduce the overall breath-hold time. In previous work at 3T on another system this delay was eliminated altogether by acquiring the ^{1}H and ^{3}He data in an interleaved fashion from k-space view to view [148]. The interleaved sampling technique is not used here since a non-successful breath-hold (especially in the case of severe patients) would result in image quality losses of both, the ventilation and anatomical scan. With the proposed method, the important information from the ventilation images is more likely to be acquired successfully. In addition the use of faster image acquisition acceleration methods such as parallel imaging and compressed sensing [154, 155] could be used to substantially reduce the breath-hold duration for synchronous ^{3}He and ^{1}H acquisition.

3.5. Conclusions

In conclusion, hyperpolarised ^{3}He ventilation and ^{1}H anatomical MRI acquisition within a single breath-hold was shown to provide spatially and temporally registered images. These coregistered same breath images increased the reproducibility of percentage lung ventilation calculation. The single breath method is more consistent in measuring percentage ventilated lung volume and minimises errors from lung inflation volume differences. The increased reliability of the technique when compared to the separate breath approach will reduce statistical noise and should enable subsequent studies that use this lung imaging metric of ventilation to evaluate intervention and exacerbations to reach an appropriate power with a smaller number of participants. In addition the image processing workflow can be further automated in major parts with the use of automated image segmentation (e.g. using edge detection).

The major disadvantage of %VV, independent of how it is obtained, remains a complete loss of all regional ventilation intensity information by converting images into binary masks of ventilated/non-ventilated. Also %VV has been shown to be a sensitive measure to early changes in disease, valuable information from images is lost. Exploiting the fact that image intensity is proportional to gas concentration could give further insight into inhomogeneous gas distribution as a measure of ventilation heterogeneity (VH). The following chapter presents a new approach

using ventilation weighted imaging to maximise the regional information to detect regional changes in ventilation as response to treatment.

Chapter 4 A method for quantitative mapping of lung ventilation in response to treatment using hyperpolarised ^{3}He MRI demonstrated in asthma patients[5]

4.1. Introduction

Functional imaging using single-breath hyperpolarised gas ventilation MRI is able to measure ventilation as regional gas distribution. Image intensity in ventilation weighted images acquired in a single breath is proportional to gas concentration in that voxel. Hyperpolarised gas ventilation MR-imaging has been shown to be a sensitive measure of ventilation heterogeneity in asthma [142, 156-159]. In addition, simple metrics such as percentage ventilated volume (%VV, Chapter 3) and percentage ventilation defect volume can be derived from these images, which have been shown to correlate with spirometry in asthma [132, 134, 160]. These metrics which express the percentage of the lungs ventilated, whilst commonly used, are limited by the binary classification of lungs as non-ventilated versus ventilated as result of image segmentation process. Furthermore, despite being derived from regionally specific imaging data, these numbers represent coalesced metrics from the whole lung. Thus, there is scope and a need to derive better quantitative metrics from these exquisite, sensitive and high spatial resolution images of regional lung function that better utilise the quantitative data from all voxels. This is particularly the case when we are interested in which parts of the lung respond to therapy.

Methods to quantify gas distribution based on ventilation image intensity have been proposed before. Clustering has been used to subdivide image intensities into different shades of ventilation intensity [153], and a continuous approach to normalise images using gas volumes and mean image intensities has been used as an outcome measure to assess response to metacholine challenge in asthma patients [158]. However, a direct comparison of images from multiple time-points has not been performed with either of these techniques.

In this work a technique to quantitatively map treatment response of the lungs using hyperpolarised ^{3}He ventilation images was developed and evaluated in an asthma cohort pre and post bronchodilator application. The motivation was to develop an algorithm sensitive to regional

[5] Acknowledgements:
I would like to acknowledge Professor David Barber for his help with the image registration and Bilal Tahir for great advice on the same topic. Ventilated volume calculation from ventilation images were performed by John C. Kenwrothy.

change in ventilation which isanalogous to brain activation mapping methods used in fMRI of BOLD. This approach is quantitative and regionally specific whilst being visually accessible.

4.2. Materials and methods

4.2.1. Patient recruitment

22 patients diagnosed with moderate-to-severe asthma (uncontrolled on their therapy), were recruited for this study. Patients were classified according to the GINA (Global Initiative for Asthma) step 2-5. 12 female and 10 male patients with a mean age of 51±12years (mean ± standard deviation) and FEV1 of 71±27% predicted were tested for response to bronchodilator with pulmonary function tests and hyperpolarised gas functional lung MR imaging after withholding the use of short acting β2-agonists for at least 6 hours. The patients' own bronchodilator was applied orally through inhalation during the visit to the MRI unit. All subjects recruited for the treatment response mapping were able to hold their breath for a total of 18 seconds during image acquisition. The study was performed with National Research Ethics Committee approval and with informed consent from all volunteers. Detailed patient demographics and results from pulmonary function tests are shown in Table 4.1.

Patient	Age	GINA	Sex	FEV1 % predicted Visit 1*	FEV1% predicted Visit 2*	FVC (L)	RV (L)	TLC (L)
1	49	4	F	41	-	2.14	2.57	4.68
2	54	5	F	33	33	1.47	3.28	5.53
3	63	4	F	70	-	2.13	1.73	3.87
4	53	5	F	74	-	2.65	2.37	4.95
5	49	-	M	80	-	5.30	-	8.51
6	53	5	F	61	-	2.88	3.50	6.30
7	41	4	F	54	-	2.00	1.53	3.86
8	65	4	M	72	-	3.40	3.21	6.91
9	41	5	M	97	-	5.20	2.19	7.10
10	59	4	F	95	89	3.10	2.01	5.06
11	45	4	F	114	125	4.85	2.70	7.89
12	62	2	M	44	36	3.85	4.16	8.98
13	45	5	M	72	104	4.53	2.73	7.39
14	73	4	M	41	-	2.27	5.71	8.20
15	66	4	M	27	-	2.96	4.91	8.05
16	36	4	M	100	86	4.58	2.37	7.31
17	60	4	F	122	-	3.10	2.43	5.74
18	44	4	F	78	-	3.31	2.10	5.22
19	52	4	F	101	100	2.85	1.47	4.26
20	21	4	F	84	-	4.15	1.22	5.50
21	34	4	M	51	-	3.75	2.62	6.79
22	60	3	M	47	-	3.05	4.33	7.21
Average(±Standard deviation)	**51(12)**	**4.1(0.7)**	**-**	**71(26)**	**82(32)**	**3.34(1.05)**	**2.82(1.14)**	**6.20(1.53)**

*Table 4.1: Overview patients. *measured at baseline before application of the bronchodilator*

4.2.2. MRI acquisition

All patients were scanned at three time points. Two images were acquired before application of a bronchodilator (baseline scans) and once more after application of the bronchodilator (post-BD scan). The scan protocol timing is schematically shown in Figure 4.1A: the baseline scans were both acquired within a time frame of five minutes to assess short time scale baseline physiological variability in lung ventilation, and the scan following bronchodilator inhalation was acquired 20 minutes after administration of the drug. Each MRI scan consisted of functional images (^{3}He ventilation) and structural images (^{1}H anatomy) acquired during a single breath of <18 seconds. In addition to MRI scans, PFTs were performed during a separate visit temporally close (±3 days) to the imaging appointments.

Six patients returned after 12 weeks for a repetition of the MRI scans as a means of assessment of long term baseline variability; they were imaged with the same protocol as during their first visit (dropping only one of the baseline scans).

Images were acquired after inhalation of 1 litre of gas (350 ml ^{3}He mixed with 650 ml N_2) from functional residual capacity. Patients were trained in the breathing manoeuvre outside the MR scanner before the each imaging session and once inside the MRI scanner before administration of the hyperpolarised ^{3}He. Examples of corresponding MR-images from a subject are depicted in Figure 4.1B.

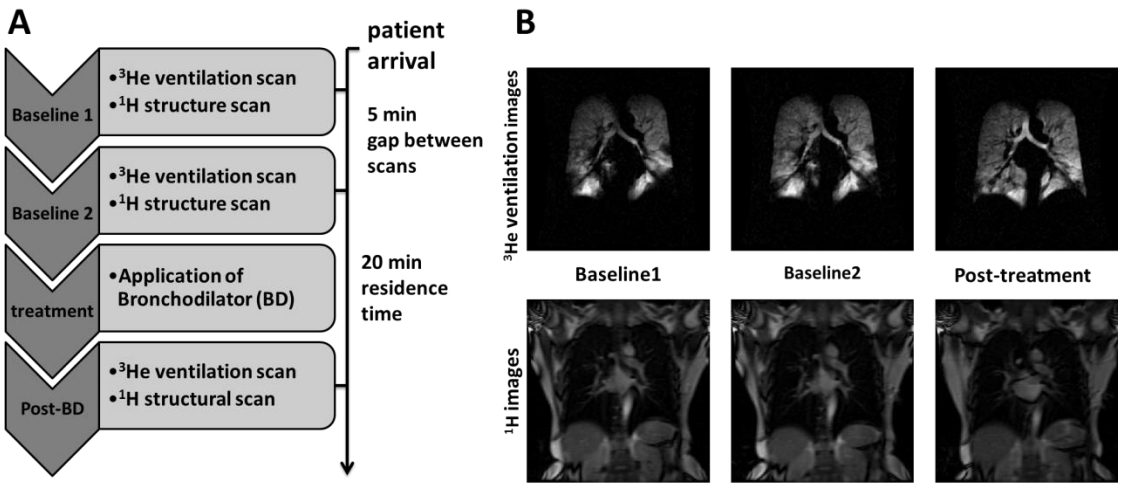

*Figure 4.1: (**A**) Imaging protocol, including the treatment application. (**B**) Corresponding example images ^{1}H and ^{3}He images from each time point.*

Patients were imaged using a whole-body clinical 1.5 T MRI scanner (GE HDx, Milwaukee, WI, USA) with a quadrature transmit-receive vest coil and the systems pquadrature transmit-receive body coil for proton imaging.

^{3}He Ventilation MRI

Helium was polarised on site to approximately 25% using a rubidium spin exchange polariser (GE Healthcare, Amersham, UK). Patients inhaled 350 ml ^{3}He mixed with 650 ml N_2 from a Tedlar bag (Jensen Inert Products, Coral Springs, Florida, USA) from functional residual capacity (FRC) as described earlier. A multi-slice 2D spoiled gradient echo sequence was adjusted to the patients' thoracic size with a field of view between 38 and 42 cm and 20-24 coronal slices of 10mm thickness. Static ventilation weighted images were acquired with a fixed imaging matrix of 128x102 resulting in a resolution of about 3x3x10mm. The echo time (TE) was set to 1.1ms with a repetition time (TR) of 3.6 ms using a flip angle of 8° and 62.5 kHz receiver bandwidth.

^{1}H anatomical MRI

During the same breath-hold ^{1}H images were acquired from the same volume as the ^{3}He ventilation images with a multi-slice 2D balanced steady state free precession sequence with a lower resolution matrix (128x64) to reduce the length of the breath-hold. The echo time was 0.7ms with a repetition time of 2.4ms using a flip angle of 50° and a receiver bandwidth of 167 kHz. Note that the advanced same breath 3D ventilation and anatomical imaging sequences used in Chapter 3 were not used in this study due to the fact that the asthma imaging protocol was defined for this study before that acquisition method had been evaluated.

4.2.3. Image analysis

Before quantitative treatment response maps could be calculated from the ventilation weighted images, three intermediate image processing steps were first necessary:

(i) Image registration

Image registration was performed to compensate for patient movement between acquisitions made during separate breaths and after repositioning. Despite training in the breathing manoeuver some patients struggled to reproduce their breath-hold precisely. Image registration was then used to correct for volume changes between images performed at different time points. Since the chosen treatment can change gas distribution and signal intensity related to ventilation in the lung considerably, the corresponding ^{3}He ventilation images can show substantial regional changes in intensity and morphology pre and post bronchodilator treatment. This makes registration of ventilation images before and after treatment difficult. To avoid the influence of morphologic changes in ventilation images on the deformation and translation of the registration process, the

temporally co-registered same breath proton images were used to facilitate registration. Since proton images were acquired in the same breath-hold as ventilation images (Figure 4.1B), the deformation matrix obtained from the proton anatomical image registration was applied to the ventilation images to spatially match acquisitions from different time-points. The registration algorithm used is part of a Matlab plugin called ShIRT (Sheffield image registration Toolbox) and described in [161] in greater detail (compare also Section 5.2.8.

(ii) Image segmentation

Semi-automated image segmentation was performed to segment signal from ^{3}He in ventilated lung voxels from the background using ScanIP (Simpleware Ltd., Exeter, UK) as presented in Section 3.2.3. A threshold-based region growing algorithm was used, followed by visual inspection of the result and an adjustment of the threshold if necessary. In a second step the major airways were manually excluded from the images. The results of segmenting an example slice are shown in Figure 4.2.

Figure 4.2: Showing the results of a segmentation and extraction of the major airways until generation 2/3 depending on visibility of the airways.

(iii) Normalisation of signal intensity

In order to compare ventilation images acquired at different time points normalisation is necessary. Normalisation was performed in two separate steps:

In a first step images are normalised to correct for variability in number of ^{3}He atoms dispensed (inhaled gas) and their polarization. This approach is based on Tzeng et al. [158]:

$$I'(\vec{r}) = \frac{I(\vec{r})}{\sum_r I(\vec{r})} \cdot \frac{V_{bag}}{V_{voxel}} \qquad \text{Eq. [4.1]}$$

$I'(\vec{r})$ is the normalised image intensity with $\vec{r}$ =(x,y,z). V_{bag} is the total amount of gas inhaled, which was in this study 1l in all cases and V_{voxel} is the voxel volume. The accumulated image

intensity $\sum_r I(\vec{r})$ is a factor independent of inhalation state (neglecting an finite detection threshold) of the lung and solely depends on amount of gas inhaled and the polarization thereof. The ratio V_{bag}/V_{voxel} is intra-patient constant and is a factor that allows the conversion into a volume fraction (not to be confused with fractional ventilation *r* in Chapter 5):

$$I'(\vec{r}) = \frac{I(\vec{r})}{V_{voxel}} \cdot V_{gas} \qquad \text{Eq. [4.2]}$$

With V_{gas} being the gas volume per unit intensity, $I'(\vec{r})$ is the approximate volume fraction of a voxel filled with the inhaled gas mix. The results of this normalisation are shown in Figure 4.3D.

In a second step of the normalization process the dilution of the inhaled gas dose due to variations in total lung volume between breaths is then compensated for. Each voxel is multiplied with the ventilated lung volume of the corresponding image (V_{lung}) divided by the lung volume after application of the bronchodilator (V_{lungBD}), which leaves $I''(\vec{r})$ (Figure 4.3E):

$$I''(\vec{r}) = I'(\vec{r}) \cdot \frac{V_{lung}}{V_{lungBD}} \qquad \text{Eq. [4.3]}$$

Baseline variability

Before bronchodilator treatment, two images were acquired in order to derive baseline variance images to distinguish the joint effects of the underlying variability in the experimental method and breath-to-breath physiological variability in regional lung function at baseline, from physiological changes in gas distribution directly resulting from the treatment response.
Three separate methods to derive baseline variability from the two pre-treatment images were investigated:

(1) Regional baseline variability

The mean difference between two pre-treatment acquisitions $\sigma(\vec{r})$ was used to assess regional variability based on the normalised images with $\vec{r}$ =(*x*,*y*,*z*):

$$\sigma(\vec{r}) = \left| I''_{baseline\,1}(\vec{r}) - I''_{baseline\,2}(\vec{r}) \right| \qquad \text{Eq. [4.4]}$$

(2) Regional baseline variability (nearest neighbour smoothing)

In an effort to make the calculated baseline variability less sensitive to random error in the images (noise and the effect of imperfect pixel-pixel registration), information from the neighbouring surrounding voxels was included. To compensate for non-isotropic voxels with approximately 3 times higher resolution in the imaging-plane than in the slice-direction (slice thickness fixed Δz

= 10mm) images were filtered in-plane with a [3 3] pixel kernel. The convolution matrix took surrounding pixels equally into account (mean-filter). After filtering images, regional variability was calculated as Eq. [4.4].

(3) Global mean difference

The baseline variability can also be defined as a global value for the whole lung. Regional baseline variability was calculated as per Eq. [4.4] then an average value of all non-zero voxels is calculated to obtain the mean global baseline variability, $\overline{\sigma}$:

$$\overline{\sigma} = \overline{\left| I''_{baseline1}(\vec{r}) - I''_{baseline2}(\vec{r}) \right|} \qquad \text{Eq. [4.5]}$$

In the case of the subgroup that came on two occasions 12 weeks apart, the baseline variability acquired during Visit 1 was used for both visits, since only a single pre-treatment image was acquired during Visit 2.

For subsequent calculation of treatment response maps method (2) was used throughout. Justification for this choice is discussed in the discussion section.

Treatment response

Having calculated the threshold for activation of treatment response for each voxel, the magnitude of the treatment response was then calculated from the difference between ventilated volume fraction before and after treatment over the total volume fraction in both images:

$$\Delta I(\vec{r}) = I''_{postBD}(\vec{r}) - I''_{mean\_basline}(\vec{r}) \qquad \text{Eq. [4.6]}$$

where $\Delta I(\vec{r})$ represents ventilation differences due to treatment. This subtraction to quantitatively compare the two images relies on the imaging parameters and hardware being the same and the subject being in a similar position in the RF coil. Each voxel of the calculated $\Delta I(\vec{r})$ map was then compared for 'activation' against the threshold set by the baseline variability $\sigma(\vec{r})$. Since $\sigma(\vec{r})$ was defined as the absolute difference between the two normalised baseline images it is used as a threshold for a positive or negative response effect of the difference of $\Delta I(\vec{r})$ before and after treatment. For voxels where this absolute difference was smaller than the absolute threshold $\sigma(\vec{r})$, treatment response was set to zero:

$$TR(\vec{r}) = 100\% \cdot \begin{cases} 0 \ if, & |\sigma(\vec{r})| > |\Delta I(\vec{r})| \\ \Delta I(\vec{r}) \ if, & |\sigma(\vec{r})| < |\Delta I(\vec{r})| \end{cases} \qquad \text{Eq. [4.7]}$$

The final result is the TR (treatment response) expressed in percent change. An example treatment response map from a single imaging slice is shown in Figure 4.3G (bottom). The black background represents the intersection of masks from baseline and post-treatment scans (see bottom Figure 4.3F). Treatment response is measured in terms of difference between normalized image signals $I''(\vec{r})$ before and after treatment, maps show increased ventilation $TR(\vec{r})>0$ in green and decreased ventilation in red $TR(\vec{r})<0$. Since $I''(\vec{r})$ is the approximate fraction of a voxel filled with gas (after gas volume and density normalization) changes are expressed in percent. Figure 4.3 shows a graphical overview of all image processing workflow steps.

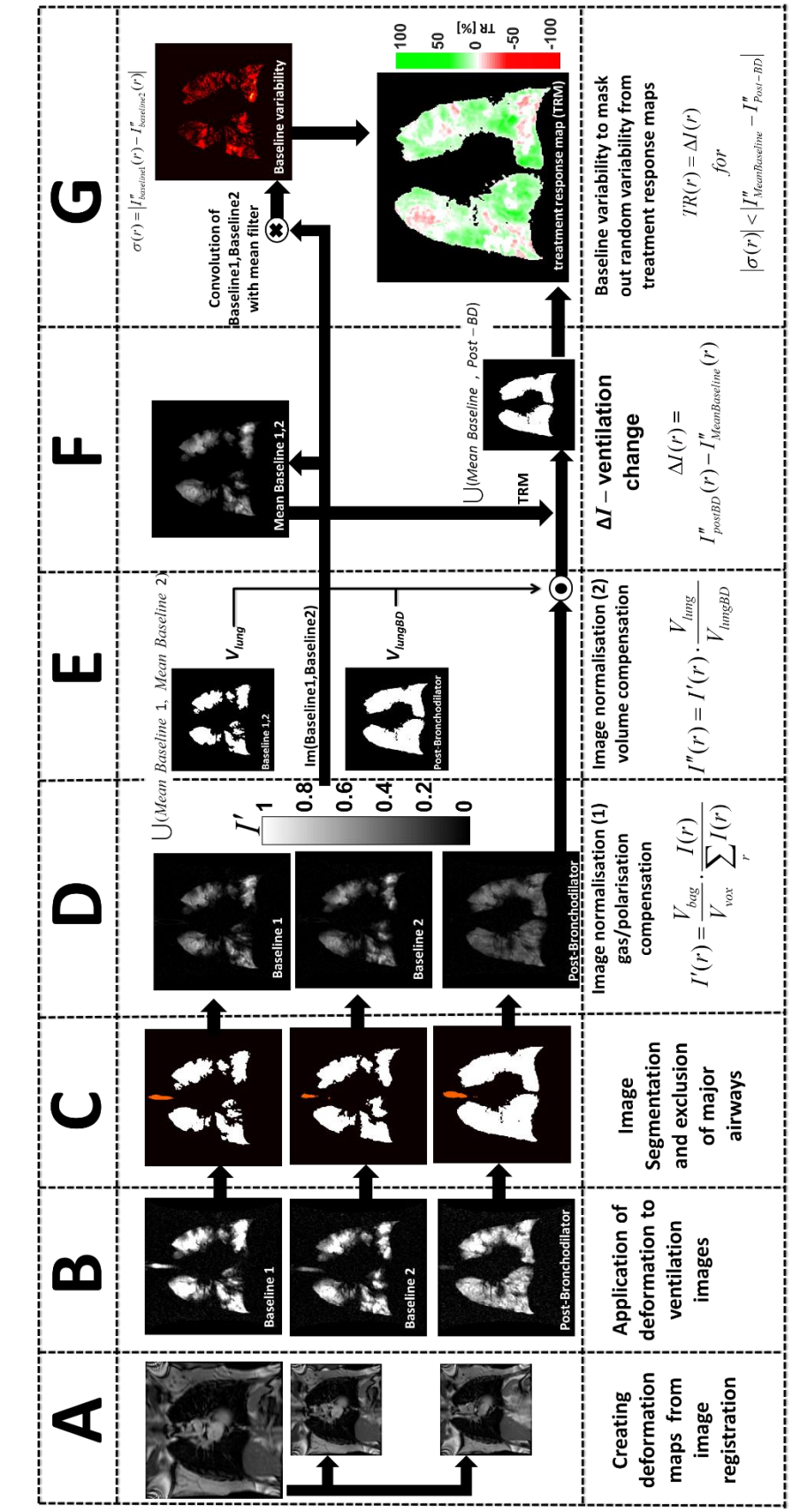

Figure 4.3: Different steps to calculated treatment response maps from ventilation weighted images.

Analysis

To compare lung ventilation before and after treatment, the positive response and negative response were assessed. Physiologically understandable values representinge ventilation changes were derived by integrating the fractional changes (%TR) and multiplying them by the voxel volume to obtain approximate gas volume newly entering a voxel or vanishing thereof (Figure 4.4). The effect was integrated over the whole lung for negative response resulting in accumulated volume decrease in regions of signal loss and positive changes as volume increase where signal is gained. The difference between total lung volume decrease and increase was tested for significance using Wilcoxon matched-pairs single-tailed signed rank test.

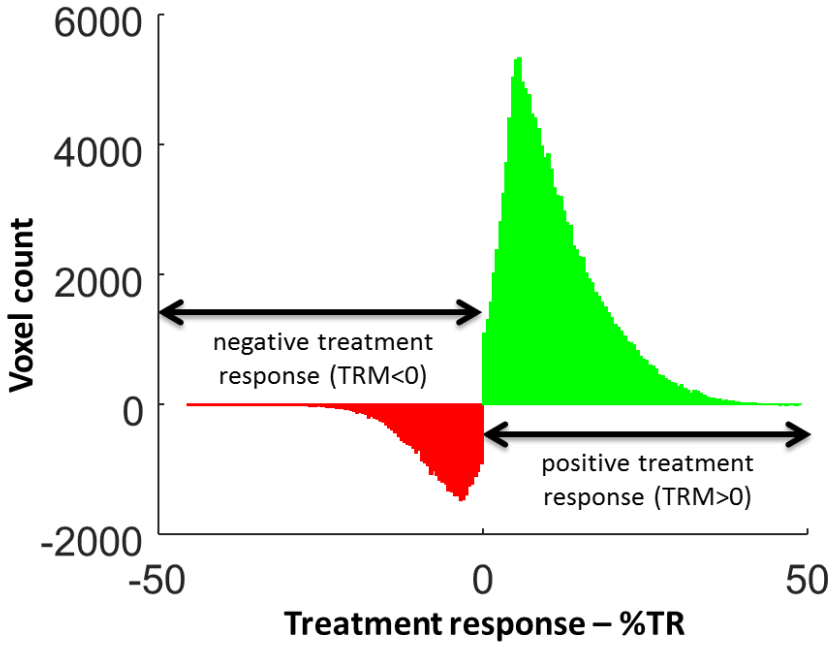

*Figure 4.4: Histogram of a treatment response map of relative changes of patient 2. Negative values denote reduced ventilation (**red**) and positive values represent increased ventilation (**green**) reaching a lung unit. In this example the positive response was reflected by an increase of 351ml over the whole lung compared to a total of 54ml decrease in ventilation. Therefore the net-volume change from the histogram was quantified to a positive 298ml. Corresponding treatment response maps of this patient are shown in Figure 4.6.*

Percentage ventilated volume

In addition to the treatment response map analysis, the conventional percentage ventilated volume (%VV) was calculated using the same co-registered ^{3}He and ^{1}H MRI datasets. This was done as

described. Ventilated lung volume was obtained from binary segmentation of ventilation images using a manual threshold. The volume of the lung cavity was segmented from ^{1}H images using a seeded region growing algorithm. All masks were visual inspected and, if necessary, manual corrected. The ventilated volume was calculated as the ratio of the volume of the mask from ^{3}He images to ^{1}H images as shown in Chapter 3.

Statistics

Difference between measurements made pre and post bronchodilator was tested for using a Wilcoxon test, since all normality tests were negative. To test response to bronchodilator, a one-tailed test was chosen since bronchodilator application is expected to have a positive effect on gas distribution in the lung. For all other tests a two-tailed test was performed, since no directional changes were suspected. To test %VV before and after treatment for significant changes a Wilcoxon matched-pairs signed rank test was used. $P = 0.05$ was chosen as significance level.

4.3. Results

4.3.1. Baseline variability

Baseline variability was assessed to evaluate short-term changes in gas distribution in the lung using two ventilation images acquired before bronchodilator inhalation. To decide how to best calculate thresholds of baseline variability based on two images the proposed methods (1), (2) and (3) from Section 4.2.3 were compared in four subjects. Treatment response maps were produced with the three different methods. To visualise the effects of the different baseline variability calculation methods, the distribution of voxels excluded values from the treatment response maps are plotted in Figure 4.5, with frequency in the y-direction and excluded TR-values in the x-direction.

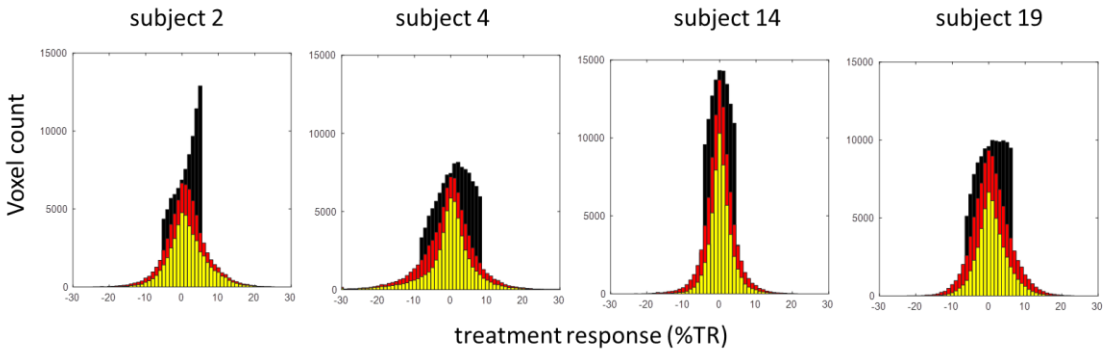

Figure 4.5: Histograms show distributions of excluded TR values using different methods to calculate the baseline-variability thresholds:

*Method 1: (**red**) – regional threshold as mean difference between baseline 1 & baseline 2*
*Method 2: (**yellow**) – regional baseline variability (nearest neighbour method)*
*Method 3: (**black**) – global threshold ;*

Method (3) is based on a cut-off threshold and does not take regional variability of ventilation into account but instead non-selectively excludes values. Both methods (1) and (2) allow for a regionally sensitive cut-off and approximately follow a Gaussian distribution (Figure 4.5). In comparison to method (1), method (2) aims to reduce the effects of noise by weighting the prescribed baseline variability for a given voxel with weightings from the nearest neighbour voxels. Method (2) was thus chosen as the number of voxels lost when masking treatment response with baseline variability was minimized (see Figure 4.6). A single slice example of a baseline variability map is shown in Figure 4.3G. The image shows regional hot-spots where more variability between the two images was observed.

4.3.2. Treatment response mapping

Treatment response mapping was successfully performed in 20 patients. An example dataset from patient 2 is shown in Figure 4.6, with treatment response maps and the corresponding ^{3}He MR images. Green areas corresponding to an increase of ventilation (TR as change of ventilated fraction) dominate the treatment response map. In this case, increase of gas volume was quantified as 351ml in total after treatment (green voxels) compared to a decrease of 54ml (red voxels). This results in a net-area of 297ml from the histogram in Figure 4.4.

Figure 4.7 shows the group treatment response to bronchodilator from all 20 patients. Changes in ventilation were measured as increased and decreased volume from integration of whole lung histograms. Positive response over the cohort was found to be significantly greater than negative response using a one-tailed Wilcoxon test ($P<0.001$). Accumulated volume increase was found

to be 210±68ml in comparison to a negative response of 95±31ml as graphically shown in Figure 4.7 in this cohort. The same test was used to test differences in percentage ventilated volume (%VV), which also showed significant increase (P<0.001) after bronchodilator application. FEV1 increased significantly (P<0.001) in response to bronchodilator application as well as FVC (P<0001). %VV was found to be 86±11% on average before treatment and elevates to 90±9% after treatment. FEV1 was found to change from an average of 71±27% predicted to 81±28% predicted.

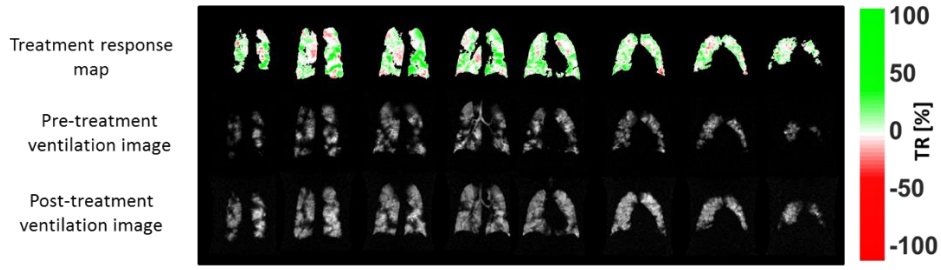

Figure 4.6: Example treatment response sets from patient 2 showing all slices acquired. Top row TR, middle row pre-treatment ventilation images, and bottom post-treatment ventilation images. The TR is in units of litres. White areas correspond to no significant changes in ventilation above the threshold $\sigma(\vec{r})$ *.*

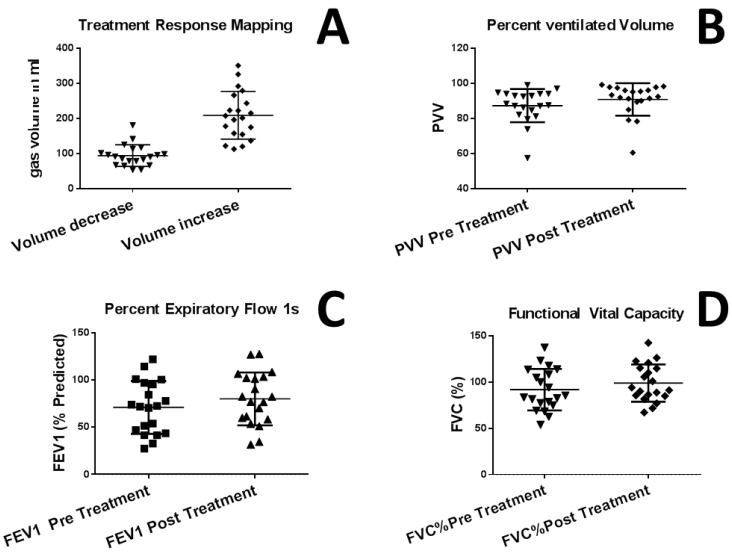

Figure 4.7: Comparison of image derived parameters: (A) – TR as volume change, (B) - %VV; and spirometry: (C) - FEV1, (D) - FVC. Response to Bronchodilator treatment was found to be significant with all methods (one-tailed Wilcoxon signed rank test, P<0.001). Although all methods show significant sensitivity to change the TR groups are more tightly clustered with clearer separation and a difference >50% between the mean values.

To assess the feasibility of this method in the assessment of a treatment over multiple visits, 6 patients were imaged in a second visit and were assessed with the same methods. Figure 4.8 shows an overview of the results, comparing FEV1, %VV and treatment response mapping. Since no further treatment was applied and patients were only given a placebo between the two visits no significant difference in ventilation distribution between the two visits was expected. Figure 4.8A reflects this, and no significant differences between ventilation increase between visits and ventilation decrease between visits could be found, in either baseline-baseline or BD-BD (Figure 4.8A).

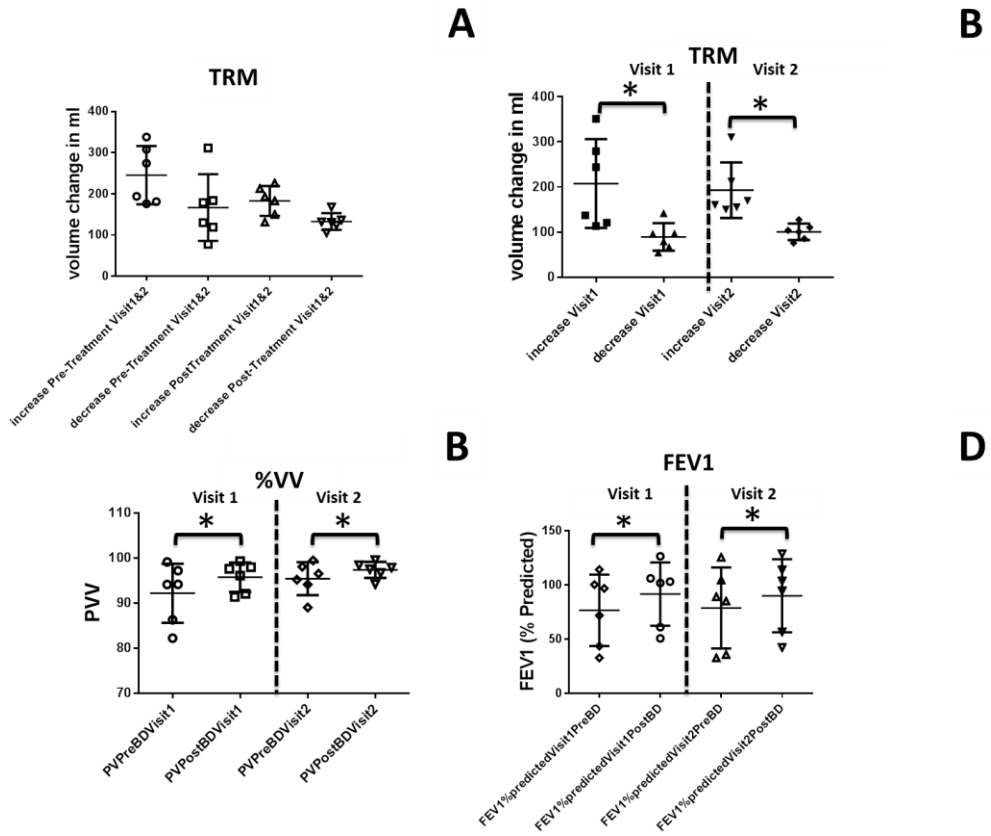

*Figure 4.8: Overview treatment response of subjects, who attended on 2 visits. For each comparison volume increase and decrease from histograms are plotted. * indicates significant difference (P<0.05)*

*(**A**) Volume changes between Visit 1 and Visit 2. First and second column show positive and negative changes in ventilation images acquired at baseline between Visit 1 and Visit 2. Third and fourth column shows changes in ventilation images between Visit1 and Visit2 after application of the bronchodilator*

*(**B**) Shows the response to bronchodilator during Visit 1 and Visit 2*

*(**C**) %VV compared from both visits before and after bronchodilator application*

*(**D**) FEV1% predicted from both visits before and after bronchodilator application*

Difference between volume increase and decrease pre and post application of bronchodilator in Visit 1 and Visit 2 were both found to be significant ($P<0.05$, one-tailed Wilcoxon signed rank test). %VV derived from the same datasets showed significance between pre-and post-bronchodilator treatment in both visits (Figure 4.8C), as did FEV1 (Figure 4.8D). These findings are in agreement with those in the Visit 1 pre and post treatment.

Since large changes in lung volume can have an impact on the outcome of the registration, the reproducibility of lung volumes was tested. Lung volumes from the baseline and the post-BD scan from all 20 volunteers were tested. The total lung volume (TLV) calculated from segmentation of the lung cavity in ^{1}H images was compared between pre- and post-treatment images. The Bland-Altman plot of the differences is shown in Figure 4.9**Error! Reference source not found.**. A mean total volume difference of less than 40 ml was found with a standard deviation of 389ml corresponding to -0.5%±8.3% of the mean lung volume. Findings show a similar mean difference (0.2%) as Horn et al. with a much higher standard deviation (SD=3.2%, [162]). This might be explained by the fact that the previous study included trained healthy volunteers, while the current study examines asthma patients who are short of breath. Nevertheless, the findings emphasise the necessity of image registration and lung volume normalization step (2) in the TRM process.

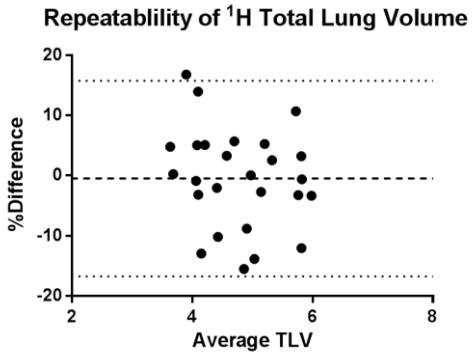

Figure 4.9: Bland-Altman plot of differences between lung volumes in litres. Dotted lines show ±1.96 standard deviations and the mean difference. Mean difference between total lung volumes -0.5% with a standard deviation of 8%.

4.4. Discussion

A method for treatment response mapping was developed for quantification and visualisation of regional changes in gas distribution in the lung. The technique was demonstrated in an asthma cohort. Single breath ventilation weighted images acquired before and after treatment were used as a basis to calculate treatment response maps. Additionally, the baseline random variability of the gas distribution in the lung was studied by acquiring two images before treatment. Regional short-term baseline physiological variability was derived from those images and used to quantify true treatment response effect.

Measuring regional ventilation changes between acquisitions caused by motion and differences in lung volume is challenging. This problem has been addressed previously [162] in the calculation of percent ventilated volume (%VV), where the acquisition of proton images and ventilation images in separate breaths reduce the repeatability of %VV calculation and registration was shown to improve reproducibility of %VV. When calculating treatment response maps, image registration was used to overcome differences in lung volume of ventilation images acquired at different breath-holds. Proton images, acquired during the same breath-hold as the ventilation images were used to calculate deformation maps that were then applied to ventilation images. This reduced registration errors introduced by morphologic changes in ventilation images arising from response to treatment. Moreover, registration reduces misalignment resulting from patient movement between scans and from repositioning patients in the scanner between imaging sessions. Registered images allow comparison of ventilation changes over multiple time points. Since the signal from lung parenchyma in ^{1}H MRI is hard to distinguish from noise, image registration relies on the outline of the lungs and blood vessels inside the lung. In diseased lungs, air-trapping could result in altered lung expansion, which might cause errors in deformation maps from image registration. Nevertheless, this error is expected to be low, since patients were aiming for the same lung inflation and volumes changes were found to be less than 1±8%.

After registration, the image normalisation process enabled comparison of signal intensities in the ventilation images from different acquisitions. The method proposed by Tzeng et al. was used [158], to compensate for differences in ^{3}He atoms reaching the lungs and polarisation levels rather than relying solely on image intensity detected in the trachea. In a second normalisation step change in concentration of ^{3}He of gas in the lungs due to changes in ventilation (e.g. airway opening or altered lung inflation) were considered.

Images were acquired in a similar position within the coil using the same sequence parameters each time, allowing a comparison of relative changes in image intensity. Changes from normalised images were calculated, allowing comparison from voxel to voxel and also comparison of size of effect between subjects. Translated to lung physiology, a negative response (red areas) in a certain lung unit corresponds to reduction in ventilation at approximately the value of TR in percent. On the other hand a positive response (green areas) implies an increase in ventilation of TR. The two effects can be converted to a volume by multiplying fractional change within a voxel with voxel volume or summarised as net effect over the histogram (compare Figure 4.10).

It is acknowledged that lung units which show very low ventilation before and after treatment, may represent a long time constant for gas washin and therefore, may not be captured accurately with a single breath imaging method. Those areas in the lung are thresholded and are hence not considered with this method. Nevertheless defects that are reflected in the %VV derived from the same data as treatment response maps and could be assessed separately with this method to add information about the efficacy of the treatment. The other difference to tidal breathing at rest results from the amount of gas breathed in: the dose was fixed to a total gas volume of 1L, rather than the individual tidal volume, and consisted of 300ml of highly diffusive ^{3}He ($D_{0helium\_in\_air}$ $\approx 0.9 cm^{2}/s$ compared to $D_{0air} \approx 0.2\ cm^{2}/s$) [149]. Considering an average total ventilated lung volume of 4,09l, then about 7% of the gas in the lung is composed of ^{3}He.

4.4.1. Baseline variability thresholding

Three methods were proposed to obtain the threshold for activation of TR. A global mean difference of the two images acquired is not sensitive to regional changes. It might be a valid method in healthy subjects where only small changes in regional ventilation from pixel-pixel can be expected within a short time period. However, a regionally specific threshold is more sensitive to redistribution of gas within the lung in the absence of treatment and is more suitable for patients where some regional reversibility of baseline ventilation heterogeneity due to underlying physiological variability at baseline is expected. It has been shown that non-ventilated regions of the lung can change size and position between scans performed on the same day in asthma [55]. This was confirmed by the baseline variability maps produced in this study, indicating local redistribution of gas in the lung (Figure 4.4G). It would be interesting to assess this repeatability more than twice before treatment. Future work could assess to what extent the regional assessment of baseline variability from two images is valid by scanning the same asthma patient multiple times before treatment.

4.4.2. Treatment response

Ventilation changes in response to bronchodilator inhalation in asthma were regionally visualised and quantified. Improvement of ventilation was found to be significant using the measures of percentage treatment response, ventilated volume and spirometry in this asthma cohort. The average net treatment response expressed as volume was found to be positive 115±74ml. Note also that volume increase and decrease clusters in Figure 4.7A are tighter and better delineated than the other measurements of %VV, FEV1 and FVC, pre- and post-bronchodilator indicating that the method may be a more sensitive outcome measure as an endpoint measurement of change. Mean increased volume was 55% higher than decreased volume over all 20 patients and therefore distinguishes much clearer changes due to treatment.

In the small subgroup of patients imaged 12 weeks later, response to bronchodilator was shown to be significant during Visit 1 and Visit 2 with all methods. Since patients were untreated during the 12-week intermediary period it is not surprising that changes between visits are not significant. Nevertheless, volume increase is 31% higher than volume decrease before bronchodilator treatment comparing both visits (Figure 4.8A, columm 1&2), which suggests a small increase in global ventilation between visits in these 6 patients. This difference is also apparent as a very small net change of ventilated volume %VV (3.39%) and FEV1 (2.72%). An explanation for this change might be the effect of the placebo that the patients were given or it may just be another effect of the small sub-sample size.

Figure 4.8A visualises changes in ventilation between repeated visits (Visit 1 and Visit 2). Nevertheless, non-zero TR suggests a redistribution of gas in the lung when measuring ventilation under similar conditions (e.g. same time of the day, same imaging hardware) with a 3 month gap.

In comparison to %VV or clustering image intensity [153] as a quantitative metric, treatment response mapping maximises regional information measured in each voxel by calculating a continuous metric based on changes in image intensity for each voxel. In contrast to Tzeng et al. [158], this method did not only compare the heterogeneity measure of ventilated volume fraction in the lung, but registration of images from different acquisitions and visits enables a quantification and visualisation of response to treatment or challenge on a regional basis.

4.4.3. Conclusion

Treatment response mapping enables quantitative evaluation of regional ventilation changes from hyperpolarised gas MRI. The presented method was shown to be suitable for longitudinal studies

and the absence of ionising radiation makes it particularly suitable for application in paediatric populations. Treatment response mapping can be transferred to other patient populations and interventions than those presented here. FEV1 (as a commonly applied endpoint for studies) and %VV (as an established parameter derived from ventilation images) show only global net changes in ventilation. Nevertheless, this method is sensitive to regional and directional changes of gas distribution on a continuous scale. Changes in ventilation are measured in an observed area within the lung and are quantitatively expressed as percentage change response to treatment (TR) or as the corresponding change of regional gas volume. Based on the same ventilation images used to calculate %VV, the regional information is maximised by taking image intensity changes into account and generating a single number for each measured voxel derived from pre- and post-treatment images. For the comparison presented in this chapter, the information content from treatment response maps reduced to two numbers (ventilation increase and decrease expressed in a volume) in order to perform statistical analysis to test for significant changes as would be done for global metrics such as in %VV and FEV1 in response to treatment. Nevertheless, these number are condensed information from each measured voxel in the lung and the TR maps themselves are indeed intended as a regional quantitative means of assessment of treatment. Condensing the voxel information into a single index risks sacrificing the sensitivity to regional change. Figure 4.10 demonstrates in 5 example slices from different volunteers of the asthma cohort how visually the effects of the treatment response can be seen in the maps.

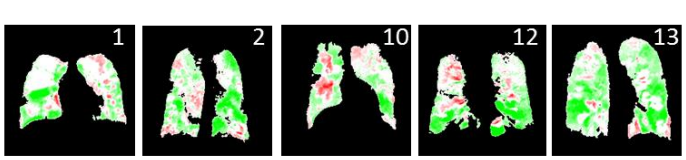

	1	2	10	12	13
Net-change [ml]	143	297	111	227	212
Ventilation increase [ml]	223	351	197	326	279
Ventilation decrease [ml]	79	54	86	99	67

Figure 4.10: Selected example slices from TR maps from different volunteers (*indicated in the maps*). *For each example the net-effect as a net gas-volume change and the positive and negative volume (ventilation increase and ventilation decrease) are given.*

Chapter 5 Quantification of regional fractional ventilation in human subjects by measurement of hyperpolarised ^{3}He washout with 2D and 3D MRI[6]

5.1. Introduction

Following the introduction of new methods for quantitative evaluation of ventilation images in Chapter 3 and Chapter 4, this chapter describes a new method to derive a regional quantitative parameter of ventilation from imaging gas washout over multiple breaths [163]. The experimental design of multiple breath washout imaging (MBW-imaging) is presented and evaluated in a preliminary study on 7 healthy volunteers. A 2D method and a 3D method are tested. The parameter of fractional ventilation derived from washout imaging is compared to an independently globally measured gas turnover. The gravitational effect of ventilation gradient from anterior to posterior when supine as described in the literature is investigated in healthy subjects.

Different imaging modalities have been shown to be capable of regionally resolving VH; for example ^{133}Xe scintigraphy [124, 164], xenon-enhanced computed tomography (CT) [165, 166] and ^{13}N-N_2 positron emission tomography (PET) [167]. However, all of these methods use ionising radiation, thus limiting their application in paediatric patients and for repeat longitudinal studies of lung physiology in human subjects.

MRI methods for quantitative ventilation imaging have been proposed, using both proton (^{1}H) lung MRI and hyperpolarised gas lung MRI. O_2-enhanced ^{1}H-MR imaging is sensitive to T_1 changes of the pulmonary tissue and the perfused blood-pool in the lungs when pure oxygen is inhaled. Physiological parameters, such as specific ventilation that is directly related to fractional ventilation (see Section 2.6), have been derived from the signal changes that the inhaled oxygen causes in the surrounding tissue and blood pool [25]. However, the technique is not a direct measurement of the O_2 gas distribution itself in the lung (lung ventilation) but rather the signal enhancement it causes in ^{1}H in tissue.

---

[6] This chapter is based on an article published in the Journal of Applied Physiology: Quantification of regional fractional ventilation in human subjects by measurement of hyperpolarized ^{3}He washout with 2D and 3D MRI. [1]FC Horn, [1]MH Deppe, [1] H Marshall,[1] J Parra-Robles, and [1]JM Wild; Journal of Applied Physiology (1985), Volume 116, Issue 2, pages 129-139;

1. Academic Radiology, Department of Cardiovascular Sciences, University of Sheffield, UK

Quantitative multiple-breath imaging with hyperpolarised ^{3}He MRI was initially proposed by Deninger et al [168] based on the signal build-up of gas washin and demonstrated in rodent lungs. An optimised protocol reducing the number of breaths needed has since been shown to be feasible in mechanically ventilated large animals [169]. The requirement for large volumes of ^{3}He, and mechanical ventilation, mean that washin methods have been limited to animal studies at present.

In this chapter washout imaging is used to derive regional fractional ventilation as a quantitative measure of gas turnover. The concept of fractional ventilation as the ratio of fresh gas entering a volume unit to the total end inspiratory size of the unit is explained in Chapter 2.6 'Multiple breath washout models - modelling gas mixing'.

The aim of this development work on 7 healthy subjects was to develop a technique for multiple breath washout imaging using hyperpolarised gas MRI which is capable of producing maps of fractional ventilation while being practical for the clinical use in human subjects. For this reason a fast 2D imaging protocol for minimal interruption of the breathing pattern and a 3D protocol providing full lung coverage are introduced and evaluated. The technique was compared to an independent measure of gas turnover and is evaluated in 4 healthy volunteers.

5.2. Materials and methods

5.2.1. Human subjects

In this initial study 7 healthy subjects were imaged, following informed consent and approval of the national research ethics committee Table 5.1 gives an overview of the specific details of the volunteers.

Subject	Sex	Age, years	Weight, kg	TV, litres*	FEV1, % predicted**	FVC, litres (% predicted)**
Volunteer1	M	35	60	0.85	96	4.69(100)
Volunteer2	M	27	79	0.74	113	2.96(86)
Volunteer3	F	31	62	0.70	115	4.28(122)
Volunteer4	F	26	51	0.60	103	3.51(100)
Volunteer5	M	23	77	1.01	108	6.56(111)
Volunteer6	M	30	75	0.69	82	5.1(94)
Volunteer7	M	27	79	0.77	108	6.38(116)

*Table 5.1: Subject characteristics; *at rest, supine and outside scanner; ** Calculated according to guidelines by Quanjer et al. [84]*

5.2.2. Multiple breath washout protocols

MBW imaging was performed using a single dose of hyperpolarised ^{3}He gas, which was inhaled from a one litre bag from a starting position of functional residual capacity (*FRC*) similar to the protocol used in routine single breath-hold ventilation weighted imaging with ^{3}He. The assumption is that the gas is washed in to equilibrium across all lung units before washout commences on subsequent breaths. The single breath gas washin procedure does not, however, represent a steady state of gas concentration in the presence of obstructive lung disease and regional VH. It has been shown before that during the course of a breath-hold there is a time dependent ventilation component of ^{3}He in partially obstructed lungs [170]. Nevertheless, the more dominant effect on tracer gas turnover is the washout of gas from the lungs.

During the washout, a fraction of the hyperpolarised ^{3}He in every volume element (voxel) $\Delta V = \Delta x \cdot \Delta y \cdot \Delta z$ at position (x,y,z) in the lungs is replaced by air with each subsequent breathing cycle (exhalation – inhalation) directly translating into a signal intensity decay. From this signal decay the fractional ventilation $\boldsymbol{r}$ can be calculated independent of the initial concentration. Values range between $\boldsymbol{r} = 0$, meaning no gas is replaced, and $\boldsymbol{r} = 1$ meaning all gas is completely replaced with each breath like in conducting airways. Fractional ventilation $\boldsymbol{r}$ can only be calculated for voxels with sufficient initial concentration of the tracer gas. Since the decay is monitored within each voxel, fractional ventilation $\boldsymbol{r}$ is the average decay of the whole unit that might include different smaller structures within the imaging voxel.

A schematic of the MBW imaging acquisition timing is outlined in Figure 5.1. Images are acquired separated by a fixed delay time, denoted by Δt. The delay is sufficiently long to allow subjects to perform a breathing cycle (exhale – inhale) between data acquisitions. The first two images are acquired during a calibration breath-hold to account for signal losses due to gas depolarisation that are not related to gas washout. This delay before the washout starts allows time for the gas to achieve an equilibrium concentration and to fill airspaces that are filled at a later stage in breath hold due to partial obstruction [170].

Prior to inhaling the hyperpolarised gas for the wash-out experiment, the whole procedure was tested. Subjects were inside the scanner breathing instructions were given and the imaging sequence was being played out by the scanner to mock the experiment. This allowed subject to get used to timing and breathing during the image acquisition. The tidal volume was acquired during those test runs and qualitative feedback was given to subjects about their breathing efforts. After 2-3 test runs subjects were considered to be well trained for the experiment using hyperpolarised ^{3}He.

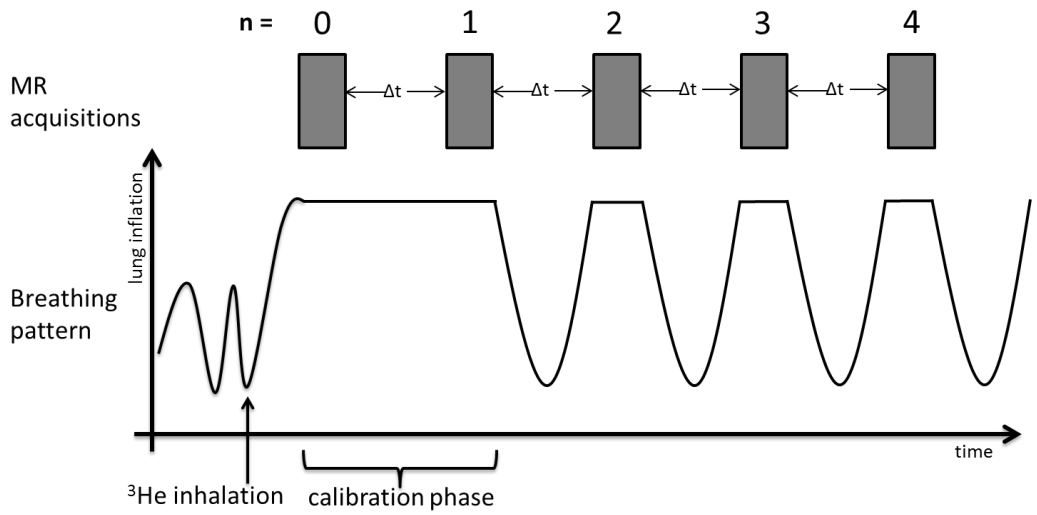

Figure 5.1 : Timing of image acquisitions and breathing manoeuvre. Images were acquired at a fixed delay Δt. Subjects held their breath during the first two acquisitions, constituting the calibration phase, and performed a single breathing cycle (exhale – inhale) between subsequent acquisitions.

A 2D imaging protocol was developed for assessment of gas washout in two parallel sagittal slices covering the central parts of both the left and right lungs. This approach was then extended to a 3D whole lungs imaging method in a second protocol with different timings. Both follow the schematic outlined in Figure 5.1 and are described below in further detail.

5.2.3. 2D washout acquisition protocol (2D-WO)

Subjects inhaled a mixture of ^{3}He and N_2 from FRC. The dose consisted of ~100 mℓ of ^{3}He topped up with N_2 to match the subject's tidal volume and was delivered in a Tedlar bag. Following the calibration breath-hold (purpose of calibration explained in Section 5.2.7), subjects were instructed to breathe in synchronisation with the timing of the sequence for data acquisition (as shown in Figure 5.1). The fixed delay time Δt was empirically set at 4s to ensure comfortable breathing. This protocol was performed in all healthy subjects and repeated twice for each subject to assess reproducibility.

5.2.4. 3D washout acquisition protocol (3D-WO)

To perform washout imaging with 3D images, a dose of 200 mℓ ^{3}He was mixed with 800 mℓ N_2 and inhaled from *FRC*. Similar to the 2D-WO acquisition, subjects breathed in synchronisation with the sequence timing after a calibration breath-hold (as shown in Figure 5.1). Due to the increased acquisition duration needed for volume coverage with the 3D sequence (2.6s) the fixed delay Δt was increased to 5s.

5.2.5. Flow measurement during washout imaging experiments

During the washout phase of the experiments tidal volume, flow and pressure were monitored at the mouth using a RSS 100HR research pneumotachograph (Hans Rudolph, Shawnee, KS) with a series 3830/4830 linear screen sensor (Hans Rudolph, Shawnee, KS), which allows a sampling interval of 20 ms as shown in Figure 5.2A. Recorded flow, pressure and volume are shown in Figure 5.2B. The apparatus was tested in the MRI environment for compatibility and was not found to reduce image quality. A disposable filter was connected to the sensor to avoid contamination (Model 2820, Vitalograph, Buckingham, UK). The flow data were also used to assess the reproducibility of tidal volume during the wash-out experiment.

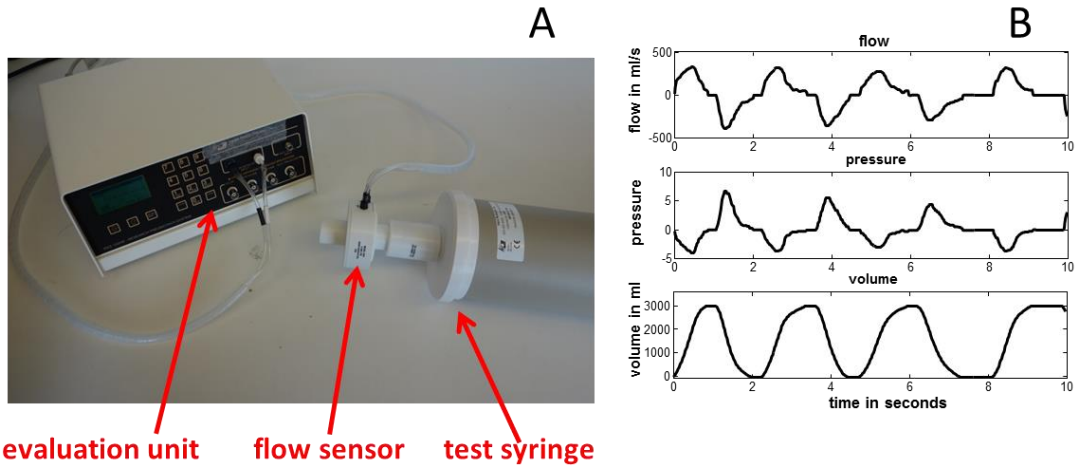

Figure 5.2: (A) Setup of the pneumotachograph evaluation unit measuring the pressure differences connected to the flow sensor. To calibrate setup a 3L test syringe is used. (B) Recoding from the evaluation unit using the 3L test syringe: Flow, pressure and volume are evaluated.

5.2.6. ^{3}He MR hardware and pulse sequences

MRI experiments were performed on a 1.5T Signa HDx scanner (GE, Milwaukee, WI, USA) using a quadrature wrap-around transmit-receive chest RF coil tuned to 48.62 MHz (Clinical MR Solutions, Milwaukee, WI, USA). ^{3}He was hyperpolarised to ~25% using spin-exchange optical pumping apparatus (GE Healthcare, Amersham, UK) under a site-specific regulatory licence.

In the case of the **2D acquisitions**, the pulse sequence parameters of the spoiled gradient echo sequence (SPGR) were: a 64 × 32 matrix (frequency × phase), 38x38 cm field-of-view, echo time (TE) 1 ms, repetition time (TR) 3.38 ms, receiver bandwidth (RBW) 31.3 kHz, flip angle ~ 4° and centric phase encoding order. Two sagittal slices were acquired with a slice thickness of 50mm to mitigate effects of intra-slice gas diffusion during the experiment [50] and to cover major parts of the left and right lung. The acquisition duration for each time-point was 0.2s.

In the case of the **3D acquisitions**, a SPGR sequence with a matrix of 32x32x32, 38x38 cm field-of-view with a slice thickness of 10mm , TE 0.75ms, TR 2.5ms, RBW 32.3 kHz, flip angle ~1° and centric phase encoding were used. The flip angle was chosen deliberately small (half of the optimum value [42]) to ensure sufficient signal to noise ratio (SNR > 15) in at least 4 acquisitions of the time series. The duration of image acquisition for each time-point was 2.6s.

An estimate of end inspiratory lung volume (LV) was required in order to calculate the volume turnover for the 2D ^{3}He washout acquisitions. LV estimates were made from segmentation of ^{1}H anatomical images that were acquired using a multi-slice balanced steady state free precession sequence covering the whole lung. Parameters were: slice thickness of 10mm with 22-24 slices, matrix of 256x192 (frequency x phase), TR 2.8ms, RBW 250 kHz and flip angle of 50°. To minimise movement of the subjects between the ^{3}He washout and ^{1}H scans, the scanner's body coil was used to acquire the ^{1}H scans with the ^{3}He coil in-situ. Comparable lung inflation volumes to those during the washout protocol (2D-WO) were achieved by inhalation of a bag of air containing the same volume used for the washout imaging from the same initial volume (*FRC*). The scan was performed twice and the average of both volumes was used to calculate the volume turnover.

5.2.7. Calculation of fractional ventilation from washout imaging data

The fractional ventilation parameter ***r*** was calculated from the signal decay during the washout. Altogether three different mechanisms contribute to the overall signal decay: (a) the turnover (washout) of gas, (b) T_1 relaxation of the polarisation of the hyperpolarised gas and (c) the depolarisation of magnetisation from the small flip angle radiofrequency (RF) pulses that are used to acquire the MR images. To calculate ***r***, the mechanisms of signal decay b) and c) need to be separated from a). These two effects combined can be measured from the ratio of the signal in the two images acquired during the calibration breath-hold assuming that the ^{3}He T_1 is reproducible between breaths, a condition addressed in the discussion. All subsequent images can then be corrected for decay of signal that is non-washout related.

During washout, the evolution of the ^{3}He signal in a voxel measured by a spoiled gradient echo sequence can be modelled with [171]:

$$S(t) = I(t) \cdot e^{-\frac{t}{T_1}} \cdot (\cos\alpha)^{N_{RF}} \qquad \text{Eq. [5.1]}$$

Where $S(t)$ is the signal intensity at time t, $I(t)$ is a function describing the density of ^{3}He gas in the lungs at a given breath, $e^{-\frac{t}{T_1}}$ the losses from T_1 decay and $(\cos\alpha)^{N_{RF}}$ the signal

depolarisation after N_{RF} radiofrequency pulses with a flip angle α. Due to the finite polarisation of the inhaled gas, the signal is only measured at discrete cyclic time points with a delay Δt. The equation can then be reformulated to:

$$S(n) = I(n) \cdot \left(e^{-\frac{\tau+\Delta t}{T_1}} \cdot (\cos\alpha)^N \right)^n \qquad \text{Eq. [5.1]}$$

With *S*(n) representing signal intensity of a volume element acquired at time step *n* with a total delay of $\tau+\Delta t$ from the start of the previous acquisition, where τ is the duration of an acquisition and Δ*t* is the gap between two acquisitions and *N* is the number of RF pulses used to acquire an image in a single time-point acquisition. τ, Δt, α and *N* are all kept constant during the experiment. Assuming that T_1 remains constant and neglecting gas diffusion into the blood stream (due to the very low solubility of ^{3}He), the equation can be simplified to:

$$S(n) = I(n) \cdot C^n \qquad \text{Eq. [5.2]}$$

Here, *C* is a constant correction factor that combines the effects of both longitudinal relaxation and RF depolarisation, *I*(0) = *I*(1) because no washout takes place during the calibration phase at breath-hold (Figure 5.1). This enables the calculation of a local correction factor for every voxel position (*x*,*y*,*z*) :

$$C = \frac{S(1)}{S(0)} \qquad \text{Eq. [5.3]}$$

Having obtained *C*, corrected images of absolute ^{3}He gas density, *I*(*n*) can be derived for the subsequent time series of acquired images *S*(*n*) from Eq. [5.3]. The signal decay in the corrected images *I*(*n*) can thus be regarded as being due to washout of ^{3}He gas alone and fractional ventilation *r* (see Figure 2.26 in Section 2.6)can then be calculated from:

$$I(n) = (1-r)^{n-1} \cdot I(1) \qquad \text{Eq. [5.4]}$$

for n ≥ 1 with n = 0 being the first image in the calibration-breath-hold. Logarithmic conversion transfers this problem into a linear fitting problem:

$$\ln I(n) = \ln(1-r) \cdot (n-1) + \ln(I(1)) \qquad \text{Eq. [5.5]}$$

that is solved as follow:

$$r = 1 - e^{\frac{\partial \ln(I(n))}{\partial n}} \qquad \text{Eq. [5.6]}$$

From a least squares fit of the corrected signal intensity decay ($I(n)$) Eq. [5.6] shows how fractional ventilation can be obtained for each voxel as a quantitative measure of regional gas washout.

Using Eq. [5.3] this can be expressed in terms of $S(n)$ as the measured signal decay:

$$r = 1 - e^{\frac{\partial \ln(S(n)}{\partial n} - \ln(C)} \qquad \text{Eq. [5.7]}$$

5.2.8. Specific details of image processing

A flowchart of the image post-processing steps for a 2D acquisition is shown in Figure 5.3. The raw data acquired were reconstructed by 2D FFT after applying a Gaussian filter (σ = image matrix/2) to the k-space raw data using custom-written code implemented in Matlab (Mathworks, Natick, MA, USA). An example 2D dataset is shown in Figure 5.3A. Image registration is necessary to compensate for motion and lung volume changes throughout the experiment, which are prominent around the diaphragm, potentially leading to unrealistic values of fractional ventilation.

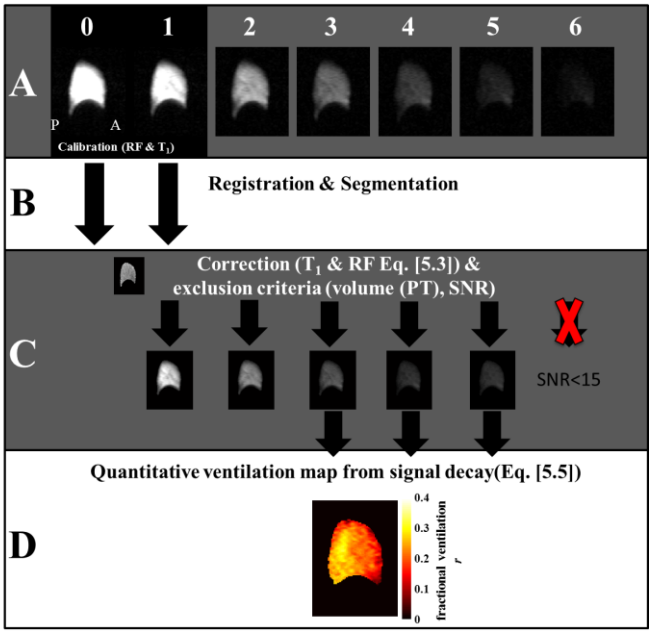

Figure 5.3: Flow chart of the data processing steps used to obtain fractional ventilation parameter r from a 2D dataset.(A) Acquired images of the MBW-imaging protocol. (B) Image registration and segmentation. (C) Correction for T_1 and RF decay according to Equation 4.(D) Applying Equation six to calculate fractional ventilation maps.

All datasets were registered to the first image using an image registration algorithm as described in greater detail by Barber et al. [161]. To account for the different intensity ranges resulting from the washout of gas, the images are first normalised to the maximum signal of the lung volume at each time point before applying the registration algorithm and mapped back to their original intensities after registration. An in silico simulation using a lung virtual from the outline from a segmented dataset was used. The virtual lung was filled with defined values of image intensity to test the algorithm, registering two different inflation states. A comparison of original data with the registered data showed that the registration algorithm did not affect signal intensity. The registration algorithm is based on an adjusted sum-of-squared intensity differences as similarity measure (SSD).

After registration, images are segmented using a threshold-based mask created from the first image which has the highest signal to noise ratio (SNR_{2D} >150 ; SNR_{3D}> 200). The threshold is established using Otsu's method [172] as a fast method to obtain a threshold. This uses the signal threshold level which maximises the between-class variance of the two clusters defined by the applied threshold (foreground and background) in the histogram of an image. The images were then filtered using a median filter with a 3x3 neighbourhood to reduce the effect of noise. Afterwards images with SNR < 15 were excluded from further evaluation. SNR was calculated as the ratio of mean signal intensity of the whole segmented lung to the standard deviation of the noise. A second segmentation is then applied using a mask created from the last acquisition with SNR≥15 of the washout cycle (Figure 5.3D). The second segmentation excluded lung regions with no signal left after the washout (e.g. trachea) and guaranteed that the SNR in each pixel in all voxels was at least 15. This mask is then applied to all images. The segmentation is followed by the correction for T_1 and RF depolarisation described above in Eq. [5.2] (Figure 5.3C). Finally, Eq. [5.5] is evaluated on a pixel by pixel basis to calculate the fractional ventilation r for each voxel using a least squares algorithm (Figure 5.3D).

As a final step the lung volumes and breathing were checked for reproducibility due to their direct impact on the fractional ventilation (compare also Section 6.2). Recordings from the pneumotachograph were evaluated and the mean tidal volume over the whole experiment was calculated. Tidal volume changes ±15% of the mean value resulted in an exclusion of the two sequential time-points to avoid major changes of fractional ventilation between breaths (due to altered breathing efforts). In addition the lung volume (LV as segmented from the individual time-steps) of the 3D acquisition was taken into account and for changes of LV >10% compared to the mean LV the individual acquisition was excluded.

5.2.9. Gravitational evaluation of fractional ventilation

To evaluate the effects of gravity on regional ventilation, each map was divided into strips of 2cm running length-wise in the superior-inferior direction, orthogonal to the direction of gravity when the subject is supine in the MRI scanner, and mean *r* was calculated for each strip. The first and last strips were excluded from the evaluation of gravitational slopes to omit upper and lower borders.

5.2.10. Comparison of imaging and pneumotachograph measurements of ventilation

The values of fractional ventilation obtained from washout imaging were compared to the total gas volume turnover measured using the pneumotachograph and lung volume from MRI. With knowledge of the inspiratory lung volume, LV (from the imaging data), and the tidal volume, TV, (from the pneumotachograph), the gas volume turnover of the whole lungs with each breath can be calculated [65, 171]:

$$\bar{f} = \frac{TV}{LV} \qquad \text{Eq. [5.8]}$$

In the case of the 3D protocol, LV, was obtained by segmenting the 3D ventilation images acquired for each breathing cycle and taking the mean value. The images were segmented using a threshold determined by Otsu's method [172]. In the case of the 2D protocol the average inspiratory lung volume was determined from manual segmentation of the signal void (air space) in the additional proton scans acquired. This method has previously been shown to give good estimates of LV [57]. This measurement can be considered as independent of the ^{3}He MR measurements of fractional ventilation. Even though the same dataset is used to calculate gas volume turnover and fractional ventilation for the 3D protocol, the information is used in a different way. While the binary segmented images from the calibration phase are used to return the lung volume as part of calculation of gas turnover, for calculation of fractional ventilation, the image intensity itself as a function of time is required.

5.2.11. Comparison of fractional ventilation from 2D and 3D protocols

To directly compare the mean fractional ventilation of the 2D maps with the 3D maps it is assumed that the two thick slice 2D maps represent most of the lung volume. The tidal volume during the washout phase of the experiment directly influences the values of *r*:

$$r_{global} = \frac{V_f}{V_f + V_r} = \frac{TV}{TV + FRC} \qquad \text{Eq.[5.9]}$$

and is dependent on the subject's voluntary breathing. However, as FRC is common to both experiments, mean global fractional ventilation values measured with the 2D protocol are converted using Eq. [5.9] for comparison with those measured with the 3D protocol:

$$FRC = LV - TV_{2D-WO} = \frac{TV_{2D-WO}}{r_{2D-measured}} - TV_{2D-WO}$$
$$r_{global\_conv} = \frac{TV_{3D-WO}}{TV_{3D-WO} + FRC} \qquad \text{Eq.[5.10]}$$

where TV is the tidal volume measured during washout from the 2D acquisition (2D-WO) and the 3D acquisition (3D-WO) respectively, $r_{2D-measured}$ represents the fractional ventilation measured with the 2D protocol, and r_{global_conv} is the fractional ventilation measured with the 2D protocol scaled for comparison with the fractional ventilation measured with the 3D protocol.

5.2.12. Reproducibility

Repeatability of 2D and 3D MBW-imaging was investigated. Subjects were imaged repeatedly with the same protocol. In case of the 3D washout acquisition the gap between scans was 5 minutes. In case of the 2D dataset only Volunteer 4 was imaged within the same scan session. Repeatability of 3D datasets was tested by comparing the *r*-maps on a voxel-voxel basis and a comparison of the histograms (Pearson's correlation of mean values and standard deviations). In the case of the 2D datasets voxel by voxel correlation was performed on Volunteer 4.

5.3. Results

Table 5.1 shows subject data; weight, age and sex as well as tidal volume measured in supine at rest (TV), FEV1 and FVC in litres and % predicted [84]. All healthy volunteers had no history of respiratory or cardiac disease and were non-smokers. All subjects tolerated the imaging protocols well. A representative 2D dataset from one slice of a washout acquisition in the sagittal plane is shown in the top row of Figure 5.3. The middle row displays the images after correction for RF depolarisation and T_1 decay, which are then used to obtain a fractional ventilation map from the dataset as seen at bottom of Figure 5.3. The resulting 2D fractional ventilation maps from healthy subjects (volunteers 1- 4) are displayed in Figure 5.4 together with the corresponding histograms from the right and left lung *r* maps. Representative slices from 3D fractional ventilation maps from subjects 1-4 are shown in the axial, coronal and sagittal planes in Figure 5.5.

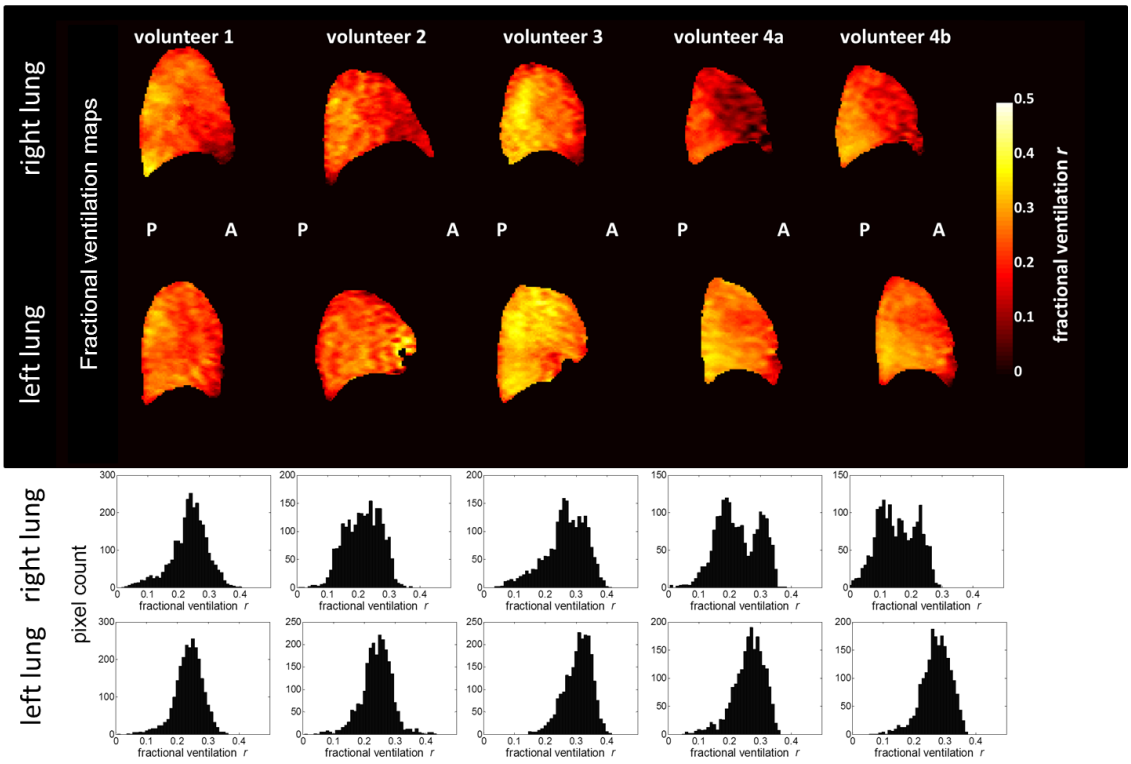

Figure 5.4: *Maps of fractional ventilation parameter r obtained with the 2D washout acquisition protocol. Sagittal slices from left and right lung are shown for 4 healthy subjects as well as histograms of distribution of r values for each lung slice.*

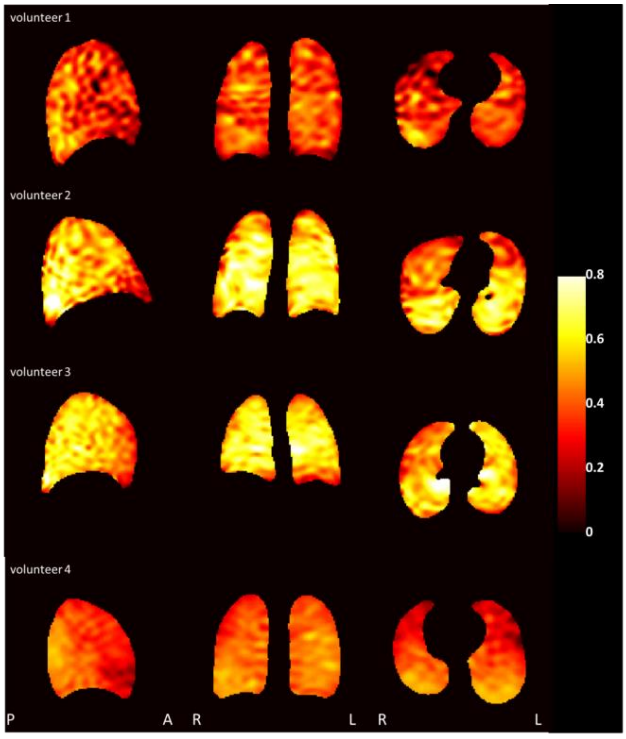

Figure 5.5: *Fractional ventilation maps from 3D washout from healthy subjects in the sagittal, coronal and axial plane (Volunteer 1-4).*

An overview of all mean fractional ventilation values from the subjects from all experiments is given in Table 5.2. The observed mean values of fractional ventilation ranged from *r* = 0.21 to 0.34 in case of the 2D protocol and from *r* = 0.16 to 0.48 in the case of the 3D protocol.

		Mean fractional ventilation (*r*) Mean (±standard deviation)		Volume turnover TV /LV (TV in litres)		Slope of *r* A-P of the right lung, cm^{-1} (%/cm of the mean *r*)		Mean fractional ventilation 2D scaled to 3D
subject	2D	2D	3D	2D	3D	2D (right lung)	3D	2D→3D
Volunteer 1	Experiment 1a	0.25(0.04)	0.35(0.10)	0.22 (1.0)	0.25 (1.3)	0.006(2.3)	0.015(4.3)	0.31
	Experiment 1b	0.26(0.07)				0.006(2.2)		
Volunteer 2	Experiment 2a	0.26(0.07)	0.16(0.07)	0.22 (0.8)	0.17 (0.7)	0.005(1.9)	0.0140(6.35)	0.23
	Experiment 2b	0.24(0.06)	0.19(0.09)			0.003(1.1)	0.0088(5.07)	
Volunteer 3	Experiment 3a	0.28(0.05)	0.28(0.09)	0.31 (0.8)	0.22 (0.7)	0.007(2.5)	0.0030(1.07)	0.27
	Experiment 3b	0.34(0.06)	0.30(0.09)			0.009(2.7)	0.0003(0.35)	
Volunteer 4	Experiment 4a	0.22(0.08)	0.48(0.10)	0.18 (0.5)	-	0.013(4.4)	0.0143(3.46)	-
	Experiemnt 4b	0.30(0.07)	0.43(0.08)			0.013(9.9)	0.0101(2.32)	
Volunteer 5	Experiment 5a	0.21(0.13)	0.17(0.07)	0.33 (1.4)	0.12 (0.6)	0.007(3.3)	0.0004(0.27)	0.10
	Experiemnt 5b		0.18(0.07)				0.0024(1.32)	
Volunteer 6	Experiment 6a	0.26(0.10)	0.25(0.09)	0.25 (1.0)	0.20 (0.9)	0.016(6.1)	0.0010(0.42)	0.24
	Experiemnt 6b		0.26(0.08)				0.0138(4.38)	
Volunteer 7	Experiment 7a	0.23(0.08)	0.19(0.09)	0.12 (0.5)	0.12 (0.5)	0.008(3.6)	0.0077(4.04)	0.23
	Experiemnt 7b		0.19(0.09)				0.0031(1.66)	

Table 5.2: O*verview values 2D and 3D washout experiments. TV = Tidal Volume; LV = inspiratory Lung Volume. In the case of Volunteer 4 the flow-recording failed, therefore no tidal volumes could be extracted from this dataset.*

5.3.1. Gravitational effects of fractional ventilation

The gravitational trend of increased fractional ventilation from anterior to posterior (A-P) in Volunteer 2 is shown in Figure 5.6 which also demonstrates the intra-subject repeatability of the method, with the gravitational trend being generally well reproduced despite some variation in the actual *r* values returned in a given strip from a given experiment. Regional ventilation is known to be higher in gravitationally dependent regions than in non-dependent regions [25, 65, 173]. This ventilation gradient from A-P was observed in both the 2D and 3D *r* maps and is exemplified in the anterior to posterior profiles derived from a 2D washout in two slices in Figure 5.6. In the case of the 2D protocol, the slices in the left lung were acquired more laterally than those in the right lung such that motion artefacts from the heart could be avoided (Figure 5.6B). Those slices were therefore under less gravitational compression from any overlying mediastinal tissue mass and are therefore not discussed in further detail here. The gravitational slopes of *r* from A-P in the right lung are shown in Table 5.2 for all subjects. Gravitational effects from repeated experiments show a significant correlation ($r = 0.65$, $P < 0.05$). This has been demonstrated qualitatively before [174].

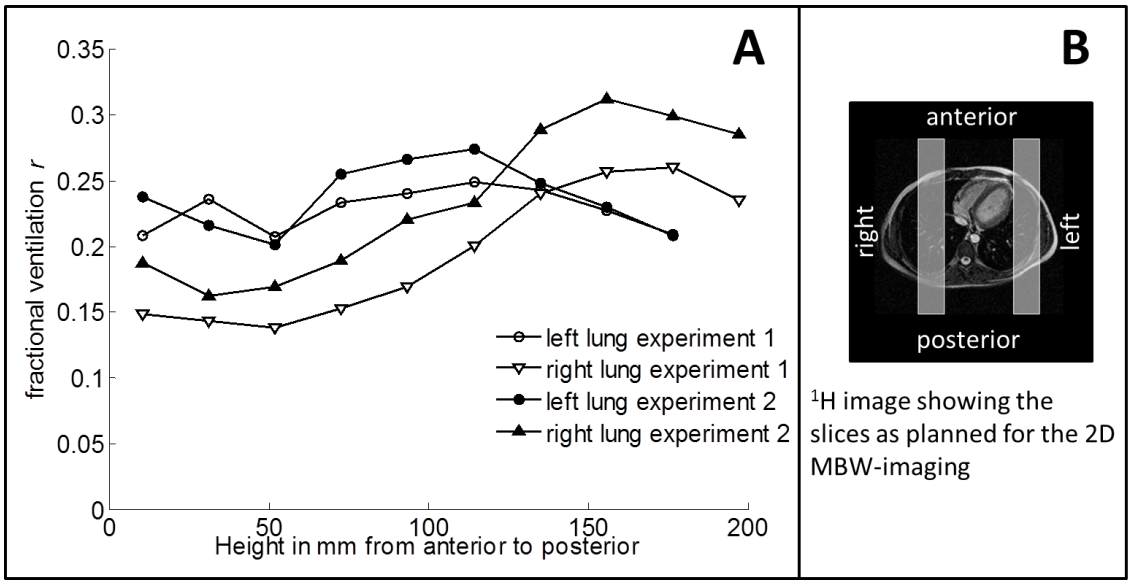

*Figure 5.6: (**A**) Gravitational effects from anterior to posterior as seen in the left and right lungs of volunteer 2 from two 2D washout datasets. The repeatability between the two scans can be observed. The right lung shows an increase in fractional ventilation between anterior and posterior parts, while the slices in the left lung do not. (**B**) The slices in the left lung are positioned further lateral and are therefore under less gravitational compression from overlaying mediastinal tissue mass.*

5.3.2. Comparison of imaging and pneumotachograph measurements of ventilation

Figure 5.7 shows comparison of the mean fractional ventilation values from gas washout imaging with the global gas volume turnover obtained from the flow measured with the pneumotachograph at the mouth and the total inspiratory volume as segmented from the breath hold MRI volume images. The dead-space volume of the upper airways as measured from the ^{3}He images (NB this was excluded from the fractional ventilation calculations) was in total 150mℓ, including the dead space volume of the pneumotachograph and the filter (70mℓ). This total dead space volume was subtracted from the measured tidal volume. A significant correlation of $r = 0.67$ ($P < 0.001$) was found between the two measures. Despite this good Pearson's correlation (of the best fit to all points) the gas turnover is systematically lower. The assessment of LV from ventilation images and anatomical images is not a precise measure of true LV, since it is hard to account for the exact contribution of tissue and blood in LV.

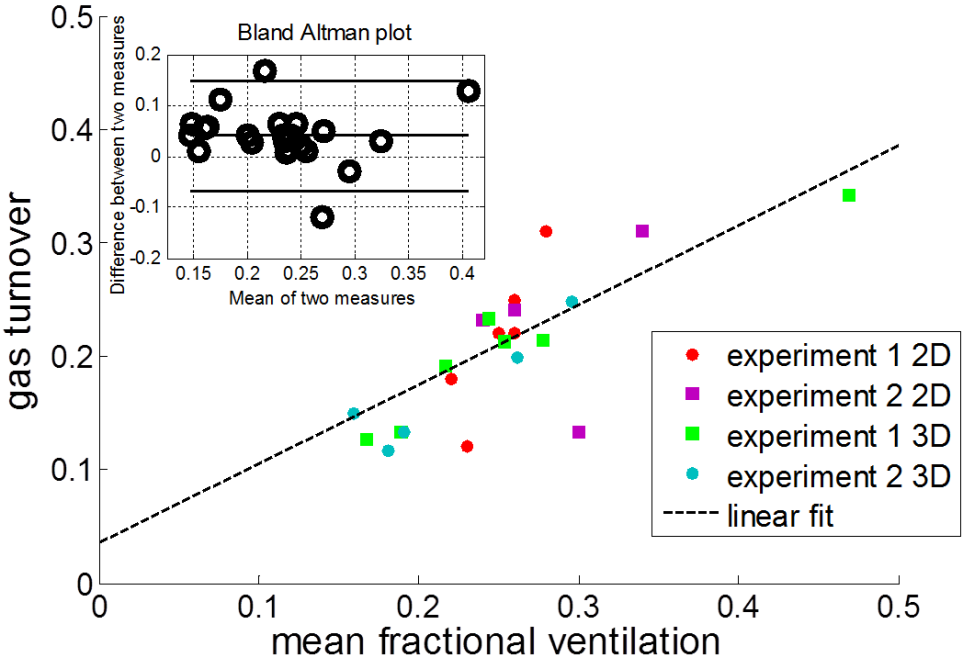

Figure 5.7: *Comparison between the gas volume turnover (tidal volume measured by pneumotachograph divided by total lung volume measured by MRI) and the measured global mean fractional ventilation from the 2D and 3D washout protocols including the Bland-Altman plot in the top left corner. Pearson's correlation r = 0.67 (P < 0.001, of the best fit to all points), Bland-Altman analysis shows a mean difference = 17.2% (standard deviation = 23.7%).*

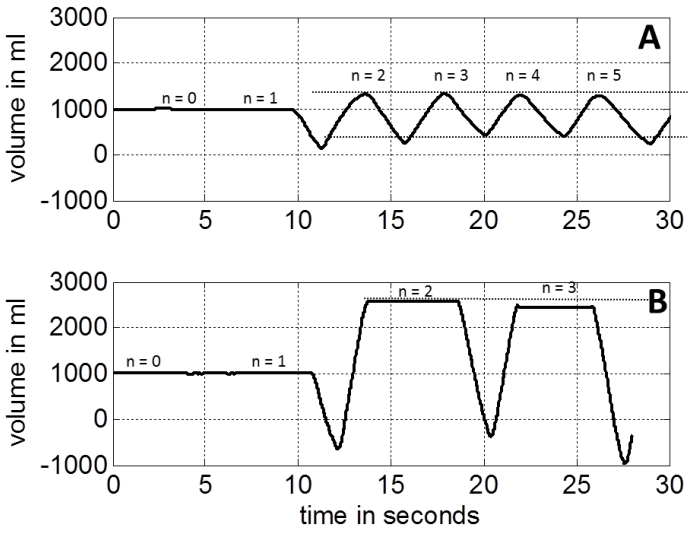

Figure 5.8: *Pneumotachograph recordings for subject 4 during (**A**) a 2D acquisition and (**B**) a 3D acquisition. n = 1,2,3,4,5 numbers the respiratory cycle in which the datasets were acquired.*

5.3.3. Comparison of fractional ventilation from 2D and 3D protocols

The last column in Table 5.2 shows the fractional ventilation measured with the 2D protocol converted to corresponding 3D fractional ventilation values using Eq. [5.8]. The comparison accounts for the dead space of 150mℓ. A Bland-Altman analysis showed a relative mean difference of 5.9% with standard deviation of ±27.2%. The correlation was not found to be significant.

5.3.4. Repeatability of washout measurements

Figure 5.9A and B show the comparison of two experiments from Volunteer 4 on a pixel by pixel basis from the 2D and the 3D protocol, respectively. Corresponding experiments were performed within the same session and the volunteer was not moved between the acquisitions. A significant Pearson's correlation of r= 0.85 (P < 0.0005) was found in the case of the 2D protocol and r= 0.74 (P < 0.0005) in the case of 3D protocol. A Bland-Altman analysis of the datasets from Figure 5.9 resulted in a relative mean of difference of 2.9% (2D) and 10.9% (3D) with a standard deviation of ±12.1% (2D) and ±13.5% (3D).

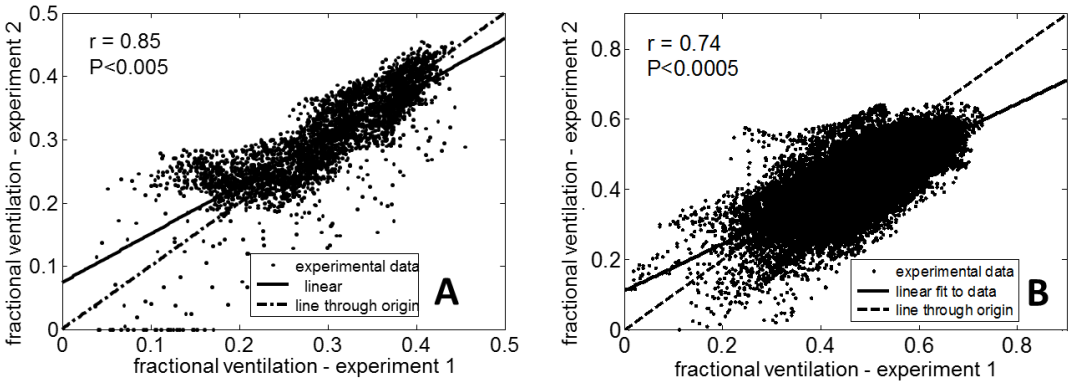

Figure 5.9: *(A) Correlation on a pixel by pixel basis of two 2D washout experiments of Volunteer 4 acquired in the same session (Pearson's correlation of r = 0.85 and P<0.005). (B) Correlation on a pixel by pixel basis of two 3D washout experiments of Volunteer 4 acquired in the same session (Pearson's correlation of r = 0.74 and P<0.005). Pearson's correlation was done on the best fit to data (continuous line).*

Table 5.3 shows an overview of the repeatability test results comparing 3D MBW-imaging in 6 volunteers. All datasets show significant correlations r = 0.5 or greater. In addition a Bland-Altman analysis was performed and the results are listed in Table 5.3. In addition fractional ventilation maps were divided along the major axis into anterior-posterior, left-right and superior-inferior into 8 regions of roughly equal size (Figure 5.10).

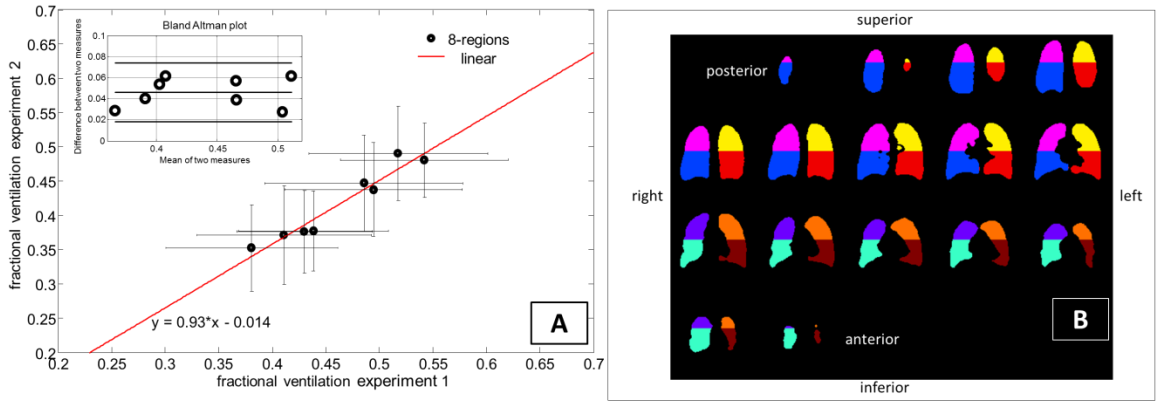

Figure 5.10: *(A) Correlation and Bland-Altman plot of 8-region comparison from Volunteer 4. Errorbars derive from the standard deviation of fractional ventilation in each of the regions. Black dots show comparison of same regions in both experiments (r = 0.97, P<0.001,), the red line is the linear fit (almost equal to unity line). A Bland-Altman analysis is shown in the top left corner (mean difference = 10.5%, standard deviation = 3.2%). (B) Lung divided into 8 regions of roughly equal size. Each colour represents one region.*

Mean values from repeated experiments performed with the 2D washout protocol from all healthy volunteers are reported in Table 5.2. A standard deviation of the mean values of 12.0% and a relative average difference of 17.0% was found. A regional comparison was not possible since data were not acquired on the same day for all volunteers. In case of a 2D slice this could account for significant differences when matching regions or voxels from different locations in the lung.

3D MBW-imaging Subject	Correlation r voxel-by-voxel comparison, all P<0.001	Bland-Altman Analysis mean difference (standard deviation)%	Correlation r 8-region comparison, all P<0.01
Volunteer 2a	0.65	34.9(25.3)	0.92
Volunteer 2b			
Volunteer 3a	0.79	8.3(17.6)	0.95
Volunteer 3b			
Volunteer 4a	0.74	10.9(13.6)	0.97
Volunteer 4b			
Volunteer 5a	0.56	6.4(33.8)	0.83
Volunteer 5b			
Volunteer 6a	0.80	2.8(17.3)	0.97
Volunteer 6b			
Volunteer 7a	0.50	1.8(33.6)	0.77
Volunteer 7b			

Table 5.3: *Comparison of repeated 3D MBW-imaging during the same session. Pearson's correlation all show highly significant correlations. In addition lungs were divided into 8 regions of equal size for comparison (divided along the main axis). Mean fractional ventilation measured in the all 8 regions shows high correlation for all volunteers tested.*

5.4. Discussion

This work of methodical development has shown how quantitative maps of fractional ventilation can be acquired in under a half minute by monitoring the washout of a single dose of hyperpolarised ^{3}He gas. This method was shown to work with a 2D acquisition protocol that allows synchronised breathing close to calm tidal breathing with very small interruptions. The same method was also extended to a 3D acquisition allowing the assessment of regional fractional ventilation values from the whole lung.

The mean global values of fractional ventilation were compared to an independently-measured value of whole lung gas turnover and significant agreement was found (Figure 5.7). The average of the mean values of fractional ventilation obtained from all 7 healthy volunteers with the 2D protocol (r = 0.26±0.04) correspond to specific ventilation (SV) of 0.35±0.04 which is comparable to the values measured by Sá et al. (SV = 0.33±0.11) with free breathing oxygen-enhanced ^{1}H MRI [25]. The histograms of r (VH) shown in Figure 5.4 from the 2D fractional ventilation maps display the same shape with the exception of Volunteer 4. The histogram suggests a bimodal distribution of fractional ventilation in the right lung reflecting the VH in two different lobes presumably, while the histogram shape in the left lung is similar in all volunteers.

The mean values from the 3D acquisitions from all volunteers were similar (average r = 0.25±0.08) to those derived from 2D protocol in the same volunteer, but ranged between r=0.16-0.48. The fractional ventilation values scale with breathing volume and inhalation level. Due to the timing of the 3D data acquisition, some volunteers (compare Volunteer 4) found it harder to breathe in a calm fashion. The longer 3D sequence duration increases the apnoea during the first breath-hold, which in turn can result in an altered subsequent breathing pattern in some cases with increased *TV* (Figure 5.8, volunteer 4). This might explain the bigger variability in mean fractional ventilation in the 3D protocol. While volunteers re-establish steady tidal breathing during the 2D washout after apnoea this was not possible during a 3D washout, where only four to five acquisitions with sufficient SNR could be acquired and longer image acquisitions considerably interrupt the breathing pattern. Acquisition acceleration techniques like compressed sensing (CS) [6] and k-t-BLAST [175] may help to decrease 3D acquisition times and the number of RF pulses needed to acquire the 3D images, so that a timing similar to the one in 2D might be achievable. Using the recorded *TV* in both experiments and with the assumption that *FRC* (the initial volume before breathing in the hyperpolarised gas) is highly reproducible, the values acquired with the 2D protocol can be converted into whole lung fractional ventilation values (Table 5.2). Comparison of mean whole-lung fractional ventilation from 3D image acquisition does not significantly correlate with mean fractional ventilation from 2D slices (scaled by the difference

in TV).This might indicate that two sagittal slices do not represent the heterogeneity from the whole lung as previously suggested by Sá et al [176].

5.4.1. Repeatability

The pixel by pixel comparisons of the fractional ventilation maps from repeated experiments (Figure 5.9A and B) show significant correlations and confirm the reliability of both protocols in the tested volunteer. Table 5.3 shows the strong correlations of all tested 3D datasets when compared across 8 similar regions in the lung. Even a voxel-by-voxel comparison shows highly significant Pearson's correlations greater than 0.5.

5.4.2. Gravitational evaluation of fractional ventilation

The well-known A-P ventilation gradient in supine humans, which is usually attributed to gravity and the spring-like compression of the lung under the weight of the overlying mediastinum [25, 65, 173], is clearly demonstrated in this work and helps confirm the validity of the method. The comparison of 2D and 3D gravitational effects shows good agreement of the gravitational effect. This leads to the assumption as used by Sá et al. [176], that a single sagittal slice could be representative for VH distributed in the whole lung in healthy volunteers. In the presence of lung disease VH is not only a function of the gravitational difference in ventilation from anterior to posterior parts of the lung, but from inhomogeneous gas distribution related to disease patho-physiology.

5.4.3. Conclusion

The results presented here demonstrate that it is feasible to obtain quantitative fractional ventilation maps by MR measurements of ^{3}He washout with only a single dose of hyperpolarised ^{3}He. This reduces the amount of hyperpolarised ^{3}He necessary for this type of examination considerably when compared to previously suggested methods based on ^{3}He washin [168, 169]. The washout approach presented here enables ^{3}He MRI ventilation quantification for studies in humans breathing voluntarily using ~100 mℓ doses of ^{3}He for a 2D washout with two slices. This compares favourably to 2ℓ of ^{3}He used to acquire a 2D fractional ventilation map in a mechanically-ventilated pig used as a prelude to human experiments with the equivalent washin technique [169]. The feasibility of acquiring a fractional ventilation map of the whole lung using 200 mℓ of ^{3}He was shown using the 3D washout protocol. Additionally, the total duration of the examination is less than a half a minute, making it practical for routine clinical application. Reproducibility of the technique was shown.

The 2D washout imaging protocol caused subjects to deviate less from a relaxed breathing pattern than the 3D protocol. Tidal volumes approximately matched those measured at rest in a supine position outside the scanner. This could be an advantage when trying to measure fractional ventilation under different physiological conditions. As an example this could be used to investigate linearity of values of fractional ventilation when subjects breathe at different tidal volumes. It would also be an advantage for studies on patients with severely impeded lung function, as it requires only a synchronisation of the breathing cycle with the acquisition protocol. For patients who are able to hold their breath for longer than 10s, the 3D voluntary breathing protocol was shown to be capable of producing fractional ventilation maps of the whole lung. In Chapter 8 it is shown that this requirement can be met by patients with a predicted FEV1 of 30%. After some training even a 6 year old child was tested successfully with this technique. Furthermore, in particular for patients in the presence of ventilation heterogeneity full lung coverage is of advantage to probe the whole lung rather than a single slice.

Chapter 6 Error analysis of fractional ventilation from MBW-imaging

6.1. Introduction

In the previous chapter measurement of regional fractional ventilation as a metric of gas turnover was introduced using hyperpolarised ^{3}He MBW-imaging. Agreement with an independent measure of gas turnover was shown and the gravitational gradient in lung ventilation described in literature previously was observed [25, 65, 163, 173, 174]. The feasibility of the technique in 2D and 3D was then tested.

In this chapter measurement errors influencing fractional ventilation derived from MBW-imaging are systematically investigated. The calculation of fractional ventilation from image intensity decay is described in Chapter 5. The signal intensity decay, to be fitted to obtain regional fractional ventilation can be described as follows:

$$I(n) = (1-r)^{n-1} \cdot C^{-1} \cdot S(1) \qquad \text{Eq. [6.1]}$$

where r is the regional fractional ventilation. C the correction factor calculated from non-washout related signal decay and $S(1)$ the signal intensity in the first image before the gas washout has started. Therefore the error in $I(n)$ can be broken down as:

$$\delta I^2 = \left(\frac{\partial I}{\partial r} \cdot \delta r\right)^2 + \left(\frac{\partial I}{\partial C} \cdot \delta C\right)^2 + \left(\frac{\partial I}{\partial S} \cdot \delta S\right)^2 \qquad \text{Eq. [6.2]}$$

where the random error δI of the intensity decay represents the combination of effects from variation in tidal volume from breathing (δr), errors in the correction factor (δC) and due to noise in the measured signal (δS). In the following analysis relative errors are denoted with a Δ and expressed in percent. First the individual errors influencing $I(n)$ are investigated alongside their influence on fractional ventilation. Then the combined error in $I(n)$ is used as an input to a Monte-Carlo analysis to determine the combined effect of all errors on r.

6.2. Errors derived from volume changes

During MBW-imaging subjects breathe voluntarily and have to synchronise breathing with the imaging sequence. The disadvantage of synchronised breathing is that the tidal volume (TV) as well as the lung volume during breath-hold (LV) can alter considerably from breath to breath. This is especially the case for the first image following the calibration phase of apnoea, which is

likely to be at higher *LV* than the first two images. These changes in *TV* and *LV* will directly scale mean values of fractional ventilation accordingly (Section 5.2.10):

$$\bar{r} = \frac{TV}{LV} \qquad \text{Eq. [6.3]}$$

Figure 6.1 shows a volume curve as recorded during washout imaging. Errors resulting from irregular breathing are schematically shown. Pneumotachograph recording and segmented lung volumes from 3D washout images during washout in healthy volunteers (Table 5.1) were used to evaluate volumes and the corresponding standard deviations δTV and δLV. Those standard deviation are subject-specific and derive from intra-experimental changes of tidal volume and lung volume (see Table 6.1).

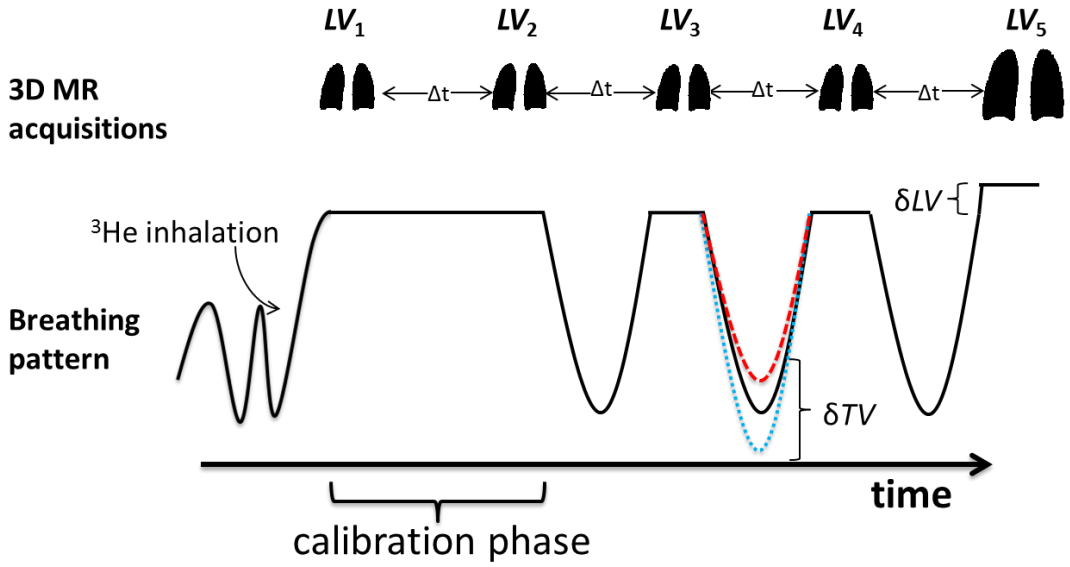

Figure 6.1: Schematic of a multiple breath washout imaging protocol showing the volume curve during MBW-imaging experiment as measured with a pneumotachograph. Above the curve a segmented coronal slice is shown to visualise the volume change. The deviations of lung volume and tidal volume are schematically shown in the volume curve.

Error propagation was used to investigate the influence of deviations in both tidal and lung volume on the estimate of fractional ventilation.

$$\delta \bar{r} = \sqrt{\left(\frac{\delta TV}{TV}\right)^2 + \left(\frac{\delta LV}{LV}\right)^2} \cdot \bar{r} \qquad \text{Eq. [6.4]}$$

Where $\bar{r}$ is the mean global fractional ventilation as derived from *TV* and *LV*. $\delta\bar{r}$ is the associated error in fractional ventilation due to volume changes during the experiment.

Results

Lung volumes (*LV*) were obtained from volumetric images of the 3D MBW-imaging protocol from 7 subjects. It should be noted that the SNR is not expected to influence the outcome *LV* measurements, since images with an SNR<10 were excluded from evaluation. Table 6.1 gives an overview of the resulting volumes, the standard deviations thereof and the resulting error in global fractional ventilation evaluating Eq. [6.4].

Subject	*LV*	*δLV*	*TV*	*δTV*	$\bar{r}\pm\delta\bar{r}$	*Δr* (in %)
Volunteer 1	5320	252	1350	252	0.25±0.05	20.7
Volunteer 2	4490	269	745	139	0.17±0.03	19.6
Volunteer 3	3044	209	680	161	0.22±0.06	24.7
Volunteer 4	4626	204	-	-	-	-
Volunteer 5	4931	306	590	102	0.12±0.02	18.4
Volunteer 6	4545	479	914	110	0.20±0.03	16.0
Volunteer 7	4557	188	594	79	0.13±0.02	13.9
Mean	4502±655	272±93	812±264	141±56	0.18±0.04	18.9±3.44

Table 6.1: Overview average end inspiratory lung volumes (LV) and standard deviation as obtained from segmenting 3D image-volumes. Tidal volume (TV) and its standard deviation were measured using a pneumotachograph during gas-washout. Resulting global fractional ventilation ($\bar{r}\pm\delta\bar{r}$) and relative error (Δr) were calculated using Eq. [6.4]. All volumes are in ml.

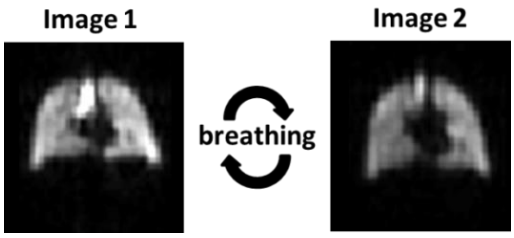

Figure 6.2: Demonstration of the effects of lung volume change in an example from a young CF patient. Total volume difference from segmented 3D volumes in this example was found to be 0.5L. The same intensity window was applied to both images.

Discussion

The relative error of fractional ventilation related to changes in lung volumes was evaluated to be less than 19±3% on average and was found to be 25% in the worst case scenario. It is assumed that the relative error Δr deriving from lung volume changes during MBW-imaging is influencing all values of fractional ventilation equally. Linear scaling of regional fractional ventilation with global volume changes has been evaluated in the literature [177, 178] and was previously applied in a similar method using fractional ventilation from oxygen enhanced imaging [176].

6.3. Errors associated with the signal correction factor

The correction factor to compensate for non-washout related signal decay is derived from two images acquired during a calibration breath-hold (Eq. [5.3]) and is a function of T_1 and α:

$$C = e^{\frac{-t}{T_1}} \cdot (\cos\alpha)^{N_{RF}} \qquad \text{Eq. [6.5]}$$

Where the exponential describes the T_1 signal decay over a time t and the other term treats signal decay due to RF depolarisation with N_{RF} pulses. In the following the influence of changes in the delivered transmit flip angle due to different lung inspiration levels during each breath-hold and changes in T_1 due to changes in the gas mix during gas washout are discussed and investigated. In addition oxygen uptake by the blood is investigated in terms of influence on the outcome of fractional ventilation. The error is calculated based on values from literature [61, 179]. It should be noted, that in the presence of collateral ventilation the correction factor will also be masked by inter-pixel gas diffusion resulting in gas movement between compartments during breath-hold. Those effects are not taken into account in this error analysis.

The effect of RF flip angle α

Depending on the loading of the RF coil different power has to be applied to accomplish a given flip angle in a given subject. The flip angle changes within a small margin for different inflation levels with the coil design used and at 1.5T [180]. Lung volumes change less than ±11% (Table 6.1). Assuming isotropic expansion of each voxel in the lung this means a change of 2.2% in each direction. The error in flip angle due to this change of inspirational level is therefore considered as negligible in this error evaluation [180].

The effect of T_1

Eq. [5.2] modelling the polarisation decay during the washout experiment assumes a constant T_1 throughout the experiment. With inhalation of the anoxic hyperpolarised ^{3}He –N_2 gas mixture a slightly lower oxygen concentration in the lungs will be found than after breathing air as in the following breaths. In addition oxygen in the lungs is taken-up by blood during the calibration breath-hold contributing to a further slight drop of partial oxygen pressure in the lung. This results in an associated increase of the T_1 of hyperpolarised ^{3}He (Section 2.4.8) [40]. A schematic of the T_1 trend during the course of a washout experiment is shown in Figure 6.3.

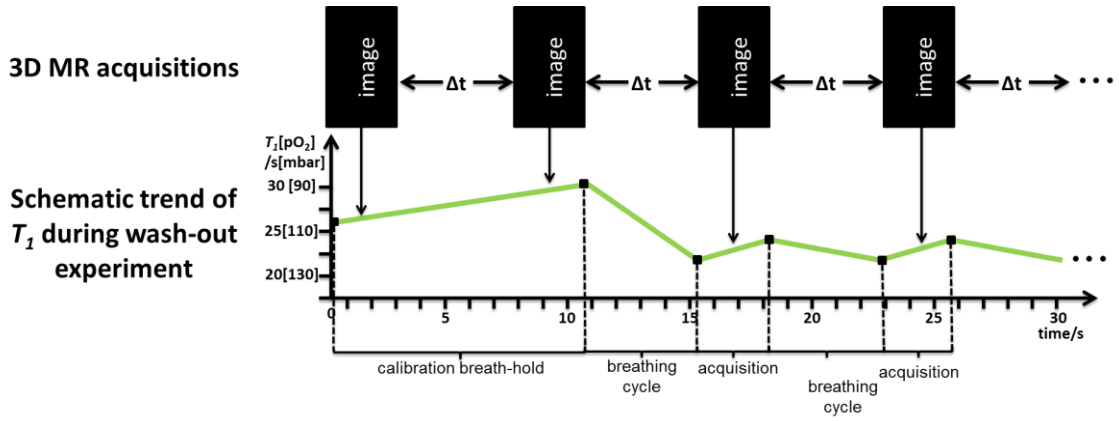

Figure 6.3: Illustrative schematic showing variation of T_1 of the hyperpolarised ^{3}He in the lung during a washout experiment. Due to inhalation of an anoxic gas mix the T_1 can be expected to be higher than during the washout and increases during calibration breath-hold while more oxygen is taken up by the blood. With beginning of the gas washout after the first breathing cycle the oxygen level returns to normal reducing T_1. During every breath-hold T_1 will slightly increase again due to oxygen uptake.

To estimate the error introduced in the correction factor from overestimating T_1, values from the literature were used. Typical values of pulmonary alveolar pressure are around 133mbar [65] in healthy lungs. This is in agreement with regional measurements of pO_2 from hyperpolarised gas MRI [61, 179] and from multiple inert gas elimination technique (MIGET) [181]. By introducing a 1000*ml* volume of anoxic gas mixture the partial oxygen pressure drops as follows:

$$pO2_{anoxic} = pO2_{normal} \cdot \frac{LV - 1000ml}{LV} \qquad \text{Eq. [6.6]}$$

where $pO2_{annoxic}$ is the partial oxygen pressure after inhalation of the mix of nitrogen and hyperpolarised ^{3}He, $pO2_{normal}$ is the partial oxygen pressure under normal breathing conditions. The ratio at the end is the mean global fractional ventilation, with *LV* being the total lung volume, 1000*ml* the volume of the gas inhaled from the Tedlar bag at the beginning of the experiment,

describing the relative amount of residual gas in the lung. This assumes equilibrium mixing of the resident gases in the lung a valid assumption in healthy subjects in absence of delayed ventilation. The lung volumes, as in the previous section on volume related errors, are derived from the volunteer datasets in Chapter 5. This allows an evaluation of the changes in T_1 derived from inhaling an anoxic gas mixture.

In addition to the change of apparent gas mix in the lung, the uptake of oxygen by the blood has an influence on T_1. To evaluate oxygen uptake a linear model is used [61, 63]:

$$pO2_{end} = pO2_{init} - R \cdot t \qquad \text{Eq. [6.7]}$$

where $pO2_{init}$ is the initial partial oxygen concentration upon inhalation, R is the rate at which this concentration decays over the time t. The initial partial oxygen pressure ($pO2_{init}$) is equal to $pO2_{annoxic}$ and for R a value of 2mbar/s was taken from literature [61, 179]. t is the period of apnoea during the calibration acquisitions which is equal to the duration of the acquisition (~2·2.2s) plus the gap between the images (4s) acquired during calibration breath-hold and adds up to 8.4s. $pO2_{end}$ therefore is the partial oxygen concentration at the end of the calibration breath-hold.

$$T_1' = \xi \cdot \left[\frac{1}{\left(pO2_{normal} \cdot \frac{LV - 1000}{LV} \right) - R \cdot t} \right] \qquad \text{Eq. [6.8]}$$

where T_1' is the T_1 after the combined effects of inhaling anoxic gas and oxygen uptake are both factored in and ξ = 2.61 bar·s [61]. The results for subjects are summarised in Table 6.2.

Subject	$\frac{LV - 1000ml}{LV}$	pO2 /[mbar] during normal breathing ($pO2_{normal}$)	$pO2_{anoxic}$ /[mbar] (after inhalation of anoxic gas)	$T1_{anoxic}$ /[s] (result of inhaling anoxic gas)	R (decay rate of oxygen)	$pO2_{O2\text{-}uptake}$ /[mbar] (result of oxygen uptake)	T1'/[s]
Volunteer1	0.19	134±15 mbar*	109	24	2±0.86 mbar/s*	92	29
Volunteer2	0.22		104	25		87	30
Volunteer3	0.33		90	29		73	36
Volunteer4	-		-	-		-	-
volunteer5	0.20		107	25		90	29
Volunteer 6	0.22		104	25		88	30
Volunteer 7	0.22		104	25		88	30
Mean±SD	0.23±0.05		103±6	26±2		86±6	31±2

*Table 6.2: Overview of the parameters used in estimating T_1'. Standard deviation of mean values derive from inter-volunteer variations. * value from literature [61, 179];*

The systematic error ΔC_{sys} is calculated by substituting T_1' plugged into Eq. [6.5]:

$$\Delta C_{sys} = \frac{C - e^{\frac{-t}{T_1'}} \cdot (\cos\alpha)^{N_{RF}}}{C} \cdot 100\% \qquad \text{Eq. [6.9]}$$

In addition to the systematic overestimation of T_1 the variation of T_1' is taken into account as relative error ($\delta T_1'$, Table 6.2 as the variation between volunteers). The random error in C is derived as follows:

$$\delta\, C(T_1') = \sqrt{\left(\frac{\partial C}{\partial (T_1')}\delta\, T_1'\right)^2} = \\ = \sqrt{\left(e^{\frac{-t}{T_1'}} \cdot \cos(\alpha) \cdot \left(\frac{-t}{(T_1')^2}\right)\delta\, T_1'\right)^2} = C \cdot \sqrt{\left(\frac{t}{(T_1')^2} \cdot \delta\, T_1'\right)^2} \qquad \text{Eq. [6.10]}$$

With sequence parameters as shown in Chapter 5 (α=1°, acquisition matrix: 32^2) the error in C was calculated.

From the systematic error ΔC_{sys} due to T_1 overestimation, the systematic error in fractional ventilation r can be calculated as follows:

$$\Delta r_{sys} = \frac{r - \left[r \cdot \Delta C_{sys}\right]}{r} \cdot 100\% \qquad \text{Eq. [6.11]}$$

The erroneous correction factor results in a deviation of the true slope that linearly changes fractional ventilation r. The random error in r is calculated similarly from error propagation:

$$\delta\, r = \sqrt{\left(\frac{\partial r}{\partial C}\delta\, C\right)^2} = \sqrt{\left(r \cdot \left(-\frac{\delta\, C}{C}\right)\right)^2} \qquad \text{Eq. [6.12]}$$

This means that the random error found in C is equal to the random error in fractional ventilation r (under the assumption that the error deriving from flip angle variations was neglected).

Results:

The resulting systematic error in the correction factor for typical values of T_1 in healthy lung are shown in Figure 6.4 including $\delta T_1'$ as the inter-volunteer variability. The systematic error of the correction factor C_{err} ranges from approximately 10% to 18% for higher values of T_1.

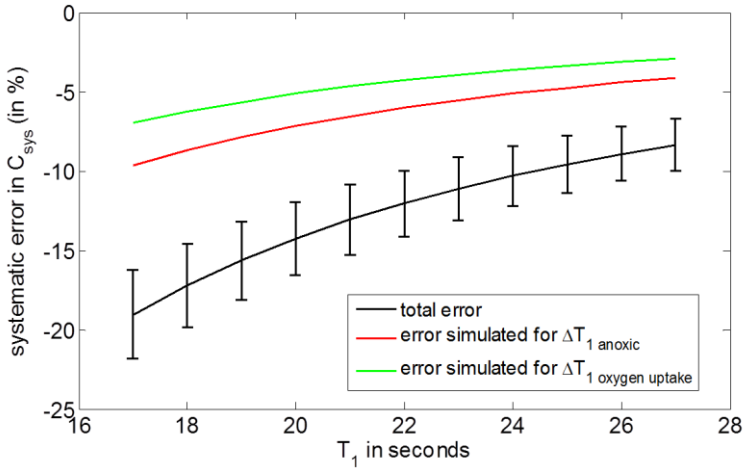

Figure 6.4: Systematic error in correction factor C_{sys} for different values of T_1. Error bars obtained from variations between volunteers (referred to as random error). The green line represents the error from changes in T_1 from oxygen uptake during the breath-hold. The red line is derived from errors changes in T_1 resulting from changes of the gas mix in the lung. The total error in the correction factor plotted as a black line results from T_1' in Eq. [6.8].

Figure 6.5 shows an overview of relative error in *r* depending on differences in the starting partial oxygen pressure before inhalation of the gas mix present in the lung.

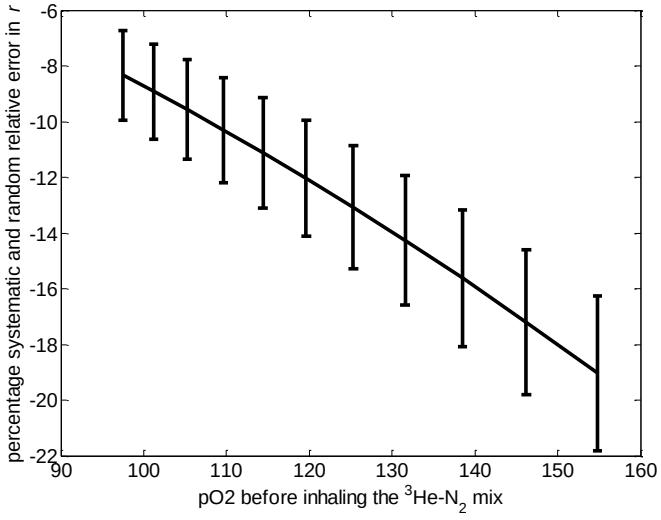

Figure 6.5: Systematic error in fractional ventilation (Δr_{sys}) for different values of starting alveolar pO_2 from literature [61, 179, 182]. The systematic error in the correction factor is plotted as black line with the random error (from physiological differences) as error bars. The relative error is constant across values of fractional ventilation.

Discussion

In summary, errors in fractional ventilation range between 7 and 22% depending on T_1 (Figure 6.5) and are expected to be constant for different values of fractional ventilation in healthy volunteers. This assumption might not apply for lungs with a very uneven distribution of gas upon inhalation of the gas mix containing the hyperpolarised ^{3}He, where spatial T_1 mapping might be required to estimate the effect of spatial heterogeneity.

6.4. Influence of SNR on fractional ventilation

In MRI the measured complex raw signal is influenced by Gaussian noise when Fourier transformed and presented as magnitude images, the distribution is well represented by a Gaussian if SNR>2 (SNR in images used here >10) [183, 184]. To simulate the effect of random noise on the estimate of fractional ventilation a Monte Carlo simulation was performed. Typical SNR values were taken from the images from the volunteer study of the previous chapter using a fixed amount of 200ml ^{3}He for each washout and are summarised in Table 6.3. The SNR was calculated as the ratio of mean signal from the segmented lung to the standard deviation of the noise.

Subject	SNR(1)	SNR(2)	SNR(3)	SNR(4)	SNR(5)	SNR(6)
Volunteer 1	85	57	21	10	<3	<3
Volunteer 2	111	79	66	48	26	16
Volunteer 3	85	81	71	53	26	14
Volunteer 4	109	78	30	8	3	4
Volunteer 5	58	53	44	33	19	14
Volunteer 6	80	75	66	39	23	11
Volunteer 7	70	66	60	38	28	17

Table 6.3: Average SNR in each image of the washout acquisition for volunteers from Chapter 5.

Noise levels were obtained from the first slices in the absence of signal and the additive standard deviation of the noise in regions with signal is calculated [183]:

$$\sigma^2 = \sigma_m^2 \cdot (2 - \frac{\pi}{2})^{-1} \qquad \text{Eq. [6.13]}$$

Where σ is the noise in the presence of signal, and σ_m the standard deviation of the noise measured in the absence of signal. The noise is a random error in the signal term *S(1)* in Eq. [6.1] with δS being equal to σ. With knowledge of the SNR as the ratio of mean signal to the standard deviation of the noise, for the measured levels of SNR, $\delta S = 1.53\sigma_m$.

The influence of this noise level on the least square fitting routine used to calculate fractional ventilation is investigated by using a Monte Carlo simulation. As an input to the simulation the dataset of Volunteer 1 (with the highest inspiratory lung volume *LV*) was used: signal value measured in the first image at $S(0)$ ($=I(1)$) and the noise level (constant during the whole washout imaging). For given fractional ventilation Eq. [6.1] can be used to determine the error.

The error was empirically determined by addition of a Gaussian-noise distribution to each point on the washout curve as schematically shown in Figure 6.6. A total of 10,000 signal decays were generated and from these a range of fractional ventilation r = [0.1 , 0.8] were fitted. To understand how the fitting routine influences the error in *r* estimation, a different number of points from the decay were included in the fitting procedure (2 points, 3 point, 4 points and 5 points).

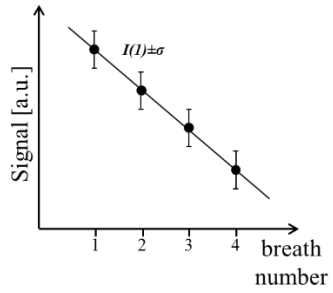

Figure 6.6: Signal decay for a specific fractional ventilation (given as input to the code). I (=signal due to gas washout) was added with noise (σ) according to a Gaussian probability distribution as shown next to the points on the curve.

Results

The simulation of influence of noise on the fitting routine was performed using the dataset from volunteer 1 with a high lung volume using 200ml of hyperpolarised ^{3}He. The error in the signal intensity increases with lower SNR levels.

Figure 6.7 shows how different values of fractional ventilation are influenced by the fitting routine. Fractional ventilation values of $r = 0.1$ and $r = 0.8$ were investigated using a 3-point and a 2-point fit. A 2 point fit results in a small error for a high fractional ventilation of 2%, but the relative error for a lower fractional ventilation with 19% is considerably higher. The relative error decreases to 10% for $r = 0.1$ and further decreases when including more points. For high fractional ventilation ($r > 0.6$) increasing the number of points also increases the error. A complete overview is given in Figure 6.7. The figure is a result of Monte-Carlo simulations of a range of fractional ventilation values r = [0.1 , 0.8] including a different number of images in the fit. In addition an

approximate SNR was calculated by taking into account signal decay as measured from the correction factor and washout.

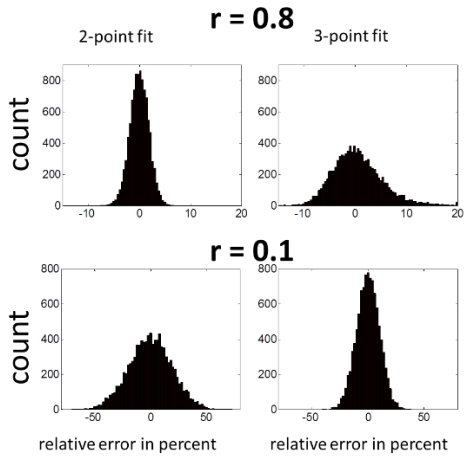

Figure 6.7: Distribution of errors across all 10,000 simulations resulting from noise in images. An initial SNR of 86 was assumed in the first image (value taken from Volunteer 1 with biggest lung volume). 10,000 values were simulated for two different fractional ventilations r = 0.8 and r = 0.1. For a very rapid signal decay (r = 0.8, high turn-over of gas) the relative error in r was found to be 7%.

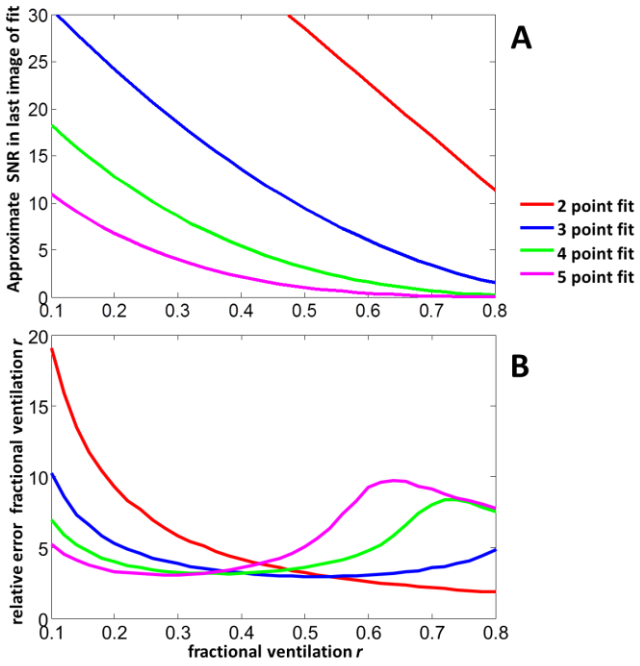

Figure 6.8: (A) shows the estimated SNR of the last image used to fit fractional ventilation. (B) shows the resulting relative error of the fitting routine. The simulation is based on dataset of volunteer 1 and assumes an initial SNR = 57 in the image before the gas-washout (compare Table 3).

Discussion

Low values of fractional ventilation show a decrease of error when adding points to the fit. The reverse effect is observed at higher values of fractional ventilation. Including signal with low SNR into the fitting routine introduces additional error in the fit resulting in an increase of the total error. Low values of fractional ventilation representing slower washout of the hyperpolarised gas are not influenced by this, but values about $r = 0.5$ show an increasing error when adding points to the fit. A sudden decrease of relative error at higher fractional ventilation (e.g. 5 point fit for $r > 0.65$, Figure 6.9) is explained with the use of absolute signal intensity in the fitting routine. Therefore the absolute value of negative signal intensities resulting from noise being bigger than signal value is taken.

By increasing the dose applied during a washout experiment SNR could be increased throughout the washout. Nevertheless, gas amount should be scaled according to expected fractional ventilation. For higher average fractional ventilation ($r > 0.45$, Figure 6.9) more gas would be beneficial for the fitting routine resulting in an reduction of error when including 3 or more points to the fit. Nevertheless, the volunteer data all have a mean fractional ventilation of less than 0.35. Setting an SNR constraint of SNR>10 with a dose of 200ml ^{3}He in comparable or smaller lung volumes then 4 points result in the best fit. The error deriving from signal noise is then around 5%. Especially when imaging children with considerably smaller lungs (see Chapter 8) with doses comparable to those used with adults, the data could be fitted over up to 4 points, since the SNR curves (Figure 6.8A) will start at a higher level.

This assumes that the flip angle is kept constant and is not adjusted to the amount of images expected. The main aim is to acquire as many images as only possible and therefore the flip angle should be as small as possible, since data from bad breathing manoeuvres or due to too low SNR images might have to be excluded subsequently.

In future work it would be beneficial for the reliability of the data to not set a fixed SNR threshold in combination with a fit over a fixed number of points, but to adjust both depending on the actually measured regional SNR and signal decay (fractional ventilation).

6.5. Total combined error analysis

As a last step, the total error deriving from the combination of errors in SNR, T_1, and volume changes is calculated. When solving Eq. [6.2] with all errors taken into account in this analysis, the following equation describes the propagating errors in $I(n)$:

$$\delta I(n) = \sqrt{\left(\frac{\delta \bar{r}}{(1-r)} \cdot (n-1)\right)^2 + \left(-\frac{\delta C}{C}\right)^2 + \left(\frac{\delta S}{S(n)}\right)^2} \cdot I(n) \qquad \text{Eq. [6.14]}$$

The first term of the equation under the square root describes the error deriving from volume changes ($\delta\bar{r}$), which is thought to be constant over all values of fractional ventilation *r*. The second term accounts for the errors from variation in the correction factor and the last term represents the error deriving from image noise.

The individual errors are obtained from the sections above. For $\delta\bar{r}$ the error resulting from volume changes is used and therefore the volume related error is a function of the fractional ventilation. It is assumed that this volume change influences the range of fractional ventilation found in the healthy volunteers in the same way. The correction factor is independent of fractional ventilation and an average random error of 3% was used as established in the section above. In addition, the systematic error deriving from the correction factor is considered and directly scales values of fractional ventilation as shown in the section above. The signal intensity is a function of the breath number with an error increasing in each breath (due to constant noise level and a decrease of signal intensity measured). The total error including least squares fitting is investigated using Monte-Carlo simulation of Eq. [5.7]. As input to this equation the corrected intensity decay and the calculated associated error distribution $I(n)\pm\delta I(n)$ were used.

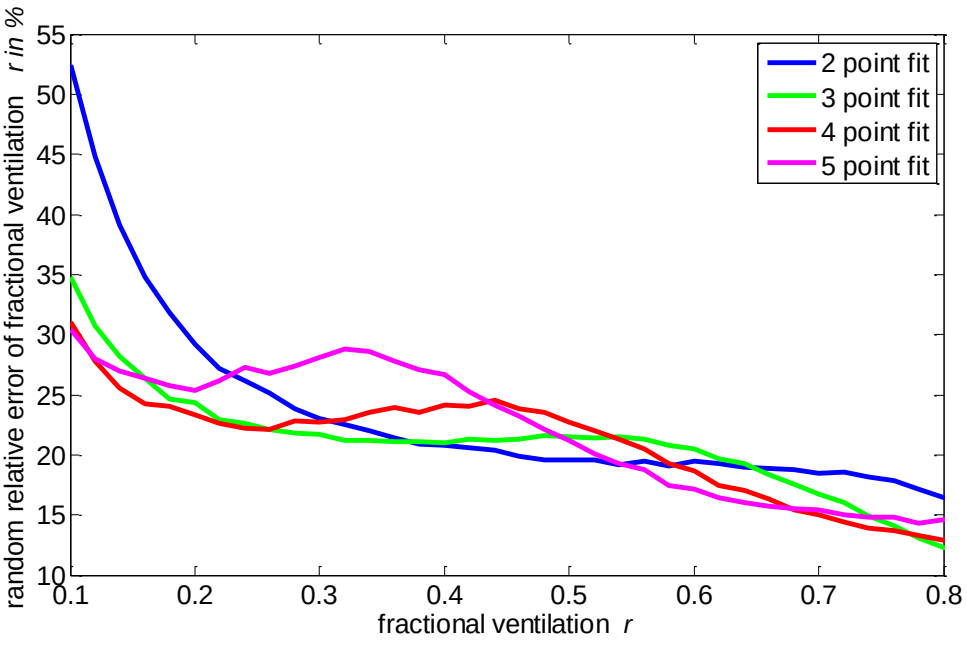

Figure 6.9: Total error simulated in a Monte-Carlo analysis. Each data point consists of 10.000 experiments.

Results

Figure 6.9 shows the result of the Monte Carlo simulation. The relative error decreases for higher values of fractional ventilation. The worst case scenario of a two point fit at low fractional ventilation results in a relative error Δr <55%. In addition, to random errors the systematic error deriving from the correction factor between 7-22% (Figure 6.5) has to be added to the values found in Figure 6.9. This systematic error derives from the overestimation of T_1 due to the length of the calibration breath-hold and the changed gas mix present in the lung. Due to different lung volumes (resulting in different gas mixe from volunteer to volunteer) and different initial inflation states it is hard to predict the contribution of this systematic error exactly for this analysis. For a fractional ventilation r = 0.01 this means the associated error is Δr=0.0014±0.0055 in the case of regions with high gas turnover r = 0.8 the associated error is Δr=0.11±0.16.

Discussion

Taking all investigated random errors into account at mean fractional ventilation of r = 0.2-0.4 a bias error of ~15% due to T_1 overestimation can be expected. The random error deriving due to breathing manoeuvres and different lung physiology in the volunteer cohort was estimated to be around ±25% for this range of fractional ventilation.

6.6. Conclusions

The impact of breathing pattern, changes of T_1 due to changes in gas mix and the influence of SNR on the fitting routing were found to be as the most important sources of error on fractional ventilation from MBW-imaging. It is assumed that changes in B_1 field due to different inspirational lung volumes are negligible [180]. Furthermore introduced by image registration are not discussed in this context. Image registration is used to align the lungs after each breathing cycle. Especially non-physiological values around the diaphragm are avoided this way, since the exact position of the diaphragm is hard to reproduce. The currently used algorithm developed by Barber et al. seems to be well suited for the purpose and no physiological unrealistic values around the edges of the lungs are found.

Chapter 7 Advances in multiple breath washout imaging acquisition methods

7.1. Introduction

In chapter 5 multiple breath washout imaging (MBW-imaging) with hyperpolarised ^{3}He was introduced as a method to derive quantitative parametric maps of fractional ventilation. A protocol was presented for image acquisition that uses a spoiled gradient echo (SPGR) sequence. To enable acquisition of multiple images interrupted by breathing, low flip angles were employed which resulted in acceptable image quality despite signal losses from gas washout and polarisation decay during the experiment. However, a more efficient use of polarisation in hyperpolarised gas lung MRI can be achieved through the use of balanced steady state (bSSFP) sequences [4]. Instead of dephasing the residual transverse magnetisation at the end of each repetition with spoiler gradients, the magnetisation is refocused by balancing all gradients with their mirrored counterpart. As a result, higher SNR can be obtained with bSSFP versus SPGR through the use of higher flip angles. In this chapter a 3D bSSFP sequence for ^{3}He MBW-imaging is compared against the 3D SPGR sequence presented in Chapter 5. The hyperpolarised ^{3}He dosage was halved (100ml) with the bSSFP sequence whilst maintaining the same spatial resolution (~1cm^{3}) as with the SPGR sequence.

With this acquisition strategy the feasibility of performing MBW-imaging with hyperpolarised ^{129}Xe as an alternative to ^{3}He was also investigated. Initial findings from 2D MBW-I with ^{129}Xe have been presented at ISMRM [174]. However, 3D MBW-imaging using hyperpolarised ^{129}Xe remains a challenging task since its Larmor frequency is lower than that of ^{3}He by a factor of 2.75. Due to its considerably lower price at natural abundance (£20/litre) when compared to more than £500/l for ^{3}He alongside its wider availability than ^{3}He [29], ^{129}Xe imaging is clinically relevant. With advances in laser technology, current polariser systems are capable of producing very high polarisation ^{129}Xe polarisation [7, 34], the chemical properties of xenon have permitted new possibilities for studying gas exchange in the lung [67, 185]. Furthermore, higher polarisation levels and efficient utilisation of finite polarisation with bSSFP should allow sufficient SNR to be achieved using hyperpolarised ^{129}Xe for MBW-imaging. Therefore, in this chapter the feasibility of 3D MBW-imaging using hyperpolarised ^{129}Xe is also investigated in a preliminary study on healthy volunteers.

7.2. Methods

Subjects

A total of 7 healthy subjects between 23 and 38 years old and with an FEV1 in the range of 82-126% predicted were scanned under written informed consent and agreement of the local ethical committee. The volunteer details are listed in Table 7.1.

Subject	Sex	Age, years	Weight, kg	FEV1, (% predicted)*
Volunteer1	F	32	61	116
Volunteer2	M	23	77	108
Volunteer3	M	30	75	82
Volunteer4	M	28	84	108
Volunteer5	M	27	79	108
Volunteer6	F	38	80	126
Volunteer7	M	28	75	98

Table 7.1: Overview of the healthy volunteers imaged using SPGR and bSSFP MBW-imaging.* predicted values calculated according to [71].

Sequence parameters

Parameters for the 3D SPGR sequence were described in Chapter 5. For the 3D bSSFP sequence the following imaging parameters were used: matrix size of 32x32 (1.2cm x 1.2cm) and between 20-26 phase encoding steps covering the lung in the anterior-posterior direction at a partition thickness of 10mm, TR/TE 1.6/0.6ms; a receiver bandwidth = 166kHz and flip angle = 14°. The flip angle is lower than the optimum for the same 3D bSSFP ventilation imaging sequence as washout is monitored over multiple phases and polarisation needs to be preserved to monitor the washout. The gas dosage was 100ml of ^{3}He (25% polarisation) and was topped up with 900ml N_2. The MBW-imaging protocol was performed as described in Chapter 5 using the same transmit-receive coil tuned to 48.62 Mhz. With TR = 1.6 ms a single volumetric acquisition of the bSSFP sequence takes 1.9s, which is about 25% shorter than in the case of the SPGR sequence (2.6s).

^{129}Xe MBW-imaging

The same 3D bSSFP sequence was optimised for hyperpolarised ^{129}Xe MBW-imaging, with the following parameters: matrix size and slice thickness as above; TR/TE 2.9/0.9 ms, a receiver bandwidth = 16.1 kHz. The flip angle was chosen as 7° to ensure sufficient SNR over multiple acquisitions during MBW-imaging. A hard pulse was used resulting in a total acquisition time of 2.4s. A total of 600ml of enriched xenon topped up with 400ml N_2 was inhaled for imaging. The hyperpolarised ^{129}Xe had an approximate polarisation of approximately 40%. To directly compare bSSFP ^{129}Xe MBW-imaging with results from ^{3}He MBW-imaging, subjects were placed in a dual tuned coil (resonating at both 17.66Mhz, ^{129}Xe, and 48.62Mhz, ^{3}He) [186] so that no change in patient position was required between scans. Both gases were dispensed within 10 minutes and the breathing manoeuvres repeated for the repeated gas inhalations.

For a direct comparison, ^{3}He acquisitions were repeated using the same sequence with a hard pulse, resulting in shorter still TR/TE (1.4/0.4ms). The bandwidth was kept at 161kHz and the flip angle at 7°. Due to reduced coil sensitivity the ^{3}He dosage was increased to 200ml compared with the single-tuned T/R coil.

Post-processing

To calculate fractional ventilation maps from both ^{3}He and ^{129}Xe images the same procedure as described in the Methods of Chapter 5 were followed.

Comparison

To compare fractional ventilation values from different experiments, with different sequences (bSSFP versus SPGR) and ^{3}He versus ^{129}Xe, Pearson's correlation coefficient was calculated. In addition, a Bland-Altman analysis was performed and the mean difference and the standard deviation as percentage of the mean over all values were reported. This voxel-by-voxel analysis was valid because volunteers were not moved between experiments performed in the dual tuned RF coil. Therefore, inter-breath motion was assumed to be being the primary source of miss-registration. Depending on regional SNR (masks were created using image segmentation of the last image with mean SNR>10, see Chapter 5), parametric values could not be derived for all regions in the comparison. This resulted in the exclusion of some voxels from the comparison (see for example Figure 7.5).

As shown in Figure 5.10, parametric maps of fractional ventilation from the ^{3}He bSSFP-SPGR sequence comparison were manually divided into 8 regions of interest with similar size. The difference of mean values from each compartment between experiments was evaluated by calculating a Pearson's correlation coefficient.

7.3. Results

bSSFP and SPGR MBW-imaging with hyperpolarised ^{3}He

Hyperpolarised ^{3}He MBW-Imaging using a bSSFP sequence was successfully performed in all subjects. Example images acquired with an SPGR and SSFP sequences are shown in Figure 7.1. Resulting fractional ventilation maps from data in Figure 7.1 (Volunteer 6) are shown in Figure 7.2.

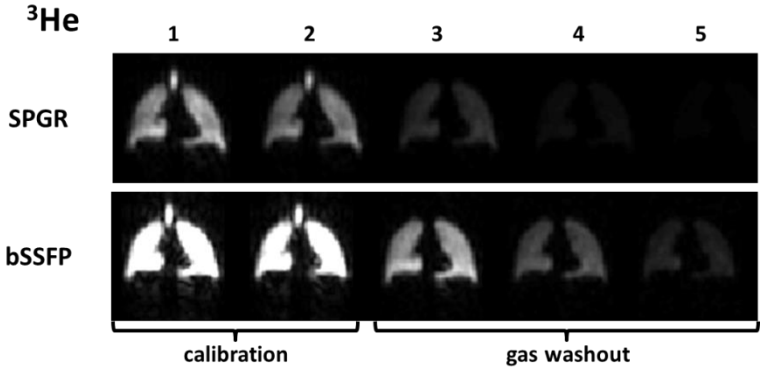

Figure 7.1: Comparison of image acquisition from the MBW-imaging protocol with SRGR and SSFP sequences in Volunteer 6. All images are presented in arbitrary units of image intensity with the same window level settings on each case.

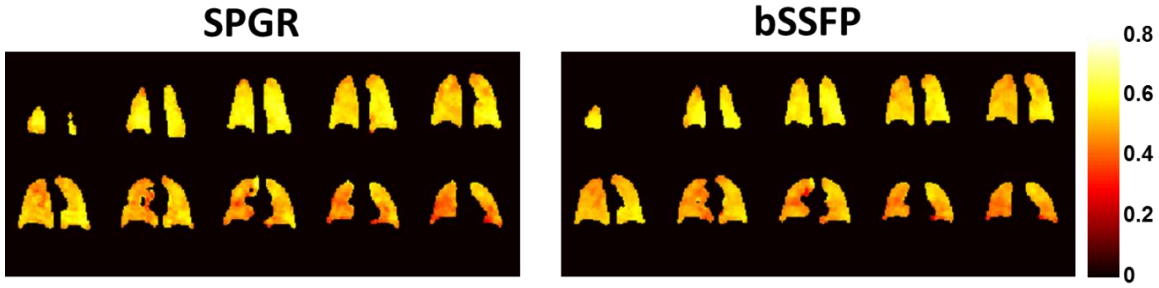

Figure 7.2: *Comparison of fractional ventilation maps derived from SPGR and bSSFP imaging acquired in the same session from Volunteer 6.*

SPGR derived fractional ventilation maps showed a good correlation with those derived from bSSFP, as summarised in Table 7.2. Volunteer 2 was also tested using an in-plane resolution of 64x64 and the same slice thickness as in other datasets (10mm) resulting in twice as many RF pulses as used in the other datasets. In this case, flip angle was reduced to 7° to account for the

extended number of RF pulses. Volunteers 6 and 7 were tested using 200ml of hyperpolarised ^{3}He and a flip angle of 7°.

Subject	Imaging sequence	Mean fractional ventilation *r*, mean (±standard deviation)	Voxel-by-voxel correlation coefficient of fractional ventilation, all P<0.001	Bland-Altman Analysis for voxel-by-voxel comparison) mean difference % (std. deviation %)	Correlation fractional ventilation (8-region comparison), all P<0.01	Volume turnover TV / LV†
Volunteer 1	SPGR	0.28(0.09)	0.58	30.1(38)	0.99	0.21
	bSSFP	0.24(0.11)				0.22
Volunteer 2	SPGR	0.33(0.10)	0.62	21.7(27)	0.95	0.20
	bSSFP**	0.28(0.11)				0.26
Volunteer 3	SPGR	0.25(0.09)	0.68	2.6(23)	0.96	0.21
	bSSFP	0.21(0.08)				0.18
Volunteer 4	SPGR	0.22(0.07)	0.73	3.9(23)	0.95	0.19
	bSSFP	0.22(0.08)				0.21
Volunteer 5	SPGR	0.19(0.09)	0.40	28.7(42)	0.85	0.13
	bSSFP	0.12(0.06)				0.11
Volunteer 6	SPGR	0.47(0.08)	0.56	7.6(19)	0.98	0.34
	bSSFP*	0.47(0.07)				0.35
Volunteer 7	SPGR	0.24(0.08)	0.67	11.6(21)	0.92	0.23
	bSSFP*	0.26(0.07)				0.22

Table 7.2: *Overview of results from voxel-by-voxel and 8 region comparisons. * 200ml ^{3}He, Flip angle = 7°. ** 200ml ^{3}He, Flip angle = 7°, in plane resolution: 64x64. †TV=tidal volume; LV = inspiratory lung volume.*

An example plot of voxel-by-voxel SPGR-bSSFP comparison from Volunteer 3 is shown in Figure 7.3 (Pearson's r = 0.68, P<0.001). A small mean difference of <3% and standard deviation of <25% were found from a voxel-wise Bland-Altman analysis on this dataset. For all datasets, the correlation coefficient r was greater than 0.4 and the average value was 0.61. The Bland-Altman analysis showed an average percentage mean difference between the SPGR and bSSFP experiments of 15.1%, with an average standard deviation of 27.5%.

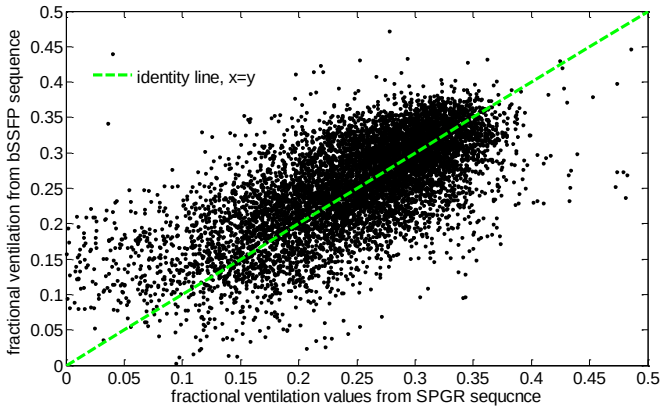

)

Figure 7.3: *Voxel-by-voxel comparison of fractional ventilation values derived from MBW-imaging using a SPGR sequence and a bSSFP sequence from Volunteer 3. Pearson's correlation coefficient r = 0.68, P<0.0001; Bland Altman analysis showed a mean difference between experiments of 2.6% with a standard deviation of 22.7%.*

The additional MR signal available on bSSFP imaging offers the possibility of improving spatial resolution whilst preserving image quality. In light of this, one dataset was acquired using an increased spatial resolution for bSSFP (64x64 in plane, Volunteer 2). The results of this scan are presented in Figure 7.4. Despite a small difference in average fractional ventilation values (0.34 (SPGR), 0.28 (SSFP)) both sequences showed similar features in the images. The standard deviation of fractional ventilation derived from both histograms was very similar with 0.10 (SPGR) and 0.10 (SSFP). Fractional ventilation maps derived from bSSFP imaging appeared slightly noisier than the lower resolution SPGR images (smoothed through zero filling to same resolution for comparison). A significant Pearson's correlation of r = 0.62 was found when comparing image maps on a voxel by voxel basis.

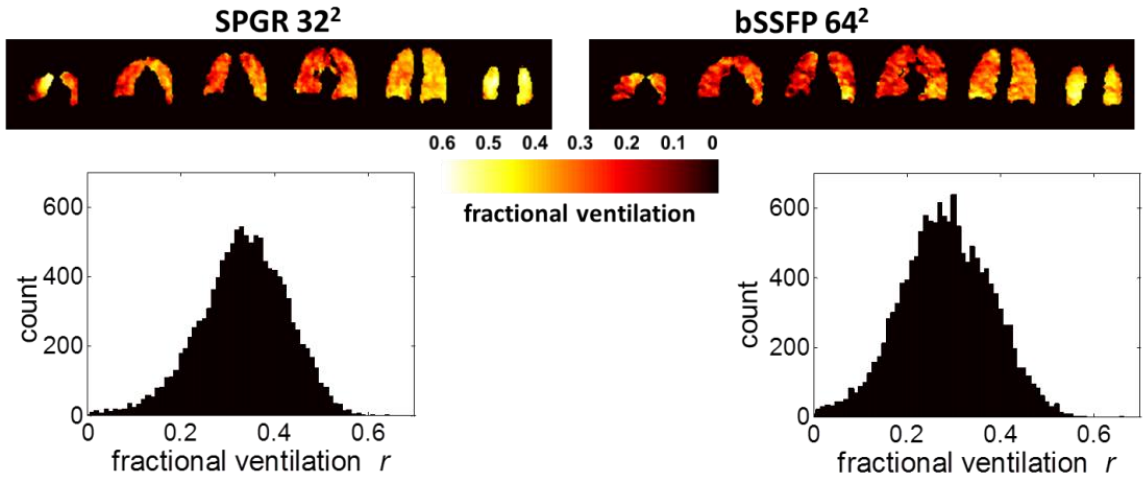

Figure 7.4: *Comparison of fractional ventilation maps derived from SPGR (32x32x26) and bSSFP (64x64x26) sequences from Volunteer 2. Fractional ventilation maps from slices (anterior to posterior) are shown along with whole lung fractional ventilation histograms. Slight differences in the in the colour intensity of the maps from each acquisition result from using the same colour map to represent the different average fractional ventilation values (SPGR average r = 0.34, SSFP average r = 0.28, compare also the peak of the histograms)*

MBW-imaging using ^{129}Xe

For all subjects (Subject 1-5, Table 7.1) on which MBW-imaging with hyperpolarised ^{129}Xe was performed, the image quality was sufficient to accurately post-process the data and produce fractional ventilation maps. Figure 7.5 shows the unprocessed results of MBW-imaging using ^{3}He and ^{129}Xe in Volunteer 3 windowed to enhance the contrast. An example of selected fractional ventilation maps derived from slices through the lungs of Volunteer 3 is shown in Figure 7.6. Similar values of fractional ventilation as well as a good agreement of features were found when

comparing ^{3}He and ^{129}Xe MBW-imaging data. The fractional ventilation histograms (Figure 7.7) are similarly shaped and display the same VH (ventilation heterogeneity i.e. the standard deviation of whole lung fractional ventilation maps). Volunteer 3, whose data is presented in Figure 7.5-Figure 7.7, exhibited the smallest value of mean differences of fractional ventilation between ^{3}He and ^{129}Xe of 2.9%, as calculated from Bland-Altman analysis. Results for all 5 volunteers are summarised in Table 7.3.

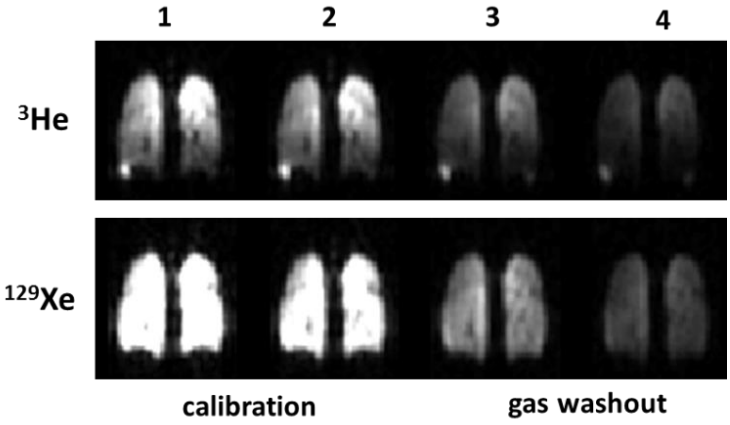

Figure 7.5: *Comparison of image acquisition from the MBW-imaging protocol with ^{3}He and ^{129}Xe in Volunteer 3. Reduced coil sensitivity at the bottom of the posterior slices when imaging with ^{3}He prevented calculation of fractional ventilation from those regions. All images are presented in arbitrary units of image intensity with the same window level settings in each case.*

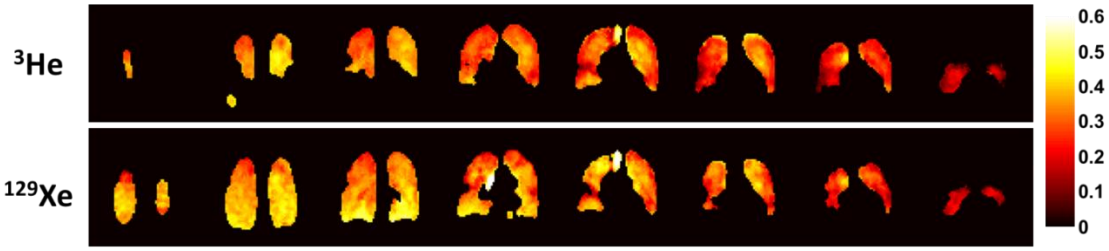

Figure 7.6: *Comparison of fractional ventilation maps from ^{3}He and ^{129}Xe MBW-imaging in Volunteer 3. The second slice of both fractional ventilation maps result from raw images shown in Figure 7.5. Every second slice from both 3D datasets is plotted, with posterior slices on the left and anterior in the right. The second slice is calculated from raw-images in Figure 7.5.*

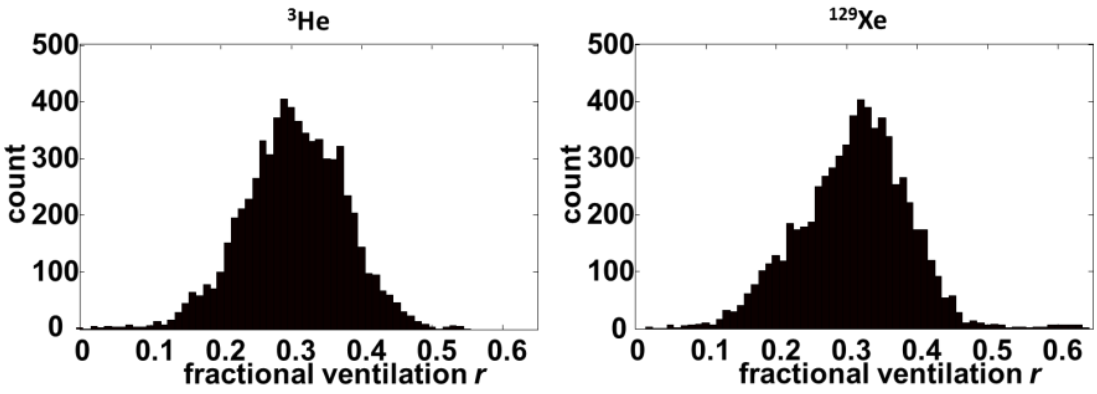

Figure 7.7: *Whole lung histograms of fractional ventilation values, derived from the maps in Figure 7.6. Only voxel which resulted in a successful calculation of fractional ventilation from both 3D maps were included in this comparison. Both datasets show very similar standard deviation/ventilation heterogeneity ($VH_{3\text{-}He}$=0.101 and $VH_{129\text{-}Xe}$=0.096).*

Voxel-by-voxel comparison / Volunteer	V1	V2	V3	V4	V5
VH_{Xe}	0.08	0.09	0.10	0.08	0.10
VH_{He}	0.11	0.08	0.10	0.07	0.10
Pearson's r (P<0.001)	0.51	0.46	0.66	0.53	0.27
%Mean Difference *r* (Xe-He)*	-30.0	+12.2	+2.9	+57.4	-22.3
%Standard deviation*	39.8	35.8	26.9	53.2	50.1
Gravitational slope (Xenon)	-0.015	-0.003	-0.042	0.009	-0.024
Gravitational slope (Helium)	-0.061	-0.039	-0.060	-0.020	>-0.001

Table 7.3: *Overview of results from voxel by voxel ^{129}Xe and ^{3}He MBW-imaging data analysis in 5 healthy volunteers. For subject demographics see Table 7.1. *percentage of mean over all values of fractional ventilation.*

Fractional ventilation maps for all subjects exhibited similar features and ventilation heterogeneity values for both hyperpolarised ^{3}He and ^{129}Xe data (Table 7.3). A voxel by voxel comparison of fractional ventilation values from the two nuclei for each volunteer showed highly significant correlations (Pearson's r ~0.5), with the exception of Volunteer 5. However, upon calculating the gravitational slope in fractional ventilation (as performed in Chapter 5 by fitting mean fractional ventilation from each coronal slice as a function of A-P position with a linear function) the gravitational slopes are considerably different for ^{3}He and ^{129}Xe with exception of Volunteer 5. The gravitational slopes in *r* were considerably higher for ^{3}He than ^{129}Xe.

7.4. Discussion and future work

Comparison of ^{3}He MBW-imaging using SPGR and bSSFP

The comparison of fractional ventilation values derived from ^{3}He MBW-imaging with SPGR and bSSFP sequences shows very good agreement in all volunteers. Considering ^{3}He is a scarce resource, bSSFP MBW-imaging is potentially a more economical alternative to SPGR requiring 50% less ^{3}He gas dosage. In addition the 10% ^{3}He : 90% N_2 mix used is a better approximation of the normal gas mix in the lung in terms of density and diffusion coefficient. Alternatively, bSSFP with the same gas dosage as SPGR permits the use of increased spatial resolution. One ^{3}He bSSFP MBW-imaging dataset was acquired using a 2-fold increase in voxel resolution in the coronal plane (64x64). Despite the increased resolution, higher SNR was measured in the first acquisition using optimised bSSFP compared to SPGR sequence at 32x32 (SNR_{bSSFP} = 39, SNR_{SPGR} = 33). In this healthy volunteer the higher resolution showed significant correlation with lower resolution SPGR-derived maps. This invariance of *r* distribution with voxel resolution suggests that a resolution of ~1cm^3 is sufficient to fulfil a major assumption of the washout model: that ventilation is homogeneous within a voxel. The ^{3}He datasets at different special resolution suggest that this assumption may hold in healthy volunteers. However, in patients with inhomogeneous ventilation (e.g. asthma, where ventilation heterogeneity starts with effects in the terminal bronchioles resulting in patchy patterns of ventilation) it may be less applicable. Thus, an increase in spatial resolution of acquired MBW-imaging data could provide greater insight into the length scale of the VH and the underlying disease process. Alternatively, the intra-voxel heterogeneity could be probed by measuring the deviation of fractional ventilation from a model decay. Insight into sub-voxel heterogeneity may be afforded by treating signal decay with a stretched exponential model rather than a mono exponential behaviour:

$$y = a \cdot e^{[\ln(S(n)]^{\alpha}} \qquad \text{Eq. [7.1]}$$

In this case the signal decay ($S(n)$) measured over *n* breaths can be represented by combination of mono exponential decay with a power law, with a factor α , which gives a semi quantitative estimation of heterogeneity [60].

For the ^{3}He SPGR-bSSFP comparison, a sequence with a Gaussian-shaped RF pulse (TR= 1.6msec) was used, but recent sequence developments have allowed a rectangular-shaped RF pulse (width 200µs) that reduces TR to 1.4ms and the total time for a volume acquisition to 1.4s. This configuration of the bSSFP sequence was used in the ^{3}He-^{129}Xe MBW-imaging comparison. In addition, the careful optimisation of the bandwidth and flip angle in future work could result in further improved bSSFP image quality [4]. However, a requirement of bSSFP is that the centre

frequency has to be carefully calibrated for each subject to avoid B_0 banding artefacts. Nevertheless, the calibration procedure is relatively simple to perform, and as a result, no major banding artefacts were observed in any of the datasets acquired in this work. In addition the broadening of the point spread function that results from the use of high flip angles is not expected to influence resulting image quality at the currently used resolution as the flip angle was deliberately kept smaller than the optimum [4] in order to preserve signal between breaths. Finally, the error estimation presented for SPGR imaging in Chapter 6 has to be revisited for bSSFP since diffusional dephasing of magnetisation during imaging gradients and effective T_2 effects have to be considered when quantitatively modelling the magnetisation (signal) with time in the total error function of bSSFP-derived fractional ventilation. Nevertheless, the fact that bSSFP fractional ventilation values findings show a good agreement with SPGR derived quantitative values is promising.

MBW-imaging of ^{129}Xe

3D multi-nuclear MBW-imaging with ^{129}Xe has been demonstrated. This has been made feasible by the efficient use of polarisation afforded by bSSFP sequences and the recent improvements in ^{129}Xe polarisation levels which have enabled high SNR images, to be obtained over 4 cycles of tidal breathing. In our preliminary work using SPGR, MBW-imaging did not provide sufficient SNR for multiple 3D acquisitions with ^{129}Xe MBW-imaging [174]. Comparable functional information was derived from MBW-I datasets from both nuclei, with similar ventilation heterogeneity exhibited by each nucleus for most subjects. The voxel by voxel comparison of regional fractional ventilation values resulted in a slightly lower average Pearson's correlation coefficient of r = 0.48 than found from comparing parametric maps from different sequences using the same gas (mean Pearson's r = 0.60). Nevertheless, correlations between data derived from both nuclei were highly significant ($P<0.001$ in all cases). Considerably different gravitational slopes in fractional ventilation for the two gases were found in all subjects. VH in healthy volunteers is usually associated with the gravitational distribution of ventilation and therefore this finding is unexpected and requires further investigation. In particular the differences may arise from altered breathing patterns in both experiments as well as different inspiratory levels, which will alter distribution of gases with different density throughout the lung. In the case of ^{129}Xe MBW-imaging the tracer gas makes about 15% of the inspired lung volume and might have an impact on air distribution. Nevertheless, we observed no clear trend between subjects to indicate a common alteration on breathing behaviour. Finally the properties of xenon as a much denser ($\rho_{He\text{-}N2}$=0.958kg/m^3, $\rho_{Xe\text{-}N2}$=2.905kg/m^3), and less diffusive gas might have an impact on the outcome of fractional ventilation ($D_{He\text{-}N2}$ = 0.90cm$_2$/s, $D_{Xe\text{-}N2}$ = 0.12 cm^2/s, [149, 187]).

A limitation of the current implementation of this dual MBW-imaging technique is associated with to the coil design. The dual-tuned coil is developed similar to a bib, with high sensitivity in the apex of the lung and drop off towards the base in posterior slices. This effect could be observed in all subjects. In the ^{129}Xe images this effect appears less pronounced than in ^{3}He images (Figure 7.6). The improved homogeneity of the Xenon images might be due to the considerably higher gas dose, resulting in higher concentration of gas throughout the lung. This has an impact on the inhalation of the gas itself (volunteers take longer to empty the gas bag for the Xenon experiment than for the Helium experiment) and the altered diffusivity of the gas mix in the lung might also impact the breathing pattern.

7.5. Conclusions

Fractional ventilation values derived from ^{3}He MBW-imaging using a 3D bSSFP sequence showed similar quantitative values as SPGR imaging. This bSSFP sequence is promising for future healthy volunteer and patient studies with MBW-imaging due to its efficient utilisation of polarisation and hence a reduction in the required gas dosage by a factor of 2. In addition in a single healthy volunteer it was shown that a resolution of 0.5x0.5x1cm resulted in comparable fractional ventilation maps to those derived from an isotropic resolution of ~1cm^{3}, which indicates in healthy normal lungs' VH is over a length scale greater than that of the voxel. In patients with considerable regional VH, a finer spatial resolution may however, be advantageous. The feasibility of 3D multi-nuclear MBW-I with ^{3}He and ^{129}Xe has been successfully demonstrated in 5 healthy volunteers for the first time. In future work, it may be possible to identify sensitivity differences in MBW-I with ^{3}He and ^{129}Xe to different physiological processes symptomatic of obstructive lung disease. Work could be taken forward with simultaneous ^{3}He-^{129}Xe MBW-imaging to monitor different properties of both gases simultaneously.

Chapter 8 Linking regional ventilation heterogeneity from hyperpolarised gas MR imaging to MBW in obstructive airways disease[7]

8.1. Introduction

After introducing MBW-imaging as a method to measure fractional ventilation in 3D in Chapter 5 and showing reproducibility of the method, it is important to test its feasibility and sensitivity to VH in patients. Since the developed method quantitatively measures ventilation with an approximate resolution of $1cm^3$ it is expected to be a sensitive tool for the evaluation of obstructive lung diseases. In this chapter, ventilation heterogeneity (VH) is assessed with this imaging method and the results are compared to pulmonary function tests sensitive to VH (LCI) [95, 109] and airflow obstruction (FEV1) [164].

The following two studies were performed in adults diagnosed with asthma and children with cystic fibrosis (CF) with normal spirometry. The outcome of MBW-imaging is analysed and statistically compared to pulmonary function tests including LCI from MBW with SF_6.

8.2. Methods

8.2.1. Subjects

Studies were performed with the consent of patients, volunteers or the parent (in case of the children in the CF study) and ethics committee approval. The asthma patient cohort included 30 moderate-severe patients with an FEV1 of 75±26% (mean ± standard deviation). Selected ventilation images of subjects from this cohort are also presented in Chapter 4. The other cohort was part of a study comparing early signs of lung disease in children with CF to heathy age-matched subjects. Children between the age of 6 and 16, all with normal spirometry (FEV1>80%) at recruitment, were imaged and 6 healthy subjects and 13 patients with CF have been recruited at this point. An overview of patient and volunteer data is presented in Table 8.1.

[7] The patient data acquired for this chapter were collected by the hyperpolarised gas imaging group in collaboration with Sheffield Children's Hospital and the Cinical Respiratory Group from the University of Leicester. Prof. Chris Brightling and Prof. Christopher Taylor are acknowledged here as representatives for their groups, who have recruited patients and helped with pulmonary function testing.

subject group	Age	Sex	mean r	std r	CV	skewness	LCIsitting	FEV1% perdicted	Gravitational slope(Δr/cm)
healthy children	10	F	0.41	0.09	21.61	-0.73	7.31	107	1.98E-03
	7	M	0.51	0.07	13.86	-0.20	6.64	98	1.71E-03
	8	F	0.42	0.07	8.49	0.51	6.64	98	1.19E-03
	14	F	0.51	0.07	11.99	0.03	5.87	84	1.03E-03
	14	M	0.39	0.06	16.52	-0.65	6.02	114	1.00E-03
	10	F	0.418	0.0501	11.98	-0.9068	6.38	89	8.74E-04
CF children	12	M	0.37	0.12	24.01	-0.53	7.73	94	8.89E-04
	10	M	0.45	0.09	20.92	-1.06	6.58	99	7.54E-04
	11	M	0.57	0.10	17.43	-1.58	6.61	110	1.37E-03
	16	F	0.56	0.09	15.89	-0.87	9.10	78	1.32E-03
	15	F	0.51	0.09	16.62	-0.50	6.04	95	1.37E-03
	12	M	0.44	0.08	22.66	-0.69	6.53	104	1.01E-03
	14	F	0.37	0.09	24.0	-0.57	7.26	92	5.09E-04
	8	F	0.46	0.10	21.51	-0.90	8.19	110	-2.89E-04
	11	M	0.57	0.06	11.30	-0.47	7.89	85	3.75E-04
	13	F	0.57	0.09	14.28	-1.61	6.63	96	3.16E-04
	10	M	0.46	0.08	16.59	-1.15	6.51	104	1.08E-03
	7	F	0.48	0.08	17.13	-0.69	7.10	107	5.33E-04
adult asthma	50	F	0.24	0.09	39.7	-0.25	12.93	54	2.08E-04
	54	F	0.31	0.14	46.02	0.39	9.04	33	2.21E-04
	65	M	0.37	0.13	35.20	-0.47	10.98	57	-2.61E-04
	56	F	0.48	0.09	18.69	-1.14	7.09	98	8.34E-04
	63	F	0.55	0.11	20.8	-1.28	11.52	70	8.75E-04
	53	F	0.56	0.11	18.91	-0.92	8.61	74	8.77E-04
	49	M	0.33	0.1187	35.98	-0.27	-	80	-6.91E-05
	65	M	0.28	0.10	37.47	-0.36	9.05	72	8.67E-04
	41	M	0.34	0.12	36.0	-0.19	7.37	97	1.11E-03
	51	F	0.32	0.15	45.84	-0.04	12.85	36	-3.01E-04
	59	F	0.43	0.10	22.81	-0.73	8.76	95	1.24E-03
	45	F	0.47	0.12	25.23	-0.51	8.84	44	-9.85E-06
	62	M	breath lost during acquisition				10.16	114	-
	61	F	0.28	0.09	30.26	-0.58	8.30	105	4.17E-04
	45	M	0.50	0.12	24.14	-0.60	9.87	72	-2.44E-06
	21	M	0.36	0.10	28.62	-0.68	7.08	98	3.24E-04
	64	F	0.43	0.07	16.7	-0.44	7.40	106	2.65E-04
	73	M	0.36	0.12	32.18	-0.43	12.56	41	-1.36E-03
	41	F	0.34	0.12	35.79	-0.32	8.77	87	1.20E-03
	66	M	0.34	0.12	35.89	-0.17	10.00	100	-2.58E-04
	36	M	0.43	0.09	22.13	-0.80	7.29	27	2.58E-04
	60	F	0.39	0.09	22.06	-0.12	6.34	122	8.10E-04
	62	M	0.31	0.11	35.15	-0.17	10.85	69	2.26E-04
	44	M	0.38	0.10	27.0	-0.78	7.80	78	-4.16E-04
	52	F	0.51	0.09	17.03	-0.53	5.86	101	1.57E-03
	42	M	0.43	0.08	19.55	-0.50	7.83	98	4.34E-04
	21	F	0.51	0.09	17.3	-0.65	7.31	84	6.83E-04
	57	M	0.31	0.11	34.86	-0.33	7.61	55	-6.57E-04
	34	M	0.41	0.12	29.48	-0.85	7.59	51	4.71E-04
	60	M	0.33	0.11	32.57	-0.37	9.95	47	-4.35E-04

Table 8.1: Overview of patient and subject details (dark blue=healthy volunteer, red=CF patient, turquoise = asthma patient) and imaging derived values as well as pulmonary function test results. For the fractional ventilation – as in previous chapters – r is used as an abbreviation. Predicted FEV1 was calculated according to Miller et al. [71].

8.2.2. Pulmonary function tests

All subjects underwent spirometry to obtain FVC and FEV1. Multiple breath washout (MBW) testing was conducted using the Innocor apparatus (Innovision, Glamsbjerg, Denmark) according to ATS/ERS guidelines [105]. A mixture of 0.2% SF_6 gas and air was used in the experiments. After washin of the tracer gas to equilibrium a washout was performed until the concentration had dropped to less than 1/40 of its original value (equals 0.005% of SF_6) for three subsequent exhalations. The system was used as described in Chapter 2 'Multiple breath washout (MBW)' [95]. The lung clearance index was derived from MBW as the lung turn-overs required to reduce the tracer gas concentration to 1/40 of its original value.

8.2.3. Washout imaging

Washout imaging was performed as described in Chapter 5. Upon inhalation of the hyperpolarised ^{3}He subjects held their breath for 2 calibration acquisitions, after which subjects began to breathe independently in synchronisation with acquisitions of the scanner. The delay between breaths was 4s in the case of the CF study on children and was increased to 5s in the case of the study on asthma patients, since children have a higher breathing frequency. Washout imaging was performed using a 3D spoiled gradient echo sequence covering the whole lung with the specific imaging parameters as described in Chapter 5: a 32x32 matrix and a subject dependent field of view between 30x30 cm^2 up to 42x42cm^2. This resulted in a resolution in the x-y-plane between 9.3mm-13mm, making voxels almost isotropic with a slice thickness of 10mm. The number of slices was altered between 20 and 28 slices depending upon subjects' size. With a phase field of view of 0.8 and an TR of 2.5ms this results in an acquisition time between 1.3s and 1.8s for each lung volume. The bandwidth of the receiver was 32.3 kHz with an echo time TE of 0.8ms. The flip angle was calibrated for each subject to 1°, as described in the preliminary experiments section; this is an empirical value to preserve as much hyperpolarised magnetisation as possible for images at later stages of the washout.

Asthma patients inhaled a fixed dose of 200ml hyperpolarised ^{3}He, the children were given between 100ml and 200ml (determined empirically according to predicted FRC). Doses were topped up with N_2 to 1 litre in the case of the adult asthmatic study and to 350-500ml for the CF children. In the case of patient studies, patients were monitored closely to ensure that they did not breathe between calibration scans or lose their breath. To monitor the steadiness of the breath-hold during calibration the lung volume segmented from both calibration images was compared and in addition the mean correction factor (Eq. [5.4], Chapter 5) was recorded. The mouthpiece connected to the flow sensor was placed in the subjects' mouth after inhalation of the gas mixture containing the ^{3}He from a Tedlar bag during the calibration breath-hold interval. Care was taken,

that patients had finished inhalation before the image acquisition began in order to avoid a delayed inflow of hyperpolarised gas during calibration. This would cause erroneous calibration values as gas would still be entering the lung during the acquisition of the first calibration image. To avoid this effect, the acquisition was delayed by one second after inhalation of the gas-mix. This resulted in a total breath-hold of 10s for the calibration followed by the subsequent exhalation-inhalation cycles from room air.

8.2.4. Image analysis

Parametric maps of fractional ventilation were derived from MBW-images using the algorithm described in Chapter 5. Assuming an approximately normal distribution of fractional ventilation over the whole lung, the standard deviation (SD) and mean values were derived from fractional ventilation maps. The histograms are used to derive skewness [188] of the distribution and coefficient of variation (CV). In addition, the gravitational gradient in ventilation was investigated. For each subject the average fractional ventilation for each coronal slice was calculated and a linear slope was fitted to the result, as shown in Figure 8.1.

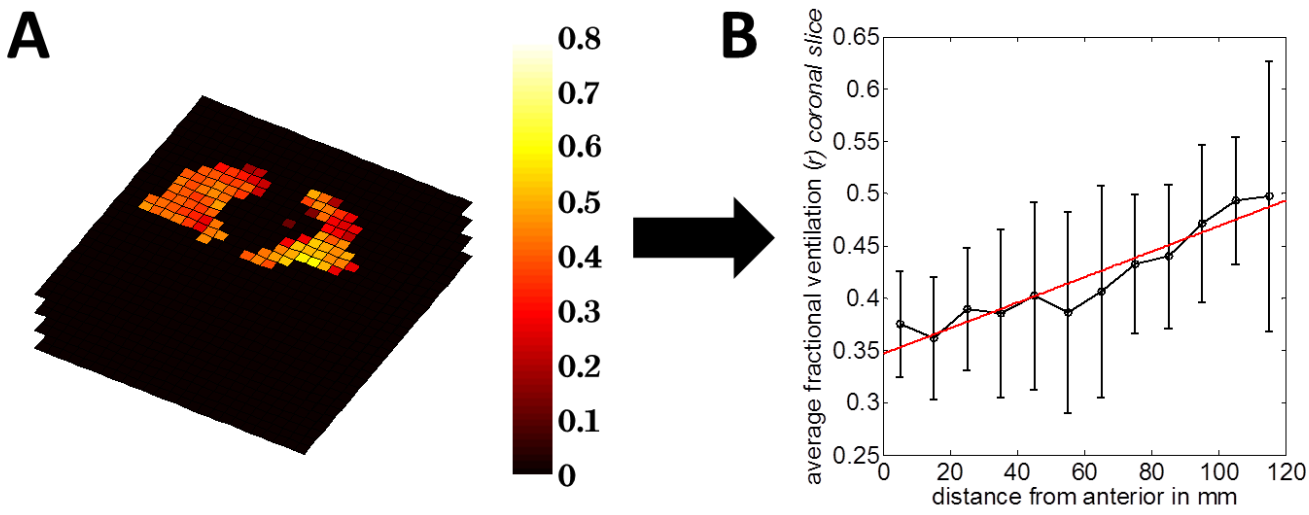

Figure 8.1: *The average of each 10mm coronal slice in 3D fractional ventilation maps (A) was plotted from anterior to posterior (B). A linear slope was fitted to measure influence of gravity on fractional ventilation in supine subjects. The slope has units of fractional ventilation per slice [Δr/cm] and can be used to evaluate ventilation changes from anterior-posterior.*

Statistical analysis

All subject groups were analysed together to find correlations between the image-derived parameters and the global MBW and spiromety results. Significant differences between the groups were tested using SPSS (IBM, Armonk, NY,USA) for statistical analysis. Spearman's r was calculated as well as a P-value to test significance of the non-parametric correlation. To compare differences between groups, analysis of variances (ANOVA) was performed with the null hypothesis that there was no difference between means. In order to compare the individual groups a Hochberg Post-hoc test [189] was performed to account for the different sized groups.

8.3. Results

Washout imaging was successfully performed in a total number of 47 subjects. Only one subject from the asthma study had to be excluded, as he did not follow breathing instruction during multiple breath washout imaging. In this subject a volume change of about 10% was found between imaging volumes of the calibration scans which resulted in 40% lower average correction factor than the other subjects. Spirometry was successfully assessed for all subjects. In one subject from the asthma study, the multiple breath washout test was not acquired. In total 23 males and 24 females were tested over an age range of 7 to 73 years. For the CF sub-study the healthy volunteers were age matched with the CF patients and therefore no significant difference in age was found with a mean age of 11.2±2.8 years (CF children) and 11.2±2.7 years (healthy volunteers). The asthma cohort with an average age of 52±13 years was considerably older than the healthy control group. An overview of all data is presented in Table 8.1. Figure 8.2 shows the comparison of fractional ventilation maps from a single slice from each subject group and of the whole lung histogram (bottom). Differences in VH can be seen in the single slices as well as the histograms, which show a broadening (increased SD) between the healthy volunteer and the CF patient as well as in the asthma patient's dataset. In addition, distributions in the diseased subjects appear more skewed.

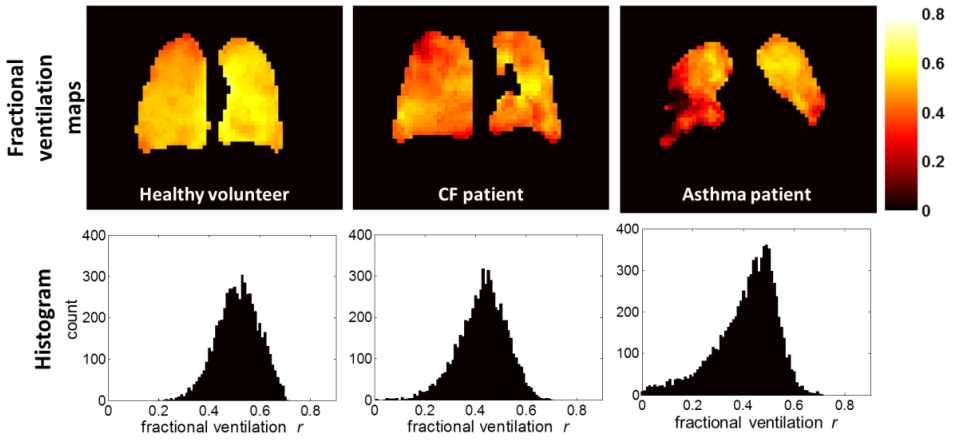

Figure 8.2: *Coronal slice of a single subject from each group investigated (top) and the corresponding whole lung histogram of fractional ventilation r from each subject group (bottom). Increase of VH can be visually seen in the fractional ventilation maps and is reflected in a broadening of fractional ventilation values in the histograms with increase of disease severity. FEV1% predicted: Healthy volunteer 98%, CF 104%, asthma: 51%*

8.3.1. Correlations

An overview of all correlations of MBW-imaging parameters with PFT parameters for all subjects is given in Table 8.2. Spearman's non-parametric test was applied since most of the data were not normally distributed as shown in the boxplots of Figure 8.4. Both LCI and FEV1 % predicted showed significant Spearman's correlations ($P<0.01$) with the image derived parameters; coefficient of variation of fractional ventilation histograms (CV) and the standard deviation (SD). SD of fractional ventilation was found to have the best correlation with pulmonary function tests and is plotted against LCI in Figure 8.3(1) and FEV1 in Figure 8.3(2). Skewness of fractional ventilation distribution did not show any correlation with pulmonary function tests and only showed correlation with another image derived parameter of VH - the CV ($r = 0.41$, $P<0.01$). The gravitational slope of fractional ventilation values correlated significantly with LCI and FEV1 ($r = -0.56$, $r=0.49$, $P<0.001$). Figure 8.3(3) shows the correlation between gravitational slope from the r-maps and SD ($r = -0.60$, $P = 0.001$). Measures of VH such as the derived SD and CV of the fractional ventilation maps correlated with LCI. Reduced gravitational slope and reduced FEV1 are both consistent with an increase of those metrics of ventilation heterogeneity.

8.3.2. Analysis of variances

An overview of the results from the ANOVA is shown in Table 8.3. To test the individual groups for significant difference a post-hoc analysis was performed. For significantly difference

variances between groups (Leven's test) a Games-Howell analysis was performed. The F-ratio as the measure of experimental variance to random variance was highest for SD of fractional ventilation. An overview of the results is shown in Figure 8.4 as boxplots. FEV1 in the healthy children was 98±11%, not significantly different (P=1) from 98±10% in children with mild CF, but both groups were found to be significantly different from the asthma group (P<0.01). On average the healthy children had an LCI of 6.5±0.6 compared to 7.1±0.9 in the CF children and 9.0±1.9 in the asthma cohort. The difference between children was found to be non-significant (P = 0.12), while both, the healthy children and the CF children groups were significantly different from the asthma cohort (P >0.001). Standard deviation (SD) of the fractional ventilation from histograms shows a significant difference between healthy volunteers and patients (P = 0.019). Of particular note only SD of fractional ventilation maps showed a significant difference between the healthy volunteer group, the CF patients and the asthma cohorts in a direct comparison. The gravitational slope shows a decrease with increasing SD, indicating that the anterior-posterior increase of fractional ventilation found in healthy volunteers is masked by disease related VH across the lungs. Gravitational slope in fractional ventilation shows a significant difference between asthma patients and CF children as well as healthy volunteers, but no difference between the age-matched patient and control groups from the paediatric CF-study. It can be observed that the gravitational effect, similar to FEV1 has a very high standard deviation in the asthma group, while SD and LCI show a tighter distribution in the same subject group.

Correlations

			standard deviation fractional ventilation distribution	coefficient of variation	skewness	LCI	FEV1% predicted	Gravitational Effect (delta(r)/cm)
Spearman's rho	standard deviation fractional ventilation distribution	Correlation Coefficient	1.000	.813	.188	.675	-.585	-.460
		Sig. (2-tailed)		.000	.206	.000	.000	.001
		N	47	47	47	46	47	47
	coefficient of variation	Correlation Coefficient	.813	1.000	.405	.660	-.479	-.534
		Sig. (2-tailed)	.000		.005	.000	.001	.000
		N	47	47	47	46	47	47
	skewness	Correlation Coefficient	.188	.405	1.000	.253	-.237	-.210
		Sig. (2-tailed)	.206	.005		.090	.108	.157
		N	47	47	47	46	47	47
	LCI	Correlation Coefficient	.675	.660	.253	1.000	-.544	-.555
		Sig. (2-tailed)	.000	.000	.090		.000	.000
		N	46	46	46	47	47	46
	FEV1% predicted	Correlation Coefficient	-.585	-.479	-.237	-.544	1.000	.492
		Sig. (2-tailed)	.000	.001	.108	.000		.000
		N	47	47	47	47	48	47
	Gravitational Effect (delta(r)/cm)	Correlation Coefficient	-.460	-.534	-.210	-.555	.492	1.000
		Sig. (2-tailed)	.001	.000	.157	.000	.000	.
		N	47	47	47	46	47	47

Table 8.2: *Non-parametric Spearman's correlations, significance levels (P-values) and subject number N comparing multiple breath washout imaging parameters (SD, CV, skewness, gravitational effect) and pulmonary function tests (LCI and FEV1). (Grey field show correlation is significant with P<0.01 (2-tailed)).*

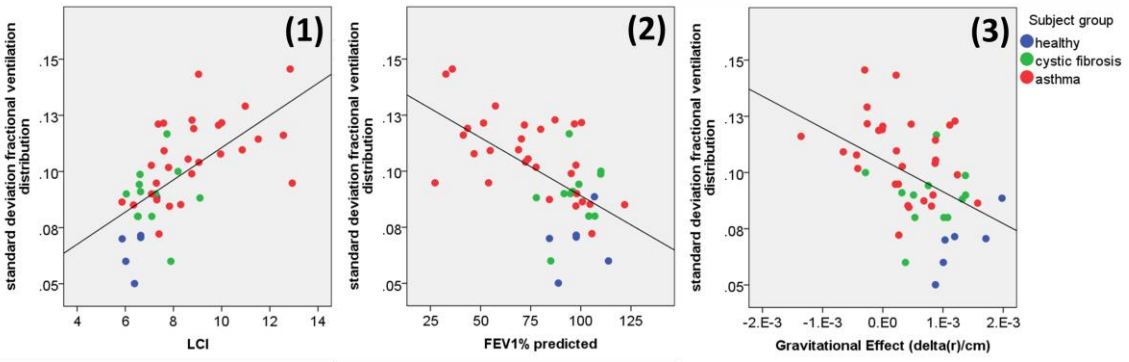

Figure 8.3: ***(1)*** *Correlation between standard deviation of fractional ventilation histograms and the lung clearance index (LCI). Blue circles represent the healthy volunteers, green the cystic fibrosis patients and red the asthmatics study. A significant correlation (P<0.001) of r = 0.68 was found.* ***(2)*** *Correlation between standard deviation of fractional ventilation histograms and forced expiratory volume in 1 second (FEV1). A significant negative correlation (P< 0.001) of r = -0.59 was found. FEV1 increases with decreasing ventilation heterogeneity.* ***(3)*** *Significant correlation between standard deviation of fractional ventilation and gravitation effects measured from changes of fractional ventilation from anterior-posterior coronal slices in all subjects. The anterior-posterior change in fractional ventilation is reduced with increased ventilation heterogeneity (r = -0.46, P <0.01). Black lines show a linear fit to all data in each of the graphs.*

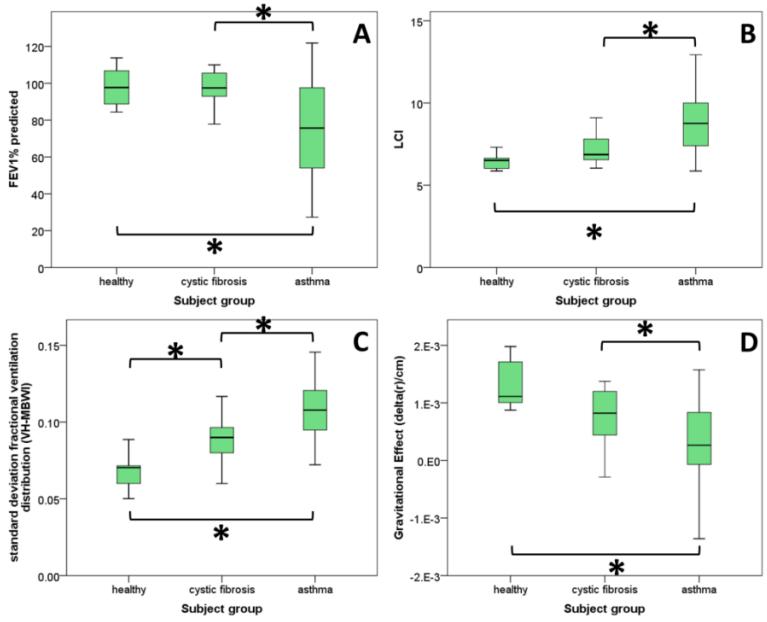

Figure 8.4: *Boxplots of imaging-derived variables and pulmonary function tests. (A) FEV1 (B) LCI (C) Standard deviation derived from fractional ventilation maps (SD/VH-MBWI) and (D) the gravitational slope.* *******=significant difference between groups (P < 0.01).*

Value	P - ANOVA	F-ratio	P(healthy,CF)	P(healthy,asthma)	P(asthma,CF)	P(Linear Model)
SD	<0.001	16.2	0.047	<0.001	<0.01	<0.001
CoV*	<0.001	15.9	0.16	<0.001	<0.001	<0.001
Grav.	0.001	7.7	0.22	0.002	0.101	0.001
LCI*	0.001	9.1	0.118	<0.001	0.001	0.001
FEV1	0.005	5.9	0.997	0.007	0.001	0.03

*Table 8.3: Overview ANOVA testing of MBW-imaging derived values and pulmonary function tests. P<0.05 of mean differences was selected as significance level. F describes the ratio of random variance to experimental variance. Grav. is an abbreviation for gravitational slope. *Levenne's test of equality of error variances P<0.01 (as a result a Games-Howell test was performed)*

In the case of the CF sub-study, MBW was performed in both a sitting position and supine in order to mimic the imaging posture. To test the two groups for significant difference LCI derived from sitting and supine MBW was compared. The findings are shown in Figure 8.5. An independent samples Mann-Whitney U test was performed to test the hypothesis that both distributions are the same. In the case of the sitting LCI- data the null hypothesis was retained (P = 0.18) while supine data showed a significant difference between patients and healthy volunteers (P = 0.02). There was no significant difference found when comparing LCI values supine and sitting within the subject groups, but in both cases the average supine LCI is higher than LCI measured sitting.

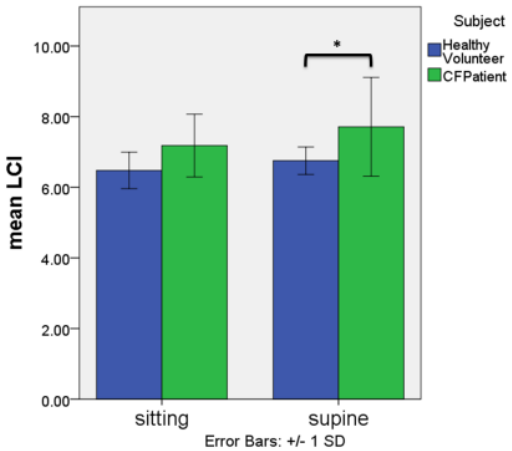

Figure 8.5: Comparison of LCI measured sitting and in supine position between heathy volunteers and CF patients. An independent samples Mann-Whitney U Test showed no significant difference between the two groups measured sitting, but with a significant different when MBW was recoded in supine position (P = 0.02).

8.4. Discussion

^{3}He MBW-I was used to produce fractional ventilation maps from patients and controls with healthy lungs in order to derive parameters to quantify ventilation heterogeneity (VH). In the case of patients with severe VH the model of each voxel being an independently ventilated compartment of the lung might be violated. Delayed ventilation representing collateral movement of gas between adjacent voxels in ^{3}He MRI breath-hold imaging has been shown before in COPD patients [170, 190] and similar effects can be found in asthma [191]. Signs of inter-voxel delayed ventilation during the breath-hold calibration interval were also found in some patients in the asthma cohort of this study [192]. Lung units affected by evidence of such delayed ventilation were however excluded from fractional ventilation maps to avoid errors introduced by inter-voxel signal increase during the calibration step. The associated signal increase would cause an overestimation of fractional ventilation that could even result in negative values. As such, we work on the premise that all voxels are at an equilibrium gas concentration at the endpoint of the breath-hold calibration period (~6s after inspiration). It is not certain to what extent delayed filling of lung units contribute to gas turnover as measured by MBW-I.

Both asthma and cystic fibrosis are obstructive lung diseases. Patients suffer from restriction to airflow caused by airway constriction and narrowing. As a result of restricted airflow, VH is expected to increase. VH is a term used to describe a heterogeneous ventilation of different regions of the lung, and can be directly studied and visualised using quantitative imaging methods like MBW-imaging. From fractional ventilation maps, regionally specific parameters can be generated in order to better understand VH. The standard deviation (SD) of fractional ventilation maps as a measure of VH was found to be most sensitive. The SD derived from the fractional ventilation maps was also shown to inversely correlate with FEV1 ($r = -0.61$, $P<0.001$). Similarly the lung clearance index (LCI) increases with rising VH and shows a positive correlation with SD ($r = 0.625$, $P<0.001$). SD also incorporates the effect of gravity, as a well-known and described VH found in healthy volunteers across the whole lung (see Chapter 2). The gravitational effect of increase of ventilation from non-dependent to dependent parts of the lung is reflected in a slope of fractional ventilation from anterior to posterior parts of the lung. Gravitational effects in lung ventilation have previously been shown to change with disease [193-195]. It is hypothesised that with an increase of VH the effect of gravity on ventilation becomes less apparent as it is masked by high variation of fractional ventilation between different regions of the lung determined by the underlying location of the disease related physiological changes. This is supported by the negative correlation between the gravitational effect and LCI ($r = -0.55$, $P<0.001$), CV ($r = -0.53$, $P=0.002$) and SD of fractional ventilation ($r = -0.46$, $P<0.001$) and in contrast, a positive correlation with FEV1 ($r = 0.55$, $P<0.001$) was found, i.e. in healthy lungs with little ventilation impairment the anterior-posterior slope in ventilation is a good indicator of healthy lung ventilation. The slightly

lower correlation of the gravitational slope and SD (derived from the same images) when compared to the correlation of gravitational slope with pulmonary function tests might be explained by the fact that in healthy volunteers an increased gravitational effect results in a higher VH. A trend of increase in VH with increasing gravitational effect was found in both the healthy volunteers and the CF-patients, but was not statistically significant.

The coefficient of variation (CV) was also derived from fractional ventilation maps as the standard deviation divided by the mean value of fractional ventilation. Since the mean value of the fractional ventilation is dependent on tidal volume, this therefore makes CV effort-dependent. Significant correlations of CV with FEV1 ($r = -0.479$ $P<0.01$) and LCI ($r = 0.660$, $P<0.01$) were found, similar to SD. In addition, the skewness of fractional ventilation histograms was measured and Spearman's correlation ($r = 0.40$, $P <0.01$) with CV was the only significant relationship found. Skewness of the fractional ventilation distribution in the whole lung seems to be less sensitive to changes in VH.

Significant differences in imaging-derived parameters and PFTs were found between the much older asthma patients and the children in the CF-study (both patients + volunteers). This is not surprising when comparing an asthma cohort with a mean age of 52 years and predicted FEV1 of 75±26% to children with mean age of 11 and predicted FEV1 > 80% in the CF study. Of particular interest is the comparison of the heathy volunteers group with the age matched CF patients where the MBW-imaging SD showed significant difference between groups, while LCI and FEV1 differences did not show significant differences. In Figure 8.5 a trend in difference between heathy volunteers and CF patients was seen when looking at the LCI, which might be expected to become significant with an increase of recruited subjects for this study.

The SF_6 MBW (LCI) was routinely acquired in the upright position whilst imaging was performed in the supine position due to the horizontal bore of the MRI scanner. Especially for patients with CF, a change in position might alter the ventilation pattern as mucus can shift within the lung when body position changes. This hypothesis is supported by the significantly higher LCI in CF patients than in healthy volunteers found when performing MBW in supine position. Unfortunately those data were not collected for the asthma study and it is questionable if similar effects might be found in asthmatics where mucus probably plays a lesser role in lung obstruction. LCI sitting was greater than LCI supine in healthy volunteers, although not significantly, so these changes may be derived from differences in tissue compression (gravitational effect) when performing MBW in supine. This result has to be tested in a bigger cohort of healthy volunteers and patients.

8.5. Conclusions

It was shown that MBW-imaging is feasible with patients as young as 6 years old. Patients with predicted FEV1 <30% were also found to be able to perform the MBW-imaging breathing protocol as only a single long breath-hold of <11s was required before breathing in synchronisation with image acquisition. This makes MBW-imaging a potentially useful and promising technique to quantify regional ventilation in the whole lung in patients with lung disease.

MBW-imaging derived parameters (SD, CV, gravitational effect) were shown to correlate significantly with pulmonary function tests. The standard deviation of fractional ventilation maps (SD) is a robust measure of ventilation heterogeneity (VH) that is less likely to be masked by breathing effort than the coefficient of variation (CV) [176]. SD derived from MBW-imaging was shown to be sensitive to the early changes in VH, whereas all other metrics did not result in significant differences between investigated subject groups. The LCI itself is more sensitive to early changes in CF when measured in supine position rather than upright sitting in this group of patients with mild CF and it can be expected increasing the number of patients recruited will result in a significant difference between mean LCI of the two groups.

The gravitational effect in healthy volunteers in the absence of ventilation defects is expected to explain any underlying VH. However, from the data from the two patient studies it was possible to show that with increased severity of disease (lower FEV1, higher VH) the gravitational effect becomes less apparent, which is consistent with gravitational effects measured with other imaging techniques in lung disease.

In future work it will be investigated how VH measured from MBW-imaging (SD) changes with age. It is not expected to be highly age dependent since only a small change of VH sensitive LCI has been shown before [95].

Chapter 9 Future work - linking multiple breath washout imaging to global multiple breath washout tests with modelling

9.1. Introduction

In the previous chapter multiple breath washout (MBW) derived indices from whole lung tests were compared to standard deviation of fractional ventilation maps derived from MBW-imaging. Both metrics of ventilation heterogeneity (VH) were shown to correlate significantly. Here a basic theoretical model is presented to directly compare exhaled tracer gas volume predicted from functional information (MBW-imaging) and that measured by sampling concentration and flow at the mouth with MBW. While MBW samples tracer gas with a high temporal resolution, it is a 1-D test and information on VH is inferred from the temporal course of measured gas concentration. This information cannot provide a unique solution from a regional perspective regarding VH. MBW-imaging on the other hand derives functional information (fractional ventilation r) regionally for each voxel, but due to the properties of the hyperpolarised gas used and duration of a whole lung image acquisition, currently only a single measurement is acquired for each breathing cycle and therefore it currently lacks the temporal information.

The comparison of quantitative functional lung MRI with MBW from the pulmonary function lab has been presented before by Sá et al. [176]. The approach uses regional signal changes from oxygen enhanced ^{1}H MRI washin and washout to derive specific ventilation[8] maps of a single sagittal slice. To directly compare specific ventilation histograms from imaging with MBW-curves the most likely distribution of specific ventilation is recovered from the global values measured at the mouth using the method from Lewis et al. [125]. VH here was assessed as the standard deviation of the logarithmic distribution of specific ventilation and showed good correlation with small differences (~10%) between both measurements. This comparison, Nevertheless, is rather similar to work presented in Chapter 8 and does not atempt to model or directly compare MBW-tracer gas decay with time.

The approach taken in this chapter to compare MBW measured from the pulmonary function lab to 3D MBW-imaging using hyperpolarised gas MRI is novel. Instead of recovering regional information from a global measurement, the regional functional information obtained from MBW-imaging is used to model the global signal (tracer gas volume) washout from the whole

[8] Specific ventilation definition can be found in Chapter 2 Eq. [2.28]. Specific ventilation can be directly converted to fractional ventilation.

lungs. Preliminary findings and the work in progress is presented, problems and deficiencies are addressed in the discussion.

9.2. Methods

In this preliminary methodological work 3 healthy subjects (female, 31; male, 30; male, 23) were examined. Subjects' details can be found in Table 5.1 and correspond to Volunteer 3, 5 and 6. All volunteers had normal spirometry and an LCI<7.

Flow measurement

To ensure the same flow resistance at the mouth in both the MBW and MBW-imaging measurements the same bacterial filter (9070.01YAUA, air Safty LIMITED, UK) and flow sensor (3700/4700, Hans Rudolph, KS, USA) were used for both techniques.

9.2.1. MBW-imaging

MBW-imaging as introduced in Chapter 5 was acquired with the same imaging parameters, protocol instructions and post-processing steps. With the above mentioned model assumptions the regionally obtained functional information (fractional ventilation *r*-maps) can be used to simulate a global tracer gas washout. Fractional ventilation as the ratio of fresh gas entering a voxel compartment to the total amount of gas in the compartment is used to describe behaviour of a gas mix introduced in the lung (during MBW-imaging a gas mix of air + ^{3}He). Assuming that the gas measured during MBW-imaging has similar properties (diffusion, density) as a mix of air and 0.2% SF_6, the functional information about the lung can be used to simulate behaviour of this gas mix in the lung.

By summation of the regional information of tracer gas volume in a compartment (voxel) after each breath a global residual gas volume in the whole lungs can be calculated:

$$V_{res}(n) = \int_{V(x,y,z)} (1 - r(x,y,z))^n \cdot C_{ini}(x,y,z) \cdot V_{vox} \cdot dV \qquad \text{Eq. [9.1]}$$

Where V_{res} (n) is the residual volume of tracer gas summed over all compartments of the lung after the n-the breath. C_{ini} is the initial concentration in each voxel. During ^{3}He washout this is proportional to the initial image intensity and is not homogeneous throughout the lung. For a comparison with a MBW-concentration curve from the pulmonary function lab C_{ini} is assumed to be constant in each voxel at $C_{ini}(SF_6)$ = 0.2% in the whole lung just before the washout begins (n=0). V_{voxel} is the volume of each compartment (voxel). $r(x,y,z)$ is the fractional ventilation (see

*Figure 9.1*A) of a given voxel location (*x*,*y*,*z*). Figure 9.1B shows the modelled residual gas volume calculated using the *r* maps from 4 compartments (shown in top right corner of that figure) from Figure 9.1A ($C_{initial}$ = 0.2%).

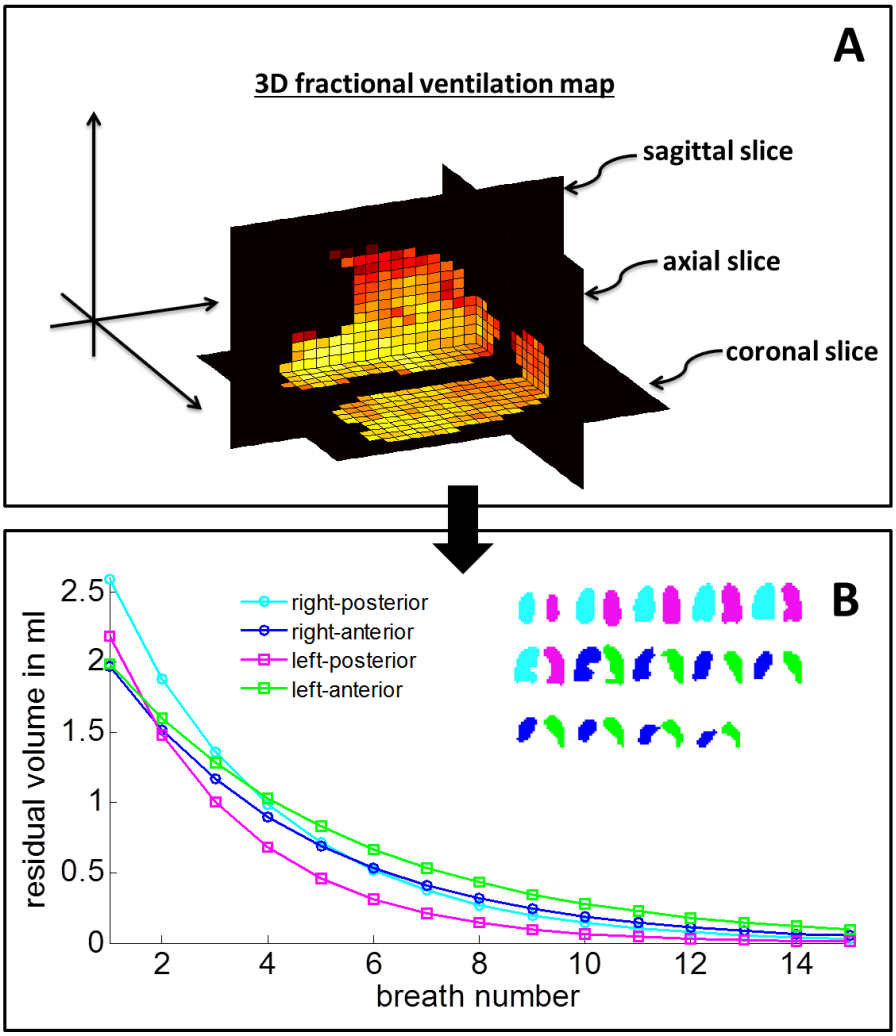

*Figure 9.1: (**A**) Fractional ventilation map r is used to predict the concentration washout for each voxel from Volunteer 6. (**B**) Residual gas volume in 4 compartments in the lung (left-right, posterior-anterior, compartments shown in top right corner). A uniform equilibrium gas concentration of 0.2% tracer gas is assumed at the beginning (breath n=0) and the acquired functional information (fractional ventilation r) is used to calculate residual gas volume after each breath in each of the 4 compartments. The sum of all compartments is equal is total residual tracer gas volume left in the lung measured with MBW at the mouth.*

From the residual gas measured in the lung with each breath the total exhaled volume of tracer gas exhaled after each breath can then be calculated:

$$V_{exhaled}(n) = V_{residual}(n-1) - V_{residual}(n) \qquad \text{Eq. [9.2]}$$

9.2.2. MBW

MBW was performed as described in Chapter 2 and as specified in the ERS-ATS guidelines [105]. To mimic the position of subjects in the MRI, all MBW measurements were recorded supine. Since breathing pattern during MBW-imaging was interrupted by image acquisition, the acoustic noise of the MRI scanner was recorded and played out during the gas washout. Subjects were encouraged to breathe in synchronisation with the recording to mimic MBW-imaging protocol. Figure 9.2A shows recordings from the flow and gas concentration from the MBW device. In the flow-pattern, zero flow is found after each inhalation, imitating the breath-hold during an MRI-acquisition. With knowledge of gas concentration over time and flow-rate the accumulated exhaled volume for each breath *n* can be calculated as follow:

$$V_{exhale}(n) = \int_{t_1(n)}^{t_2(n)} C(t) \cdot Q(t) \cdot dt = \sum_{t_1(n)}^{t_2(n)} C(t) \cdot Q(t) \cdot T_s \qquad \text{Eq. [9.3]}$$

Where $C(t)$ is the concentration recorded during MBW and $Q(t)$ is the flow. The start and end of an exhalation denoted by $t_1(n)$ and $t_2(n)$ which are defined by the zero crossing from positive flow to negative. T_s is the sampling rate of flow-gas analyser, which is in case of the Innocor system (Innovision, Glamsbjerg, Denmark) used here 10ms. The sampled data time course from Figure 9.2A were integrated using Eq. [9.3] and the exhaled tracer gas volume is plotted over breath number *n* in Figure 9.2B.

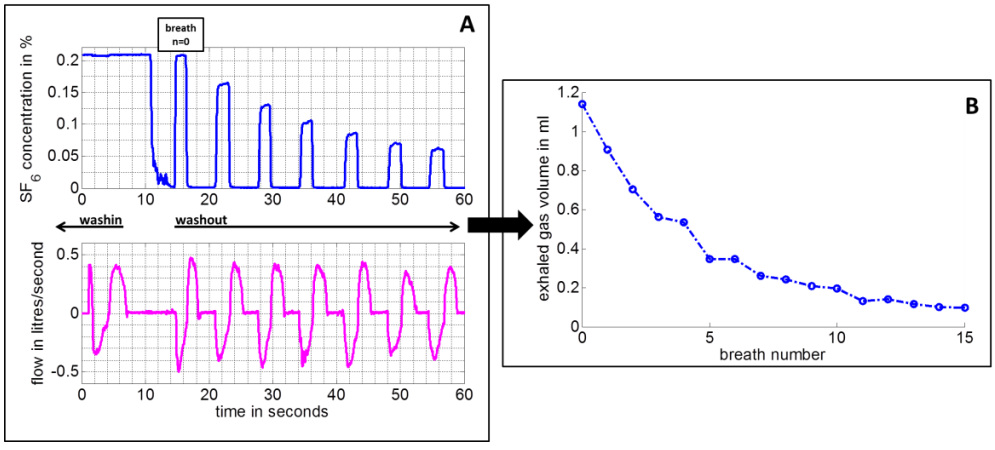

Figure 9.2: (A) MBW showing SF_6 concentration and flow recordings from Volunteer 6. Breathing was synchronised with recorded sound from MR MBW-imaging acquisition, which explains the zero-flow following each breathing cycle after inspiration. Similar to the calibration phase during the disconnection of the gas subjects held their breath before starting synchronised

breathing with breath n=0. (B) Exhaled tracer gas volume in each breath calculated from the recordings in A.

Comparison

For a direct comparison of exhaled tracer gas volume the exhaled tracer gas volume is plotted against the total gas exhaled of each breath. This allows a comparison despite differences in tidal volumes between experiments.

9.3. Results

Figure 9.3 shows the preliminary results of comparison of ^{3}He MR image based model of MBW versus SF_6 washout from three healthy volunteers. The figure shows the exhaled tracer gas volume plotted against the total exhaled volume on the left. Error-bars are derived from standard deviation of measurements. The result from Volunteer 3 shows a good match between both curves. Curves from Volunteer 5 and 6 do not match as well. For Volunteer 6 the two curves do not show a good agreement after about the 4th breath and the two curves drift apart. Important for this comparison Table 9.1 gives an overview of functional residual capacity and tidal volume made with pneumotachograph during experiments.

Subject	TV MBW-I	TV MBW
Volunteer 3	680±74	648±41
Volunteer 5	1164±86	983±47
Volunteer 6	914±7	678±46

Table 9.1: Overview pulmonary volumes measured during experiments. TV is the tidal volume measured in ml from flow-recordings.

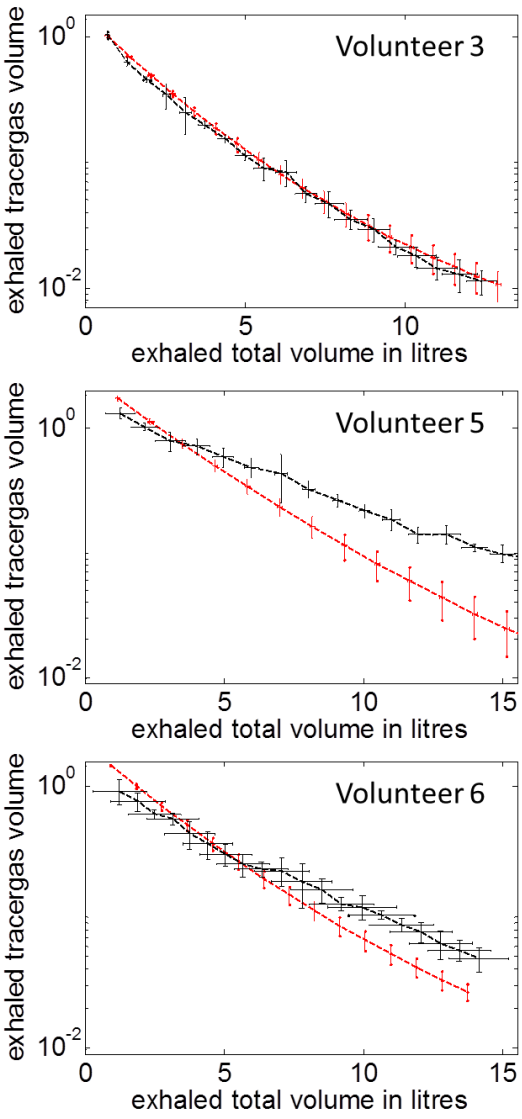

Figure 9.3: Exhaled tracer gas concentration over exhaled gas volume. Comparing global data as calculated from MBW-imaging (red) with MBW measured in the pulmonary function lab (black). Error bars are the standard deviation of repeated measures.

9.4. Discussion

The comparison of the MBW-imaging model and global MBW was successful only in one volunteer, who managed to breathe at the same tidal volume in both experiments. Despite the fact that specific ventilation derived from OE-MRI has been scaled with tidal volume by Sá et al. [176] similar adjustment was not done here, but exhaled tracer volume was rather plotted over total exhaled volume. This is done to compensate for the effect of changes in tidal volume on the amount of exhaled tracer gas.

The results from this direct comparison show altered breathing pattern results in a deviation of the curve. The assumption made by Sá et al. i. e. that SV in all units scales with *TV* is questionable and might not hold for bigger changes in tidal volume [178]. Observed changes in TV between the experiments from Voluneer 5 and 6 were about 15%. Dynamic ^{1}H MRI or CT could help assess the linearity of lung expansion with *TV*.

In addition it is assumed in the compartmental model of the lung that all functional units in the lung are separate and gas is distributed and mixed uniformly within each compartment. This assumption was tested in Chapter 7 (comparing two different resolutions) and holds for healthy volunteers with an uniform distribution of fractional ventilation, as tested here.

Furthermore, two different tracer gases are used for both techniques. Both gases have different density and diffusion ($D_{3He\text{-}air}$ = 0.9cm^2/s [187], $D_{SF6\text{-}air}$ = 0.035 cm^2/s [196]), but in the concentrations of the tracer gases used for these experiments the influence can be neglected. A single dose of ^{3}He is inhaled during (200ml) MBW-imaging mixed with N_2 (800ml) resulting in a concentration of less than 7% ^{3}He in air in all cases and SF_6 in air is 0.2% immediately after washin.

9.5. Conclusions

These preliminary results show promising agreement in the volunteer, who managed to match the tidal volume in both the MBW-imaging and MBW experiments. This comparison shows the difficulty of this direct comparison and how sensitive to changes both methods are. In the future training volunteers in breathing procedure before each data acquisition solve those problems. An alternative would be to record tracer gas concentration at the mouth while performing the MBW-imaging. This would exclude mismatching derived from different breathing pattern or lung inflation. In addition this could be done with different tracer gases used for imaging, such as SF_6 (^{19}F-imaging) which could be used together with fast gas analysers (Chapter 2, Multiple breath washout (MBW), page 40).

Chapter 10 Conclusions

This thesis investigated hyperpolarised gas MRI methods to measure lung ventilation in a quantitative fashion. Three methods were introduced and discussed. Application in patients was successfully shown.

Chapter 3 demonstrated the use of single breath-hold hyperpolarised ^{3}He ventilation and ^{1}H anatomical MRI acquisition (Figure 10.1) to increase the reproducibility of percentage ventilation volume (%VV) calculation to provide spatially and temporally registered images. This improved reliability when compared to a separate breath-hold technique will reduce statistical noise and could therefore reduce the number of participants to evaluate the outcome of clinical studies with a smaller number of participants. An optimised workflow automates process in major parts and reduces the user variability.

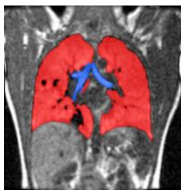

Figure 10.1: Single coronal slice of superpositioned ^{3}He image and ^{1}H image anatomical scan of the lungs using the single breath-hold technique from a healthy smoker.

Chapter 4 took ventilation image derived quantitative metrics one step further by using regional intensity differences between images before and after treatment. This maximises the regional information by taking intensity based regional and directional changes in ventilation into account. Changes of ventilation are quantitatively expressed in percentage change to treatment (%TR, Figure 10.2). The feasibility to monitor treatment response in longitudinal studies with this technique, as shown in Chapter 4, could be of great advantage. In this preliminary study no significant advantage over %VV and FEV1% predicted was demonstrated, but further studies could show the advantage of this metric.

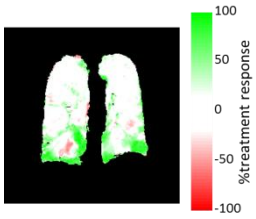

Figure 10.2: Treatment response showing effects of a bronchodilator in patient with asthma (Volunteer 7, Table 4.1)

Chapter 5 introduced the method of multiple breath washout imaging (MBW-imaging) as a quantitative functional imaging method, based on regional signal decay. This allows us to derive values of fractional ventilation. An example fractional ventilation map from a 2D acquisition is shown in Figure 10.3. Errors influencing the quantitative outcome are systematically investigated (**Chapter 6**) and improvements are achieved using steady-state imaging sequences to acquire data from MBW-imaging (**Chapter 7**). These improvements result in the feasibility to acquire ^{129}Xe MBW-imaging data.

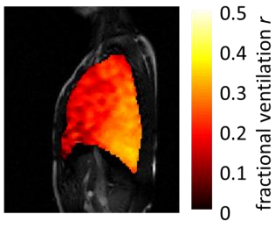

Figure 10.3: Fractional ventilation map of a sagittal slice in a healthy volunteer superimposed on a ^{1}H image.

Chapter 8, MBW-imaging derived metrics were shown to correlate significantly with pulmonary function tests. MBW-imaging is shown to be more sensitive to increased ventilation heterogeneity in a young CF cohort than spirometry and even than its pendant in the pulmonary function lab, LCI. Example coronal fractional ventilation maps from two patients are shown in Figure 10.4.

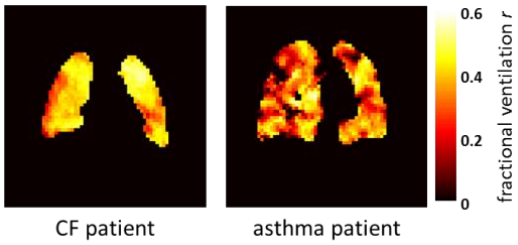

Figure 10.4: Example slices of fractional ventilation map from a CF and an asthma patient.

The regional information provided by MBW-imaging gives unique spatial insight into the washout time constants of the whole lung, and may help therefore help understanding the concept of ventilation heterogeneity in the context of clinical MBW measurements made from the whole lung (e.g. LCI). The preliminary work presented in **Chapter 9** shows that functional information from MBW-imaging can be linked to conventional MBW, an important pre-requisite for the subsequent regional interpretation of MBW.

List of figures

List of tables

List of publications

Journal Papers

1. Lung ventilation volumetry with same breath acquisition of hyperpolarized gas and proton MRI.
   Felix C. Horn, Martin H. Deppe, Helen Marshall, Juan Parra-Robles, Jim M Wild
   Journal of Applied Physiology (1985). 2014; 116(2):129-39.
2. Reply to Verbank and Paiva.
   Jim M. Wild, Felix C. Horn
   Journal Applied Physiology (1985). 2014 May; 116(9):1258.
3. Lung ventilation with same-breath acquisition of hyperpolarized gas and proton MRI.
   Felix C. Horn, Bilal A. Tahir, Neil J. Stewart, Guilhem J. Collier, Graham Norquay, General Leung, Rob H.. Ireland, Juan Parra-Robles, Helen Marshall, Jim M. Wild
   NMR in Biomedicine. 2014 September; 27(12):1461-7.
4. Comparison of CT-based Lobar Ventialtion with ^{3}He MRI Ventilation Measuments in Asthmatics
   Bilal A. Tahir, Cederic Van Holsbeke, Rob H. Ireland, Andy Swift, Felix C. Horn, Helen Marshall, John C. Kenworthy, Juan Parra-Robles, Ruth Hartley, M Laurencin, Richard Kay, B Chris, Jan De Backer, Wim Vos, Jim M. Wild
   Radiology (accepted)
5. Quantitative treatment response mapping using hyperpolarized 3He MRI in asthma patients
   Felix C. Horn, Helen Marshall, Richard Kay, Christopher E. Brightling, Juan Parra-Robles, Jim M. Wild
   (In preparation)
6. Linking regional ventilation heterogeneity from hyperpolarised gas MRI to multiple breath washout in obstructive lung disease
   Felix C. Horn, Juan Parra-Robles, Alexander Horsley, Richard Kay, Ina Aldag, Salman Seddiqui, Christopher E. Brightling, Christopher Taylor, Helen Marshall, Jim Wild
   (In preparation)

Oral Presentation

1. Quantitative mapping of treatment response in the lungs of asthmatics using hyperpolarized ventilation ^{3}He MRI
   Congress of the American Thoracic Society, San Diego (2014)

2. Multiple breath washout with hyperpolarised gas MRI
   UK Respiratory and Pulmonary Vascular Imaging Meeting, Sheffield (2014)
3. Bronchodilator treatment response mapping in COPD using hyperpolarized gas ventilation MRI
   European Respiratory Society, Barcelona (2013)
4. Multiple breath washout with hyperpolarised gas MRI
   Lung-From molecule to image, Bordeaux (2013)

Poster presentations

1. Visualizing regional ventilation heterogeneity by linking multiple breath washout to ^{3}He MRI imaging
   Felix C. Horn, Alexander Horsley, Laurie Smith, Christopher Taylor, Helen Marshall, Juan Parra-Robles, Jim M. Wild
   European Respiratory Society, Munich (2014)
2. Delayed gas filling imaged in asthma patients using hyperpolarised ^{3}He MRI
   Felix C. Horn, Helen Marshall, Juan Parra-Robles, Christopher Brightling, Jim M. Wild
   European Respiratory Society, Munich (2014)
3. Detection of early-stage lung disease in cystic fibrosis; comparing the sensitivity of ^{3}He and ^{1}H MRI, CT and LCI
   Helen Marshall, David Hughes, Alexander Horsley, Felix C. Horn, Laurie Smith, Juan Parra-Robles, Steve Cunningham, Leanne Armstrong, Ina Aldag, Christopher Taylor, Jim M. Wild
   Conference Paper, European Respiratory Society, Munich (2014)
4. Comparison of CT-based lobar ventilation models with ^{3}He MRI ventilation measurements in asthmatics
   Bilal A. Tahir, Cederic Van Holsbeke, Rob H. Ireland, Andy Swift, Felix C. Horn, Helen Marshall, Juan Parra-Robles, Ruth Hartley, Richard Kay, B Chris, Jan De Backer, Wim Vos, Jim M. Wild
   European Respiratory Society, Munich (2014)
5. Linking Helium-3 MRI Washout Imaging To Multiple Breath Washout - First Steps To Understanding Regional Lung Ventilation Heterogeneity
   Felix C. Horn, Alexander Horsley, Helen Marshall, Christopher Taylor, Juan Parra-Robles, Jim M. Wild
   American Thoracic Society, San Diego (2014)
6. Assessment of Structural And Functional Changes In Early Stage CF With Helium-3 MRI, CT And Multi-Breath Washout

Helen Marshall, David Hughes, Alexander Horsley, Felix Horn, Laurie Smith, Juan Parra-Robles, Leanne Armstrong, Ina Aldag, Christopher Taylor, Jim M. Wild
American Thoracic Society, San Diego (2014)

7. Comparison of global multiple breath washout measured at the mouth to imaging multiple breath washout in healthy subjects and Cystic Fibrosis patients
   Felix C. Horn, Juan Parra-Robles, Helen Marshall, Christopher J. Taylor, Alexander Horsley, Jim M. Wild
   International Society of Magnetic Resonance in Medicine, Milan (2014)
8. Hyperpolarised ^{3}He MRI is superior to lung clearance index in detection of ventilation abnormalities in young children with mild CF
   Helen Marshall, Alexandere Horsley, Laurie Smith, David Hughes, Felix C. Horn, Leanne Armstrong, Juan Parra-Robles, Steve Cunningham, Ina Aldag, Christopher Taylor, Jim M. Wild
   British Thoracic Society, London (2013)
9. Comparison of CT-based Lobar Ventilation with Hyperpolarized 3He MRI using image registration
   Bilal A. Tahir, Cederic Van Holsbeke, Rob H. Ireland, Andy Swift, Felix C. Horn, Helen Marshall, Juan Parra-Robles, Ruth Hartley, M Laurencin, Richard Kay, B Chris, Wim Vos, Jim M. Wild
   International Workshop of Pulmonary Functional Imaging, Madison,WI (2013)
10. Comparison of CT-based lobar ventilation models with ^{3}He MRI ventilation measurements in asthmatics
    Bilal A. Tahir, Cederic Van Holsbeke, Rob H. Ireland, Andy Swift, Felix C. Horn, Helen Marshall, Juan Parra-Robles, Ruth Hartley, M Laurencin, Richard Kay, B Chris, Jan De Backer Wim Vos, Jim M. Wild
    European Respiratory Society, Barcelona (2013)
11. Registration based estimates of lung ventilation
    Asmund Kjorstadt, Dominique Corteville, Felix C. Horn, Fank Zöllner, E Hodneland, Christian Fink, Lothar R. Schad
    ESMRMB, Toulouse (2013)
12. Reliable free breathing 3D multiple breath gas washout with hyperpolarized ^{3}He lung MRI
    Felix C. Horn, Martin H. Deppe, Juan Parra-Robles, Jim M. Wild
    International Society of Magnetic Resonance in Medicine, Salt Lake City, UT (2013)
13. Reproducible Multiple-breath washout imaging in 3D
    Felix C. Horn, Martin H. Deppe, Juan Parra-Robles, Jim M. Wild
    BCISMRM, Cambridge (2012)

14. Observation of gravitational dependence of regional fractional ventilation in human lungs with 2D and 3D multiple-breath washout imaging of ^{3}He and ^{129}Xe
    Felix C. Horn, Martin H. Deppe, Helen Marshall, Graham Norquay, Juan Parra-Robles, Jim M. Wild
    International Society of Magnetic Resonance in Medicine, Melbourne (2012)

References

1. Albert, M.S., et al., *Biological magnetic resonance imaging using laser-polarized 129Xe.* Nature, 1994. **370**(6486): p. 199-201.
2. Middleton, H., et al., *MR imaging with hyperpolarized 3He gas.* Magnetic resonance in medicine : official journal of the Society of Magnetic Resonance in Medicine / Society of Magnetic Resonance in Medicine, 1995. **33**(2): p. 271-5.
3. Deppe, M.H., et al., *A flexible 32-channel receive array combined with a homogeneous transmit coil for human lung imaging with hyperpolarized (3) He at 1.5 T.* Magnetic resonance in medicine : official journal of the Society of Magnetic Resonance in Medicine / Society of Magnetic Resonance in Medicine, 2011.
4. Wild, J.M., et al., *Steady-state free precession with hyperpolarized 3He: experiments and theory.* J Magn Reson, 2006. **183**(1): p. 13-24.
5. Deppe, M.H. and J.M. Wild, *Variable flip angle schedules in bSSFP imaging of hyperpolarized noble gases.* Magn Reson Med, 2012. **67**(6): p. 1656-64.
6. Ajraoui, S., et al., *Compressed sensing in hyperpolarized 3He lung MRI.* Magnetic resonance in medicine 2010. **63**(4): p. 1059-69.
7. Nikolaou, P., et al., *Near-unity nuclear polarization with an open-source 129Xe hyperpolarizer for NMR and MRI.* Proc Natl Acad Sci U S A, 2013. **110**(35): p. 14150-5.
8. Prisk, K.G. and R.C. Sa, *It's about numbers, not pictures.* J Appl Physiol (1985), 2014. **116**(2): p. 127-8.
9. Bloch, F., *The Principle of Nuclear Induction.* Science, 1953. **118**(3068): p. 425-30.
10. Purcell, E.M., H.C. Torrey, and R.V. Pound, *Resonance Absorption by Nuclear Magnetic Moments in a Solid.* Physical Review, 1946. **69**(1-2): p. 37-38.
11. Lauterbur, P.C., *Image formation by induced local interactions. Examples employing nuclear magnetic resonance. 1973.* Clin Orthop Relat Res, 1989(244): p. 3-6.
12. Mansfield, P. and P.K. Grannell, *Nmr Diffraction in Solids.* Journal of Physics C-Solid State Physics, 1973. **6**(22): p. L422-L426.
13. Levitt, M.H., *Spin dynamics : basics of nuclear magnetic resonance*. 2nd ed. ed. 2008, Hoboken, N.J.: Wiley ; Chichester : John Wiley [distributor].
14. Moeller, H.E., et al., *MRI of the lungs using hyperpolarized noble gases.* Magnetic resonance in medicine : official journal of the Society of Magnetic Resonance in Medicine / Society of Magnetic Resonance in Medicine, 2002. **47**(6): p. 1029-51.
15. Haacke, E.M., *Magnetic resonance imaging : physical principles and sequence design*. 1999, New York: Wiley. xxvii, 914 p.
16. Kauczor, H., R. Surkau, and T. Roberts, *MRI using hyperpolarized noble gases.* Eur Radiol, 1998. **8**(5): p. 820-7.
17. Haase, A., et al., *FLASH imaging: rapid NMR imaging using low flip-angle pulses. 1986.* Journal of magnetic resonance, 1986. **213**(2): p. 533-41.
18. Oppelt, A., et al., *FISP-a new fast MRI sequence.* electromedica, 1986. **54**(1): p. 15-8.
19. Scheffler, K. and S. Lehnhardt, *Principles and applications of balanced SSFP techniques.* Eur Radiol, 2003. **13**(11): p. 2409-18.
20. Wild, J.M., et al., *MRI of the lung (1/3): methods.* Insights Imaging, 2012. **3**(4): p. 345-53.
21. Noll, D.C., D.G. Nishimura, and A. Macovski, *Homodyne detection in magnetic resonance imaging.* IEEE Trans Med Imaging, 1991. **10**(2): p. 154-63.
22. Huang, T.Y., et al., *Are TrueFISP images T2/T1-weighted?* Magn Reson Med, 2002. **48**(4): p. 684-8.
23. Rajaram, S., et al., *Lung morphology assessment with balanced steady-state free precession MR imaging compared with CT.* Radiology, 2012. **263**(2): p. 569-77.
24. Edelman, R.R., et al., *Noninvasive assessment of regional ventilation in the human lung using oxygen-enhanced magnetic resonance imaging.* Nat Med, 1996. **2**(11): p. 1236-9.
25. Sa, R.C., et al., *Vertical distribution of specific ventilation in normal supine humans measured by oxygen-enhanced proton MRI.* Journal of applied physiology, 2010. **109**(6): p. 1950-9.
26. Bauman, G., et al., *Non-contrast-enhanced perfusion and ventilation assessment of the human lung by means of fourier decomposition in proton MRI.* Magn Reson Med, 2009. **62**(3): p. 656-64.
27. Kjorstad, A., et al., *Quantitative lung ventilation using Fourier decomposition MRI; comparison and initial study.* MAGMA, 2014. **27**(6): p. 467-76.

28. Capaldi, D.P., et al., *Free-breathing Pulmonary H and Hyperpolarized He MRI: Comparison in COPD and Bronchiectasis.* Acad Radiol, 2014.
29. Shea, D., *The Helium-3 Shortage: Supply, Demand, and Options for Congress*. 2010, Congressional Research Service: Washington, DC. p. 1-27.
30. Cho, A., *Physics. NRC urges U.S. to rethink sale of helium reserve.* Science, 2010. **327**(5965): p. 511.
31. Kuethe, D.O., et al., *Imaging lungs using inert fluorinated gases.* Magn Reson Med, 1998. **39**(1): p. 85-8.
32. Colegrove, F.D., L.D. Schearer, and G.K. Walters, *Polarization of He^3 Gas by Optical Pumping.* Physical Review, 1963. **132**(6): p. 2561-2572.
33. Walker, T.G. and W. Happer, *Spin-exchange optical pumping of noble-gas nuclei.* Reviews of Modern Physics, 1997. **69**(2): p. 629-642.
34. Norquay, G., et al., *Optimized production of hyperpolarized 129Xe at 2 bars for in vivo lung magnetic resonance imaging.* Journal of Applied Physics, 2013. **113**(4): p. -.
35. Parra-Robles, J., A.R. Cross, and G.E. Santyr, *Theoretical signal-to-noise ratio and spatial resolution dependence on the magnetic field strength for hyperpolarized noble gas magnetic resonance imaging of human lungs.* Med Phys, 2005. **32**(1): p. 221-9.
36. Xu, X., et al., *Hyperpolarized 129Xe gas lung MRI-SNR and T2* comparisons at 1.5 T and 3 T.* Magn Reson Med, 2012. **68**(6): p. 1900-4.
37. Parra-Robles, J., et al., *Theoretical prediction and experimental measurement of the field dependence of the apparent transverse relaxation of hyperpolarized noble gases in lungs.* J Magn Reson, 2008. **192**(1): p. 85-91.
38. Rao, M., R. Fraser, and J.M. Wild, *Dedicated Receiver Array Coil for 1H Lung Imaging with Synchornous Acquistion of Hyperpolarized 3He and 129Xe Gas*, in *ISMRM*. 2014, Proc. Intl. Soc. Mag. Reson. Med. : Milan, Italy. p. 0625.
39. Wild, J.M., et al., *MR imaging of the lungs with hyperpolarized helium-3 gas transported by air.* Phys Med Biol, 2002. **47**(13): p. N185-90.
40. Saam, B., W. Happer, and H. Middleton, *Nuclear relaxation of 3He in the presence of O2.* Phys Rev A, 1995. **52**(1): p. 862-865.
41. Acosta, R.H., et al., *Controlling diffusion of 3He by buffer gases: a structural contrast agent in lung MRI.* J Magn Reson Imaging, 2006. **24**(6): p. 1291-7.
42. Wild, J.M., et al., *k-space filtering in 2D gradient-echo breath-hold hyperpolarized 3He MRI: spatial resolution and signal-to-noise ratio considerations.* Magnetic resonance in medicine, 2002. **47**(4): p. 687-95.
43. Deppe, M.H., et al., *Susceptibility effects in hyperpolarized (3)He lung MRI at 1.5T and 3T.* Journal of magnetic resonance imaging : JMRI, 2009. **30**(2): p. 418-23.
44. Zhao, L. and M.S. Albert, *Biomedical imaging using hyperpolarized noble gas MRI: pulse sequence considerations.* Nucl Instrum Methods Phys Res A, 1998. **402**: p. 454-60.
45. Salerno, M., et al., *Dynamic spiral MRI of pulmonary gas flow using hyperpolarized (3)He: preliminary studies in healthy and diseased lungs.* Magnetic resonance in medicine : official journal of the Society of Magnetic Resonance in Medicine / Society of Magnetic Resonance in Medicine, 2001. **46**(4): p. 667-77.
46. Marshall, H., et al., *K-space filter deconvolution and flip angle self-calibration in 2D radial hyperpolarised (3) He lung MRI.* NMR in biomedicine, 2011.
47. Dregely, I., et al., *32-channel phased-array receive with asymmetric birdcage transmit coil for hyperpolarized xenon-129 lung imaging.* Magn Reson Med, 2013. **70**(2): p. 576-83.
48. Wild, J.M., et al., *Dynamic radial projection MRI of inhaled hyperpolarized 3He gas.* Magnetic resonance in medicine : official journal of the Society of Magnetic Resonance in Medicine / Society of Magnetic Resonance in Medicine, 2003. **49**(6): p. 991-7.
49. Ajraoui, S., et al., *Acquisition of (3)He ventilation images, ADC, T(2)* and B(1) maps in a single scan with compressed sensing.* NMR in biomedicine, 2012. **25**(1): p. 44-51.
50. Wild, J.M., et al., *Comparison between 2D and 3D gradient-echo sequences for MRI of human lung ventilation with hyperpolarized 3He.* Magnetic resonance in medicine : official journal of the Society of Magnetic Resonance in Medicine / Society of Magnetic Resonance in Medicine, 2004. **52**(3): p. 673-8.
51. McMahon, C.J., et al., *Hyperpolarized 3helium magnetic resonance ventilation imaging of the lung in cystic fibrosis: comparison with high resolution CT and spirometry.* Eur Radiol, 2006. **16**(11): p. 2483-90.

52. Woodhouse, N., et al., *Assessment of hyperpolarized 3He lung MRI for regional evaluation of interventional therapy: a pilot study in pediatric cystic fibrosis.* J Magn Reson Imaging, 2009. **30**(5): p. 981-8.
53. Mathew, L., et al., *Hyperpolarized 3He magnetic resonance imaging of chronic obstructive pulmonary disease: reproducibility at 3.0 tesla.* Acad Radiol, 2008. **15**(10): p. 1298-311.
54. van Beek, E.J., et al., *Hyperpolarised 3He MRI versus HRCT in COPD and normal volunteers: PHIL trial.* Eur Respir J, 2009. **34**(6): p. 1311-21.
55. de Lange, E.E., et al., *Changes in regional airflow obstruction over time in the lungs of patients with asthma: evaluation with 3He MR imaging.* Radiology, 2009. **250**(2): p. 567-75.
56. Tzeng, Y.S., et al., *Investigation of hyperpolarized 3He magnetic resonance imaging utility in examining human airway diameter behavior in asthma through comparison with high-resolution computed tomography.* Acad Radiol, 2008. **15**(6): p. 799-808.
57. Woodhouse, N., et al., *Combined helium-3/proton magnetic resonance imaging measurement of ventilated lung volumes in smokers compared to never-smokers.* Journal of magnetic resonance imaging : JMRI, 2005. **21**(4): p. 365-9.
58. Swift, A.J., et al., *Emphysematous changes and normal variation in smokers and COPD patients using diffusion 3He MRI.* Eur J Radiol, 2005. **54**(3): p. 352-8.
59. Yablonskiy, D.A., et al., *Quantification of lung microstructure with hyperpolarized 3He diffusion MRI.* J Appl Physiol, 2009. **107**(4): p. 1258-65.
60. Parra-Robles, J., et al. *Mapping the microscopic distribution of acinar airway length scales using fractal exponential analysis of helium-3 diffusion MRI*. in *ATS*. 2014. San Diego.
61. Deninger, A.J., et al., *Quantification of regional intrapulmonary oxygen partial pressure evolution during apnea by (3)He MRI.* Journal of magnetic resonance, 1999. **141**(2): p. 207-16.
62. Wild, J.M., et al., *Synchronous acquisition of hyperpolarised 3He and 1H MR images of the lungs - maximising mutual anatomical and functional information.* NMR in biomedicine, 2011. **24**(2): p. 130-4.
63. Deninger, A.J., et al., *Assessment of a single-acquisition imaging sequence for oxygen-sensitive (3)He-MRI.* Magnetic resonance in medicine, 2002. **47**(1): p. 105-14.
64. Cieslar, K., et al., *Measurement of nonlinear pO2 decay in mouse lungs using 3He-MRI.* NMR in biomedicine, 2007. **20**(3): p. 383-91.
65. West, J.B., *Respiratory physiology : the essentials*. 8th ed. 2008, Philadelphia: Wolters Kluwer Health/Lippincott Williams & Wilkins. ix, 186 p.
66. de Rochefort, L., et al., *Phase-contrast velocimetry with hyperpolarized 3He for in vitro and in vivo characterization of airflow.* Magnetic resonance in medicine : official journal of the Society of Magnetic Resonance in Medicine / Society of Magnetic Resonance in Medicine, 2006. **55**(6): p. 1318-25.
67. Stewart, N.J., et al., *Experimental validation of the hyperpolarized Xe chemical shift saturation recovery technique in healthy volunteers and subjects with interstitial lung disease.* Magn Reson Med, 2014.
68. Waugh, A., et al., *Ross and Wilson anatomy & physiology in health and illness*. 12th edition / ed. 2014. xii, 509 pages.
69. Haefeli-Bleuer, B. and E.R. Weibel, *Morphometry of the human pulmonary acinus.* Anat Rec, 1988. **220**(4): p. 401-14.
70. Macklem, P.T., *The physiology of small airways.* American journal of respiratory and critical care medicine, 1998. **157**(5 Pt 2): p. S181-3.
71. Miller, M.R., et al., *Standardisation of spirometry.* Eur Respir J, 2005. **26**(2): p. 319-38.
72. Cotes, J.E., D.J. Chinn, and M.R. Miller, *Lung function : physiology, measurement and application in medicine*. 6th ed. 2006, Malden, Mass. ; Oxford: Blackwell Pub. xi, 636 p.
73. Verbanck, S., et al., *Ventilation heterogeneity in the acinar and conductive zones of the normal ageing lung.* Thorax, 2012. **67**(9): p. 789-95.
74. Barnes, P.J., et al., *Asthma and COPD: Basic Mechanisms and Clinical Management*. 2002: Elsevier Science.
75. Hogg, J.C., *Airway Pathology*, in *Asthma and COPD*, P.J. Barnes, Editor. 2002, Academic Press: London; San Diego, CA. p. 56-66.
76. Yanai, M., et al., *Site of airway obstruction in pulmonary disease: direct measurement of intrabronchial pressure.* J Appl Physiol (1985), 1992. **72**(3): p. 1016-23.
77. Hamid, Q., *Pathogenesis of small airways in asthma.* Respiration, 2012. **84**(1): p. 4-11.
78. Holgate, S.T. and J. Douglass, *Fast Facts: Asthma*. 2006, Oxford: Health Press Limited.
79. Bush, A.A., D.M. Geddes, and M.E. Hodson, *Cystic fibrosis*. 3rd ed. ed. 2007, London: Hodder Arnold.

80. Owen, E. and D. Bilton, *Cystic Fibrosis - our focus. Annual data report 2013*, in *Annual Data Report*. 2013, Cystic Fibrosis Trust: Kent, United Kingdom. p. 56.
81. Lopez, A.D., et al., *Chronic obstructive pulmonary disease: current burden and future projections.* Eur Respir J, 2006. **27**(2): p. 397-412.
82. Price, D.J., *Asthma and COPD*. In clinical practice series. 2004, Edinburgh ; New York: Churchill Livingstone. vi, 143 p.
83. Szilasi, M., et al., *Pathology of chronic obstructive pulmonary disease.* Pathol Oncol Res, 2006. **12**(1): p. 52-60.
84. Quanjer, P.H., et al., *Multi-ethnic reference values for spirometry for the 3-95-yr age range: the global lung function 2012 equations.* Eur Respir J, 2012. **40**(6): p. 1324-43.
85. Wagner, P.D., *Information content of the multibreath nitrogen washout.* J Appl Physiol, 1979. **46**(3): p. 579-87.
86. Aurora, P., W. Kozlowska, and J. Stocks, *Gas mixing efficiency from birth to adulthood measured by multiple-breath washout.* Respiratory physiology & neurobiology, 2005. **148**(1-2): p. 125-39.
87. Brown, R., D.E. Leith, and P.L. Enright, *Multiple breath helium dilution measurement of lung volumes in adults.* Eur Respir J, 1998. **11**(1): p. 246-55.
88. Society, O.s.o.t.A.T., *Single breath Carbon Monoxide Diffusing Capacity (Transfer Factor): Recommendations for a Standard Technique.* American Review of Respiratory Disease, 1987. **136**(5): p. 1299-1307.
89. Fowler, W.S., *Lung function studies; uneven pulmonary ventilation in normal subjects and in patients with pulmonary disease.* J Appl Physiol, 1949. **2**(6): p. 283-99.
90. Larsson, A., C. Jonmarker, and O. Werner, *Ventilation inhomogeneity during controlled ventilation. Which index should be used?* Journal of applied physiology, 1988. **65**(5): p. 2030-9.
91. Aljassim, F., et al., *A whisper from the silent lung zone.* Pediatr Pulmonol, 2009. **44**(8): p. 829-32.
92. Macklem, P.T. and J. Mead, *Resistance of central and peripheral airways measured by a retrograde catheter.* J Appl Physiol, 1967. **22**(3): p. 395-401.
93. Brown, R., et al., *Physiological effects of experimental airway obstruction with beads.* J Appl Physiol, 1969. **27**(3): p. 328-35.
94. Hamid, Q., et al., *Inflammation of small airways in asthma.* J Allergy Clin Immunol, 1997. **100**(1): p. 44-51.
95. Horsley, A.R., et al., *Lung clearance index is a sensitive, repeatable and practical measure of airways disease in adults with cystic fibrosis.* Thorax, 2008. **63**(2): p. 135-140.
96. Brody, A.S., et al., *High-resolution computed tomography in young patients with cystic fibrosis: distribution of abnormalities and correlation with pulmonary function tests.* The Journal of pediatrics, 2004. **145**(1): p. 32-8.
97. Aurora, P., et al., *Multiple breath inert gas washout as a measure of ventilation distribution in children with cystic fibrosis.* Thorax, 2004. **59**(12): p. 1068-73.
98. Gustafsson, P.M., P. Aurora, and A. Lindblad, *Evaluation of ventilation maldistribution as an early indicator of lung disease in children with cystic fibrosis.* The European respiratory journal : official journal of the European Society for Clinical Respiratory Physiology, 2003. **22**(6): p. 972-9.
99. Aurora, P., et al., *Multiple-breath washout as a marker of lung disease in preschool children with cystic fibrosis.* Am J Respir Crit Care Med, 2005. **171**(3): p. 249-56.
100. Hogg, J.C., et al., *The nature of small-airway obstruction in chronic obstructive pulmonary disease.* N Engl J Med, 2004. **350**(26): p. 2645-53.
101. Darling, R.C., et al., *Studies on the Intrapulmonary Mixture of Gases. I. Nitrogen Elimination from Blood and Body Tissues during High Oxygen Breathing.* J Clin Invest, 1940. **19**(4): p. 591-7.
102. Mundt, E., W. Schoedel, and H. Schwarz, *Ueber die Glechmaessigkeit der Lungenbelueftung.* Pflueger's Archiv fuer die gesamte Physiologie des Menschen und der Tiere, 1940. **244**(1): p. 99-106.
103. Fowler, K.T. and P. Hugh-Jones, *Mass spectrometry applied to clinical practice and research.* Br Med J, 1957. **1**(5029): p. 1205-11.
104. Arieli, R., *Mass spectrometer for respiratory research.* Respir Physiol Neurobiol, 2010. **170**(2): p. 183-4.
105. Robinson, P.D., et al., *Consensus statement for inert gas washout measurement using multiple- and single- breath tests.* Eur Respir J, 2013. **41**(3): p. 507-22.

106. Singer, F., et al., *A realistic validation study of a new nitrogen multiple-breath washout system.* PLoS One, 2012. **7**(4): p. e36083.
107. Fuchs, S.I., et al., *Multiple breath washout with a sidestream ultrasonic flow sensor and mass spectrometry: a comparative study.* Pediatr Pulmonol, 2006. **41**(12): p. 1218-25.
108. Fowler, W.S., *Lung function studies; the respiratory dead space.* Am J Physiol, 1948. **154**(3): p. 405-16.
109. Robinson, P.D., M.D. Goldman, and P.M. Gustafsson, *Inert gas washout: theoretical background and clinical utility in respiratory disease.* Respiration, 2009. **78**(3): p. 339-55.
110. Burger, E.J., Jr. and P. Macklem, *Airway closure: demonstration by breathing 100 percent O2 at low lung volumes and by N2 washout.* J Appl Physiol, 1968. **25**(2): p. 139-48.
111. Meneely, G.R. and N.L. Kaltreider, *The Volume of the Lung Determined by Helium Dilution. Description of the Method and Comparison with Other Procedures.* J Clin Invest, 1949. **28**(1): p. 129-39.
112. Aurora, P., *Multiple-breath inert gas washout test and early cystic fibrosis lung disease.* Thorax, 2010. **65**(5): p. 373-374.
113. Lum, S., et al., *Early detection of cystic fibrosis lung disease: multiple-breath washout versus raised volume tests.* Thorax, 2007. **62**(4): p. 341-7.
114. Lutchen, K.R., et al., *Respiratory impedance and multibreath N2 washout in healthy, asthmatic, and cystic fibrosis subjects.* Journal of applied physiology, 1990. **68**(5): p. 2139-49.
115. Verbanck, S., et al., *Conductive and acinar lung-zone contributions to ventilation inhomogeneity in COPD.* American journal of respiratory and critical care medicine, 1998. **157**(5 Pt 1): p. 1573-7.
116. Verbanck, S., et al., *Noninvasive assessment of airway alterations in smokers: the small airways revisited.* American journal of respiratory and critical care medicine, 2004. **170**(4): p. 414-9.
117. Nielsen, N., J.G. Nielsen, and A.R. Horsley, *Evaluation of the impact of alveolar nitrogen excretion on indices derived from multiple breath nitrogen washout.* PLoS One, 2013. **8**(9): p. e73335.
118. Verbanck, S., et al., *Relationships between the lung clearance index and conductive and acinar ventilation heterogeneity.* J Appl Physiol, 2012. **112**(5): p. 782-90.
119. Saidel, G.M., R.B. Salmon, and E.H. Chester, *Moment analysis of multibreath lung washout.* J Appl Physiol, 1975. **38**(2): p. 328-34.
120. Gustafsson, P.M., et al., *Slow and fast lung compartments in cystic fibrosis measured by nitrogen multiple-breath washout.* J Appl Physiol (1985), 2014. **117**(7): p. 720-9.
121. Bouhuys, A., *Pulmonary nitrogen clearance in relation to age in healthy males.* J Appl Physiol, 1963. **18**: p. 297-300.
122. Gomez, D.M., *A mathematical treatment of the distribution of tidal volume throughout the lung.* Proc Natl Acad Sci U S A, 1963. **49**: p. 312-9.
123. Moeller, H.E., et al., *Measurements of hyperpolarized gas properties in the lung. Part III: He-3 T-1.* Magnetic Resonance in Medicine, 2001. **45**(3): p. 421-430.
124. Kaneko, K., et al., *Regional distribution of ventilation and perfusion as a function of body position.* Journal of applied physiology, 1966. **21**(3): p. 767-77.
125. Lewis, S.M., J.W. Evans, and A.A. Jalowayski, *Continuous distributions of specific ventilation recovered from inert gas washout.* Journal of applied physiology: respiratory, environmental and exercise physiology, 1978. **44**(3): p. 416-23.
126. Milic-Emili, J., et al., *Regional distribution of inspired gas in the lung.* Journal of applied physiology, 1966. **21**(3): p. 749-59.
127. Hashimoto, T., A.C. Young, and C.J. Martin, *Compartmental analysis of the distribution of gas in the lungs.* J Appl Physiol, 1967. **23**(2): p. 203-9.
128. Rossing, R.G., *Evaluation of a computer solution of exponential decay or washout curves.* J Appl Physiol, 1966. **21**(6): p. 1907-10.
129. Woodhouse, N., et al., *Combined helium-3/proton magnetic resonance imaging measurement of ventilated lung volumes in smokers compared to never-smokers.* J Magn Reson Imaging, 2005. **21**(4): p. 365-9.
130. Fain, S.B., et al., *Early emphysematous changes in asymptomatic smokers: detection with 3He MR imaging.* Radiology, 2006. **239**(3): p. 875-83.
131. Kirby, M., et al., *Chronic obstructive pulmonary disease: longitudinal hyperpolarized (3)He MR imaging.* Radiology, 2010. **256**(1): p. 280-9.
132. Kirby, M., et al., *Quantitative evaluation of hyperpolarized helium-3 magnetic resonance imaging of lung function variability in cystic fibrosis.* Acad Radiol, 2011. **18**(8): p. 1006-13.

133. Donnelly, L.F., et al., *Cystic fibrosis: combined hyperpolarized 3He-enhanced and conventional proton MR imaging in the lung--preliminary observations.* Radiology, 1999. **212**(3): p. 885-9.
134. de Lange, E.E., et al., *Evaluation of asthma with hyperpolarized helium-3 MRI: correlation with clinical severity and spirometry.* Chest, 2006. **130**(4): p. 1055-62.
135. de Lange, E.E., et al., *The variability of regional airflow obstruction within the lungs of patients with asthma: assessment with hyperpolarized helium-3 magnetic resonance imaging.* J Allergy Clin Immunol, 2007. **119**(5): p. 1072-8.
136. Tustison, N.J., et al., *Feature analysis of hyperpolarized helium-3 pulmonary MRI: a study of asthmatics versus nonasthmatics.* Magn Reson Med, 2010. **63**(6): p. 1448-55.
137. Peterson, E.T., et al., *Measurement of lung airways in three dimensions using hyperpolarized helium-3 MRI.* Phys Med Biol, 2011. **56**(10): p. 3107-22.
138. Ireland, R.H., et al., *An image acquisition and registration strategy for the fusion of hyperpolarized helium-3 MRI and x-ray CT images of the lung.* Phys Med Biol, 2008. **53**(21): p. 6055-63.
139. Lipson, D.A., et al., *Pulmonary ventilation and perfusion scanning using hyperpolarized helium-3 MRI and arterial spin tagging in healthy normal subjects and in pulmonary embolism and orthotopic lung transplant patients.* Magn Reson Med, 2002. **47**(6): p. 1073-6.
140. Koumellis, P., et al., *Quantitative analysis of regional airways obstruction using dynamic hyperpolarized 3He MRI-preliminary results in children with cystic fibrosis.* J Magn Reson Imaging, 2005. **22**(3): p. 420-6.
141. Gast, K.K., et al., *MRI in lung transplant recipients using hyperpolarized 3He: comparison with CT.* Journal of magnetic resonance imaging, 2002. **274**: p. 268-274.
142. Altes, T.A., et al., *Hyperpolarized 3He MR lung ventilation imaging in asthmatics: preliminary findings.* J Magn Reson Imaging, 2001. **13**(3): p. 378-84.
143. Kirby, M., et al., *Chronic obstructive pulmonary disease: quantification of bronchodilator effects by using hyperpolarized (3)He MR imaging.* Radiology, 2011. **261**(1): p. 283-92.
144. Horn, F.C., et al., *Bronchodilator treatment response mapping in COPD using Hyperpolarised gas ventilation MRI*. 2013, ERS: Barcelona.
145. Horn, F.C., et al., *Quantification of regional fractional ventilation in human subjects by measurement of hyperpolarized 3He washout with 2D and 3D MRI.* J Appl Physiol (1985), 2013. **5**: p. 5.
146. Virgincar, R.S., et al., *Quantitative analysis of hyperpolarized (129) Xe ventilation imaging in healthy volunteers and subjects with chronic obstructive pulmonary disease.* NMR Biomed, 2012.
147. Gast, K.K., et al., *(3)He-MRI in follow-up of lung transplant recipients.* Eur Radiol, 2004. **14**(1): p. 78-85.
148. Wild, J.M., et al., *Synchronous acquisition of hyperpolarised 3He and 1H MR images of the lungs - maximising mutual anatomical and functional information.* NMR Biomed, 2011. **24**(2): p. 130-4.
149. Wild, J.M., et al., *Simultaneous imaging of lung structure and function with triple-nuclear hybrid MR imaging.* Radiology, 2013. **267**(1): p. 251-5.
150. Avants, B.B., et al., *A reproducible evaluation of ANTs similarity metric performance in brain image registration.* Neuroimage, 2011. **54**(3): p. 2033-44.
151. Dice, L.R., *Measures of the Amount of Ecologic Association between Species.* Ecology, 1945. **26**(3): p. 297-302.
152. Weir, J.P., *Quantifying test-retest reliability using the intraclass correlation coefficient and the SEM.* J Strength Cond Res, 2005. **19**(1): p. 231-40.
153. Kirby, M., et al., *Hyperpolarized 3He magnetic resonance functional imaging semiautomated segmentation.* Acad Radiol, 2012. **19**(2): p. 141-52.
154. Lustig, M., D. Donoho, and J.M. Pauly, *Sparse MRI: The application of compressed sensing for rapid MR imaging.* Magn Reson Med, 2007. **58**(6): p. 1182-95.
155. Ajraoui, S., et al., *Compressed sensing in hyperpolarized 3He lung MRI.* Magn Reson Med, 2010. **63**(4): p. 1059-69.
156. Aysola, R., et al., *Demonstration of the heterogeneous distribution of asthma in the lungs using CT and hyperpolarized helium-3 MRI.* J Magn Reson Imaging, 2010. **32**(6): p. 1379-87.
157. Fain, S.B., et al., *Functional lung imaging using hyperpolarized gas MRI.* Journal of magnetic resonance imaging : JMRI, 2007. **25**(5): p. 910-23.
158. Tzeng, Y.S., K. Lutchen, and M. Albert, *The difference in ventilation heterogeneity between asthmatic and healthy subjects quantified using hyperpolarized 3He MRI.* J Appl Physiol, 2009. **106**(3): p. 813-22.

159. Samee, S., et al., *Imaging the lungs in asthmatic patients by using hyperpolarized helium-3 magnetic resonance: assessment of response to methacholine and exercise challenge.* J Allergy Clin Immunol, 2003. **111**(6): p. 1205-11.
160. Kirby, M., et al., *Hyperpolarized 3He and 129Xe MR imaging in healthy volunteers and patients with chronic obstructive pulmonary disease.* Radiology, 2012. **265**(2): p. 600-10.
161. Barber, D.C., et al., *Efficient computational fluid dynamics mesh generation by image registration.* Medical image analysis, 2007. **11**(6): p. 648-62.
162. Horn, F.C., et al., *Lung ventilation volumetry with same-breath acquisition of hyperpolarized gas and proton MRI.* NMR Biomed, 2014.
163. Horn, F.C., et al., *Quantification of regional fractional ventilation in human subjects by measurement of hyperpolarized 3He washout with 2D and 3D MRI.* J Appl Physiol (1985), 2014. **116**(2): p. 129-39.
164. Milic-Emili, J., *Radioactive xenon in the evaluation of regional lung function.* Semin Nucl Med, 1971. **1**(2): p. 246-62.
165. Gur, D., et al., *Dynamic computed tomography of the lung: regional ventilation measurements.* Journal of computer assisted tomography, 1979. **3**(6): p. 749-53.
166. Fujimura, M., et al., *A trial to measure local lung volume changes during respiration with CT.* Radiat Med, 2004. **22**(2): p. 82-9.
167. Rhodes, C.G., et al., *Quantification of regional V/Q ratios in humans by use of PET. II. Procedure and normal values.* Journal of applied physiology, 1989. **66**(4): p. 1905-13.
168. Deninger, A.J., et al., *Quantitative measurement of regional lung ventilation using 3He MRI.* Magnetic resonance in medicine : official journal of the Society of Magnetic Resonance in Medicine / Society of Magnetic Resonance in Medicine, 2002. **48**(2): p. 223-32.
169. Emami, K., et al., *Improved technique for measurement of regional fractional ventilation by hyperpolarized 3He MRI.* Magnetic resonance in medicine 2010. **63**(1): p. 137-50.
170. Marshall, H., et al., *Direct visualisation of collateral ventilation in COPD with hyperpolarised gas MRI.* Thorax, 2012. **67**(7): p. 613-7.
171. Deppe, M.H., et al., *Combined Measurement of Pulmonary Inert Gas Washout and Regional Ventilation Heterogeneity by MR of a Single Dose of Hyperpolarized (3)He.* Magnetic Resonance in Medicine, 2011. **65**(4): p. 1076-1084.
172. Otsu, N., *Threshold Selection Method from Gray-Level Histograms.* Ieee Transactions on Systems Man and Cybernetics, 1979. **9**(1): p. 62-66.
173. Hopkins, S.R., et al., *Vertical gradients in regional lung density and perfusion in the supine human lung: the Slinky effect.* Journal of applied physiology, 2007. **103**(1): p. 240-8.
174. Horn, F.C., et al. *Observation of Gravitational Dependence of Regional Fractional Ventilation in Human Lungs with 2D and 3D Multi-Breath Washout Imaging of 3He and 129Xe*. in *International Socienty of Magnetic Resonance in Medicine Annual Meeting*. 2012. Melbourne: International Socienty of Magnetic Resonance in Medicine.
175. Tsao, J., P. Boesiger, and K.P. Pruessmann, *k-t BLAST and k-t SENSE: dynamic MRI with high frame rate exploiting spatiotemporal correlations.* Magnetic resonance in medicine 2003. **50**(5): p. 1031-42.
176. Sa, R.C., et al., *Validating the distribution of specific ventilation in healthy humans measured using proton MR imaging.* J Appl Physiol (1985), 2014. **116**(8): p. 1048-56.
177. Crawford, A.B., et al., *Effect of lung volume on ventilation distribution.* J Appl Physiol (1985), 1989. **66**(6): p. 2502-10.
178. Crawford, A.B., M. Makowska, and L.A. Engel, *Effect of tidal volume on ventilation maldistribution.* Respir Physiol, 1986. **66**(1): p. 11-25.
179. Wild, J.M., et al., *3D volume-localized pO2 measurement in the human lung with 3He MRI.* Magnetic resonance in medicine 2005. **53**(5): p. 1055-64.
180. Wild, J.M., et al., *Sensitivity of Transmit Coil B1+ to Lung Inflation in Hyperpolarised 3He MRI*, in *ISMRM* 2011: Montreal.
181. Wagner, P.D., et al., *Continuous distributions of ventilation-perfusion ratios in normal subjects breathing air and 100 per cent O2.* J Clin Invest, 1974. **54**(1): p. 54-68.
182. Wagner, P.D., *The multiple inert gas elimination technique (MIGET).* Intensive Care Med, 2008. **34**(6): p. 994-1001.
183. Gudbjartsson, H. and S. Patz, *The Rician distribution of noisy MRI data.* Magn Reson Med, 1995. **34**(6): p. 910-4.
184. Henkelman, R.M., *Measurement of signal intensities in the presence of noise in MR images.* Med Phys, 1985. **12**(2): p. 232-3.

185. Kaushik, S.S., et al., *Measuring diffusion limitation with a perfusion-limited gas--hyperpolarized 129Xe gas-transfer spectroscopy in patients with idiopathic pulmonary fibrosis.* J Appl Physiol (1985), 2014. **117**(6): p. 577-85.
186. Rao, M., R. Fraser, and J.M. Wild. *Dedicated Receiver Array coil for 1H lung imaging with synchronous acquisiton of hyperpolarized 3-He and 129-Xe Gas*. in *ISMRM*. 2014. Milan, Italy: ISMRM.
187. Acosta, R.H., et al., *Diffusion in binary gas mixtures studied by NMR of hyperpolarized gases and molecular dynamics simulations.* Phys Chem Chem Phys, 2006. **8**(36): p. 4182-8.
188. Joanes, D.N. and C.A. Gill, *Comparing measures of sample skewness and kurtosis.* Journal of the Royal Statistical Society: Series D (The Statistician), 1998. **47**(1): p. 183-189.
189. Hochberg, Y., *Some generalizations of the T-method in simultaneous inference.* Journal of Multivariate Analysis, 1974. **4**(2): p. 224-234.
190. Marshall, H., et al., *He pO mapping is limited by delayed-ventilation and diffusion in chronic obstructive pulmonary disease.* Magn Reson Med, 2013.
191. Andrew, D.H., et al., *Dynamic Ventilation Distribution During Breath-Hold Differs By Asthma Severity*, in *A19. Understanding Ventilation Distribution In Airways Disease*. 2013, American Thoracic Society. p. A1045-A1045.
192. Horn, F.C., et al., *Delayed gas filling imaged in asthma patients using hyperpolarised 3He MRI*, in *ERS*. 2014, ERS Society: Munich.
193. Dregely, I., et al., *Hyperpolarized Xenon-129 gas-exchange imaging of lung microstructure: first case studies in subjects with obstructive lung disease.* J Magn Reson Imaging, 2011. **33**(5): p. 1052-62.
194. Qing, K., et al., *Regional mapping of gas uptake by blood and tissue in the human lung using hyperpolarized xenon-129 MRI.* J Magn Reson Imaging, 2014. **39**(2): p. 346-59.
195. Mugler, J.P., 3rd, et al., *Simultaneous magnetic resonance imaging of ventilation distribution and gas uptake in the human lung using hyperpolarized xenon-129.* Proc Natl Acad Sci U S A, 2010. **107**(50): p. 21707-12.
196. Boushehri, A., et al., *Equilibrium and Transport-Properties of 11 Polyatomic Gases at Low-Density.* Journal of Physical and Chemical Reference Data, 1987. **16**(3): p. 445-466.